Modeling and Characterization of X-ray Image Detectors

Shaikh Asif Mahmood

A Thesis

In the Department

of

Electrical and Computer Engineering

Presented in Partial Fulfillment of the Requirements

For the Degree of

Doctor of Philosophy (Electrical and Computer Engineering) at

Concordia University

Montréal, Québec, Canada

February 2012

CONCORDIA UNIVERSITY
SCHOOL OF GRADUATE STUDIES

This is to certify that the thesis prepared

By: Shaikh Asif Mahmood

Entitled: Modeling and Characterization of X-ray Image Detectors

and submitted in partial fulfillment of the requirements for the degree of

DOCTOR OF PHILOSOPHY (Electrical and Computer Engineering)

complies with the regulations of the University and meets the accepted standards with respect to originality and quality.

Signed by the final examining committee:

Dr. A. Hammad Chair

Dr. K. S. Karim External Examiner

Dr. A. K. W. Ahmed External to Program

Dr. M. Kahrizi Examiner

Dr. D. Qiu Examiner

Dr. M. Z. Kabir Thesis Supervisor

Approved by

Chair of Department or Graduate Program Director

February 20, 2012

Dean of Faculty

ABSTRACT

Modeling and Characterization of X-ray Image Detectors

Shaikh Asif Mahmood, Ph.D.

Concordia University, 2012

The flat-panel image detectors capture an X-ray image electronically, and enable a smooth clinical transition to digital radiography by replacing traditional film/cassette based system. They provide excellent X-ray images and have been commercialized for different X-ray imaging modalities. However, there still remain significant scientific challenges in these detectors associated with dark current and ghosting which constitute critical performance requirements for modalities such as digital fluoroscopy. This doctoral dissertation involves both experimental characterization and physics-based theoretical modelling of time and bias dependent dark current behaviour and X-ray induced change in sensitivity (ghosting) in X-ray imaging detectors. The theoretical investigations are based on the physics of the individual phenomenon and a systematic solution of physical equations in the photoconductor layer; (i) semiconductor continuity equations (ii) Poisson's equation, and (iii) trapping rate equations. The theoretical model has been validated with the measured and published experimental results.

The developed dark current model has been applied to a-Se and poly-HgI_2 based detectors (direct conversion detectors), and a-Si:H p-i-n photodiode (indirect conversion detectors). The validation of the model with the experimental results determines the physical mechanisms responsible for the dark current in X-ray imaging detectors. The dark current analysis also unveils the important material parameters such as trap center concentrations in the blocking layers, trap depths, and effective barrier heights for injecting carriers. The analysis is important for optimization of the dark current consistent with having good transport properties which can ultimately improve the dynamic range of the detector.

The physical mechanisms of sensitivity reduction (ghosting) and its recovery has been investigated by exposing a-Se detector at high dose and then monitoring the recovery process under (i) resting the samples (natural recovery), (ii) reversing the bias polarity and magnitude, and (iii) shining light. The continuous monitoring of the sensitivity as a function of exposure and time reveals the ghosting mechanisms in a-Se mammography detectors. This research finds a faster sensitivity recovery by reversing the bias during the natural recovery process. The sensitivity recovery mechanisms (e.g., recombination between trapped and oppositely charged free carrier, trapping of oppositely charged free carriers, or relaxation of trap centers) have been qualitatively investigated by validating the simulation results with the experimental data. The ghost removal mechanisms and techniques are important to improve the image quality which can ultimately lead to the reduction of the patient exposure consistent with better diagnosis for different X-ray imaging modalities.

Acknowledgements

First, I am thankful to Allah, the Almighty. I am indebted to my parents and sister for their constant support. I would like to express my earnest gratitude to my supervisor Dr. M. Zahangir Kabir for his continuous guidance, inspiration, and financial support. I am also grateful to Dr. Olivier Tousignant for providing me all the required facility during the experiments in Anrad Corporation, Montreal, Canada. I am thankful to Dr. Jonathan Geenspan of Anrad Corporation for reviewing numerous manuscripts. I would like to thank Professor S. O. Kasap from the University of Saskatchewan for many useful discussions. I would like to express my gratefulness to NSERC, FQRNT and Concordia University for the financial support I have collected. I am grateful to my research colleagues Mr. Md. Wasiur Rahman, Mr. Md Shahnawaz Anjan, Mr. Mazharul Huq Chowdhury, Mr. Md Abdul Mannan, Mr. Salman Moazzem Arnab and Mr. Farzin Manouchehri for their useful and friendly discussions. Finally I am thankful to other members of my family for their concerns about my solitary life in Montreal.

To my loving

parents & sister.

Table of Contents

CHAPTER 1

CHAPTER 2

CHAPTER 3

CHAPTER 4

CHAPTER 5

CHAPTER 6

List of Figures

List of Tables

List of Abbreviations

AB	Anti-bonding
A/D	Analog to digital
Al	Aluminum
AMA	Active matrix array
As	Arsenic
a-Se	Amorphous selenium
a-Si:H	Hydrogenated amorphous silicon
Au	Gold
CB	Conduction band
CCE	Charge collection efficiency
Cl	Chlorine
CsI	Cesium Iodide
EHP	Electron-hole pair
FPXI	Flat panel X-ray imagers
Gd_2O_2S	Gadolinium oxysulfide
IFTOF	Interrupted field time of flight
ITO	Indium tin oxide
IVAP	Intimate valence alternation pair
LP	Lone-pair
Mo	Molybdenum
PECVD	Plasma-enhanced chemical vapor deposition

PGR	Photogeneration ratio
PIB	Particle-in-binder
poly-HgI_2	Polycrystalline Mercuric Iodide
ppm	Parts per million
Pt	Platinum
PVD	Physical vapor deposition
TFT	Thin film transistor
TOF	Time of flight
VAP	Valence alternation pair
VB	Valence band

List of Symbols

α:	Linear attenuation coefficient of a medium
α_{en}:	Energy absorption coefficient of a medium
$(\alpha_{en})_{air}$:	Energy absorption coefficient of air
A:	Area
A^*:	Effective Richardson constant
β_{pf}:	Poole-Frenkel coefficient
β_s:	Schottky coefficient
C:	Capacitance
C_t:	Deep trapping capture coefficient
C_{mn}:	Capacitance of the pixel (m,n)
C_{Le}:	Recombination coefficient between free electrons and trapped holes
C_{Lh}:	Recombination coefficient between free holes and trapped electrons
δ:	Attenuation depth
Δ:	Normalized attenuation depth
ε_0:	Permittivity of vacuum
ε_r:	Relative permittivity
ε_{se}:	Permittivity of a-Se
ε_{si}:	Permittivity of a-Si:H
E_{ab}:	Average absorbed energy
E_g:	Band-gap energy
E_{ph}:	Incident photon energy
E_{phonon}:	Phonon energy
E_t:	Trap depth
E_C:	Energy of conduction band edge
E_F:	Energy of Fermi level
E_{FD}:	Energy of steady-state quasi-Fermi level
E_V:	Energy of valence band edge
φ_e:	Effective barrier for injecting electron from metal to a-Se
φ_h:	Effective barrier for injecting hole from metal to a-Se
φ_{eff}:	Effective barrier for injecting electron from p-i interface
Φ:	Photon fluence
F_0:	Magnitude of applied electric field
F_1:	Metal/a-Se interface electric field at anode
F_2:	Metal/a-Se interface electric field at cathode
F_{ni}:	Electric field at n-i interface
F_{pi}:	Electric field at p-i interface
γ:	EHP generation rate under X-ray exposure

γ_0: EHP generation rate at an electric field F_0
g: Thermal generation rate of carriers
g_e: Thermal generation rate of electrons
g_h: Thermal generation rate of holes
g_{de}: Normalized electron injection rate
g_{dh}: Normalized hole injection rate
η: Quantum efficiency
i: Induced electrode current
i_e: Induced electrode current due to electron
i_h: Induced electrode current due to hole
j: Total current density due to X-ray generated carriers
J_d: Dark current density
J_e: Electron injection current density from metal to a-Se
J_h: Hole injection current density from metal to a-Se
J_i: Electron injection current density through p-i interface
j_{rh}: Current density due to detrapping of holes
J_{se}: Steady-state thermal generation current density due to electron
J_{sh}: Steady-state thermal generation current density due to hole
J_{dep}: Transient current density due to electron depletion
J_{inj}: Total injection current density
J_{diff}: Diffusion current density
J_{drift}: Drift current density
k: Boltzmann constant
L: Total photoconductor thickness
L_n: Thickness of n-layer
L_p: Thickness of p-layer
μ_0: Carrier mobility in extended states
μ_e: Electron mobility
μ_h: Hole mobility
v_0: Phonon frequency
ξ: Irradiation energy dependent constant
n: Concentration of free electrons
n_d: Concentration of depleted electrons
n_i: Intrinsic carrier concentration in i-layer
n_t: Concentration of trapped electrons
n_{tc}: Concentration of trapped electrons in neutral trap centers
n_{tn}: Concentration of trapped electrons in charged trap centers
n_{tc0}: Initial concentration of trapped electrons in neutral trap centers
n_{tn0}: Initial concentration of trapped electrons in charged trap centers
n_{inj}: Average injected carrier concentration through p-i interface

N:	Number of transmitted X-ray photons
N_0:	Initial concentration of deep trap centers
N_a:	Active dopant concentration in p-layer
N_i:	Number of incident X-ray photons on a medium of thickness x
N_l:	Number of incident X-ray photons on a medium of thickness dl
N_s:	Total electronic noise per pixel
N_t:	Concentration of deep trap centers in blocking layer
N_{0c}:	Initial concentration of charged trap centers
N_{0n}:	Initial concentration of neutral trap centers
N_{ph}:	Photon concentration per unit thickness
N_{ti}:	Concentration of deep trap centers in intrinsic layer
N_{sat}:	Saturation value of the X-ray induced deep trap centers
$N_{sat(e)}$:	Saturation value of the X-ray induced deep trap centers for electrons
$N_{sat(h)}$:	Saturation value of the X-ray induced deep trap centers for holes
N_{total}:	Total number of electrons generated by the absorbed X-ray
N_C:	Effective density of states in conduction band
N_V:	Effective density of states in valence band
N_X:	Concentration of X-ray induced deep trap centers
N_{Xe}:	Concentration of X-ray induced deep trap centers for electrons
N_{Xh}:	Concentration of X-ray induced deep trap centers for holes
$N(E)$:	Density of states at energy E
p:	Concentration of free holes
p_t:	Concentration of trapped holes
p_{tc}:	Concentration of trapped holes in neutral trap center
p_{tn}:	Concentration of trapped holes in charged trap center
p_{tc0}:	Initial concentration of trapped holes in neutral trap center
p_{tn0}:	Initial concentration of trapped holes in charged trap center
q:	Elementary charge
Q:	Magnitude of charge signal
Q_0:	Maximum collectable charge
Q':	Actual collected charge
Q_g:	X-ray generated charge
Q_{actual}:	Actual X-ray generated charge under nonuniform electric field
ρ:	Density of material
ρ':	Resistivity of material
ρ_{air}:	Density of air
S:	Detector sensitivity
S_n:	Normalized sensitivity
τ:	Effective carrier life time
τ_0:	Initial deep trapping time

τ_c: Carrier trapping time in charged trap centers
τ_e: Electron lifetime
τ_n: Carrier trapping time in neutral trap centers
τ_h: Hole lifetime
τ_r: Average release time of trapped carriers
τ_{0c}: Initial deep trapping time in charged trap centers
τ_{0n}: Initial deep trapping time in neutral trap centers
τ_{ce}: Electron trapping time in charged trap centers
τ_{ch}: Hole trapping time in charged trap centers
τ_{cs}: Average capture time in shallow traps
τ_{ne}: Electron trapping time in neutral trap centers
τ_{nh}: Hole trapping time in neutral trap centers
τ_{rs}: Average release time in shallow traps
τ_{re}: Average release time of trapped electrons in deep traps
τ_{rh}: Average release time of trapped holes in deep traps
τ_N: Characteristic decay time of meta-stable trap centers
t: Time
t_e: Electron transit time
t_h: Hole transit time
t_{off}: Time gap between two successive X-ray exposure
t_T: Carrier transit time
T: Absolute temperature
T_e: Exposure time
U_B: Energy per electron of a bonding orbital
U_{AB}: Extra electron correlation energy in an AB orbital
U_{LP}: Extra electron correlation energy in an LP orbital
v_d: Drift velocity
v_{de}: Electron drift velocity
v_{dh}: Hole drift velocity
v_R: Thermal velocity
V: Applied voltage
V_t: Thermal voltage
V_{bi}: Built-in voltage
W_0: EHP creation energy at an electric field F_0
$W_\pm$: EHP creation energy
$W_{s\pm}$: Saturated EHP creation energy
x: Distance
X: Amount of exposure
Z: Atomic number

CHAPTER 1

INTRODUCTION

1.1 X-ray (an electromagnetic wave)

X-rays are electromagnetic waves that have a relatively low wavelength (in the range of nanometers). It can pass through most objects, including the human body. X rays are produced by means of a vacuum tube or cathode ray tube. The cathode ray tube is similar to the picture tube of a television. Electrons are accelerated from a cathode at high speed towards a metal anode (e.g., Tungsten) due to a high applied voltage across the tube (between the anode and the cathode). As they hit the metal target, they release energy. Most of this energy is released as heat and a very small amount of the electron's energy is used to knock an electron out from the inner shell of the target metal atom. As a result electrons from higher energy levels drop down to fill the vacancy and emit X-ray photons. The emitted photon energies are determined by the electron energy levels [1]. In 1895, W. C. Röentgen discovered X-rays and, therefore also termed as Röentgen rays. The unit of X-ray exposure is the Roentgen (R). It is a measure of X-ray radiation in terms of its ability to ionize air [2].

1.2 Diagnostic Imaging

Right after his discovery, Röentgen applied X-rays for taking the image of his wife's hand and, within six months, X-rays were used for medical imaging leading to a new branch of medical sciences known as diagnostic radiology. Physicians still utilize the radiographic image for patient diagnosis. Diagnostic image is produced by applying a small dose of X-ray radiation as the information carrier through a part of human body to be imaged. The part of the body (object) is placed between an X-ray source and an X-ray sensitive image receptor (detector). When uniform X-rays from the X-ray source impinge upon the body, the X-rays undergo differential attenuation. The differential absorption of X-rays modulates the intensity of the radiation that reaches the detector. The attenuated X-rays are detected by the detector and produces different shades of black and white on an X-ray image. Typically, bone emerges white, soft tissue appears in shades of gray, and air shows up black [3]. Although solid-state, digital X-ray systems have been developed for medical diagnosis, about 65% of medical imaging is still performed by film based analog process [4].

In analog radiography a photographic film is loaded into a film/screen cassette; taken to an examination room and inserted into X-ray equipment. Then, the patient is positioned, and the X-ray exposure on the film creates a latent image. Following that, the film is taken to a dark room for chemical processing to get the final image. The final image quality has to be checked to ensure that the film is suitable for medical diagnosis. This is a time consuming procedure during which the X-ray room is engaged and the patient has to remain dressed inappropriately [5]. A digital radiography system can make this process faster.

1.3 Digital Radiography

In digital radiography an X-ray image can be viewed immediately without using expensive and environmentally damaging chemicals. The image receptor (photographic film) is replaced by a solid-state detector that converts the X-rays into electronic signals, and after that the signal is digitized by an analog to digital (A/D) converter. The X-ray image can be viewed on a video monitor, and a high quality image can be taken with reduced X-ray dose. It offers for convenient patient handling, computer aided diagnosing, image processing, electronic image archiving and transmission, and high quality dynamic imaging. Therefore, on-site doctors can retrieve and inspect images quickly. In addition the image can be analyzed by specialists who are off-site.

1.3.1 Flat-panel Detector (FPD)

Extensive research has been going on from early 1970s to develop a reliable and affordable digital imaging system for medical diagnosis. Contemporarily an X-ray imaging system based on stabilized amorphous selenium (a-Se) was commercially introduced known as xeroradiography. The xeroradiography had a cumbersome readout technique and therefore, it was unattractive. At the beginning of 1980s storage phosphor based digital radiography system was commercialized [6]. However, digital radiography could not progress further until the large area thin-film transistor (TFT) or switching diode self-scanned active-matrix array (AMA) became technologically possible in early 1990s.

A flat-panel X-ray image detector is a large area integrated circuit that is able to capture an X-ray image and convert it to a digital form. Recent research has shown that the flat-panel X-ray image detectors based on AMA is the most promising digital radiographic technique, and suitable to replace the conventional X-ray film/screen cassettes for diagnostic medical digital X-ray imaging applications (e.g., mammography, chest radiography and fluoroscopy) [7]. The basis of flat-panel X-ray imager (FPXI) is the integration of the traditional X-ray detection materials such as phosphors or photoconductors with a large-area active-matrix readout structure. The flat-panel imagers incorporating AMA are commonly called active-matrix flat-panel imagers or AMFPI. Figure 1.1 shows a schematic illustration of the flat-panel X-ray image detector concept. The X-rays form the X-ray tube pass through an object (a hand in the figure), and impinge on a large area flat-panel sensor that replaces the normal film. The flat-panel consists of millions of pixels, each are square, and are spaced at equal intervals throughout the imaging plane. Each pixel acts as an individual detector which produces a certain amount of charge relative to the amount of radiation it receives. It is the stored charge distribution on the pixel capacitors which forms the latent image. The stored charges are simply read out by scanning the pixel arrays row-by-row manner using the electronic switches. Therefore in a flat-panel AMA, the X-ray image is formed in three steps. The first step is the interaction of X-rays with a suitable detection medium (detector) to convert the X-ray photons to a quantity of charge (ΔQ). In the second step the charge (ΔQ) is accumulated in a storage device. In the final step, the stored charge is measured, and digitized for computer acquisition, display and transmission. In flat-panel imagers there are two most common techniques to convert X-ray photons to electric charges; direct, and indirect conversion technique.

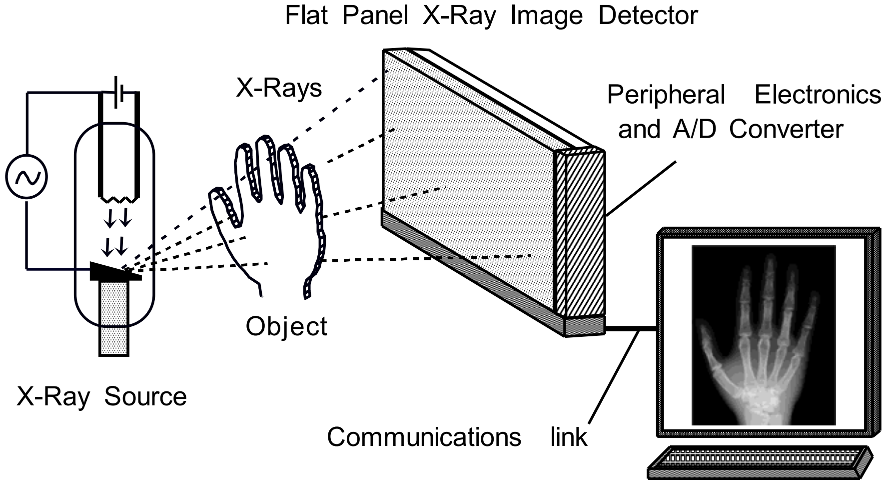

Figure 1.1 Schematic illustration of a diagnostic imaging with a flat-panel X-ray image detector.

1.4 Indirect Conversion Flat-panel Detector

In a flat-panel detector the indirect conversion technique has been utilized by several research groups and manufacturers [8, 9, 10]. In the indirect conversion flat-panel detector, a scintillator (phosphor) layer is placed in intimate contact with an AMA. Figure 1.2 shows the structure of an indirect conversion X-ray image sensor. A thick layer (~ 1.5 μm) of intrinsic hydrogenated amorphous silicon (a-Si:H) is sandwiched between two highly doped n^+ and p^+ layers. The n^+ layer is doped a-Si:H, and it is around 10 to 50 nm thick. The thin (~ 10 to 20 nm) p^+ layer is $\mu c\text{-}Si_{1-x}C_x$:H. The top electrode of the p^+-i-n^+

photodiode is a thin (~ 50 nm) layer of transparent indium tin oxide (ITO). A surface passivation layer covers the photodiode structure and the TFT array. The passivation is a chemical or physical process to encapsulate the semiconductor surface with a protective layer. The passivation is required to keep the properties of the array stable.

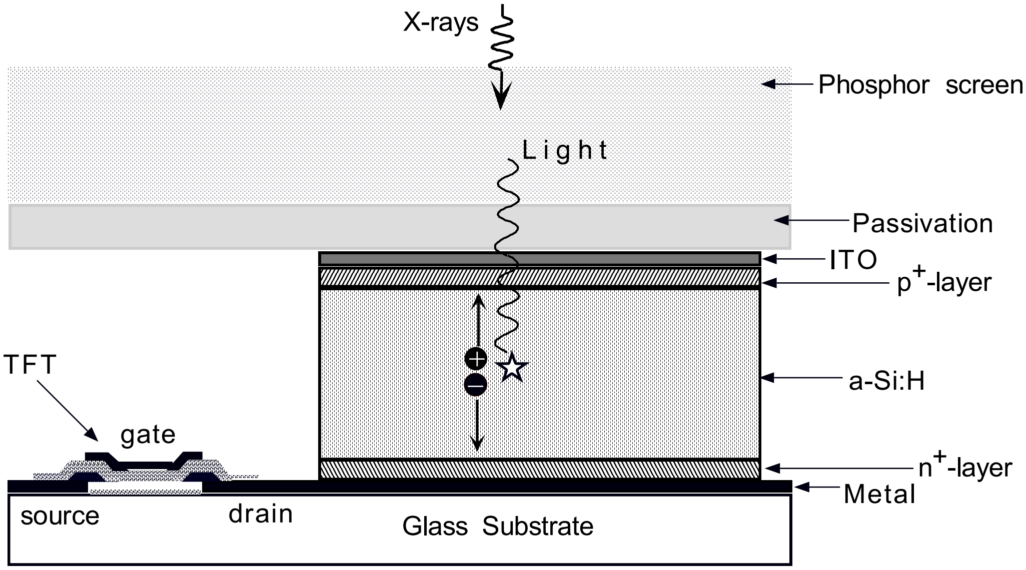

Figure 1.2 Cross section of a single pixel for an indirect conversion AMFPI.

In the indirect approach, the X-ray radiation is absorbed by the scintillator, and a proportionate number of light photons are created. These visible lights subsequently interact with a photodiode of the AMA, and produce the corresponding electrical charge. This electrical charge is stored on the pixel capacitor. Then, the accumulated charge is read out by peripheral electronic circuitry. In indirect conversion flat-panel imagers, either unstructured scintillator such as gadolinium oxysulfide (Gd_2O_2S) or structured scintillator such as cesium iodide (CsI), are used. The unstructured scintillators are cheaper, and have inert physical characteristics. However, with the unstructured scintillators, the visible light can spread to the neighboring pixels and thus reduce spatial resolution. With a structured scintillator, the light spreading is significantly reduced [5].

1.5 Direct Conversion Flat-panel Detector

In direct conversion flat-panel detectors, a suitable photoconductor converts the incident X-rays directly into charge. Contrary to the indirect approach, the image information is transferred from X-rays directly to electrical charge without any intermediate stage. Therefore, the terms indirect and direct are more referable to the nature of the initial X-ray detection mechanism. The details of the flat-panel array design are not attributable to this terminology. In both conversion techniques, the flat-panel detector integrates the incoming signal over a finite period of time. Thus it functions as an X-ray fluence detector rather than an individual X-ray photon detector.

A simplified, schematic diagram of a direct conversion X-ray image detector is shown in Fig. 1.3. The X-ray photoconductor layer is coated onto an AMA to serve as an X-ray-to-charge transducer. The photoconductor material is a large band-gap ($E_g > 2$ eV) and high atomic number (Z) semiconductor such as stabilized amorphous selenium (a-Se). The photoconductor criteria will be discussed in detail later. In order to apply a bias potential and, hence an electrical field F_0, a metal electrode is deposited onto the photoconductor layer. This top electrode is also called radiation-receiving electrode. The other (bottom) electrode is called pixel electrode or charge collection electrode. The applied bias on the top electrode may be either positive or negative with respect to bottom electrode. Depending on the bias polarity the detector shows distinct response and characteristics. The range of the applied bias may vary from few hundred to several thousand Volts. Most of the applied voltage drops across the photoconductor, since the pixel capacitance C_{mn}, is much higher than the capacitance of the photoconductor layer over the pixels.

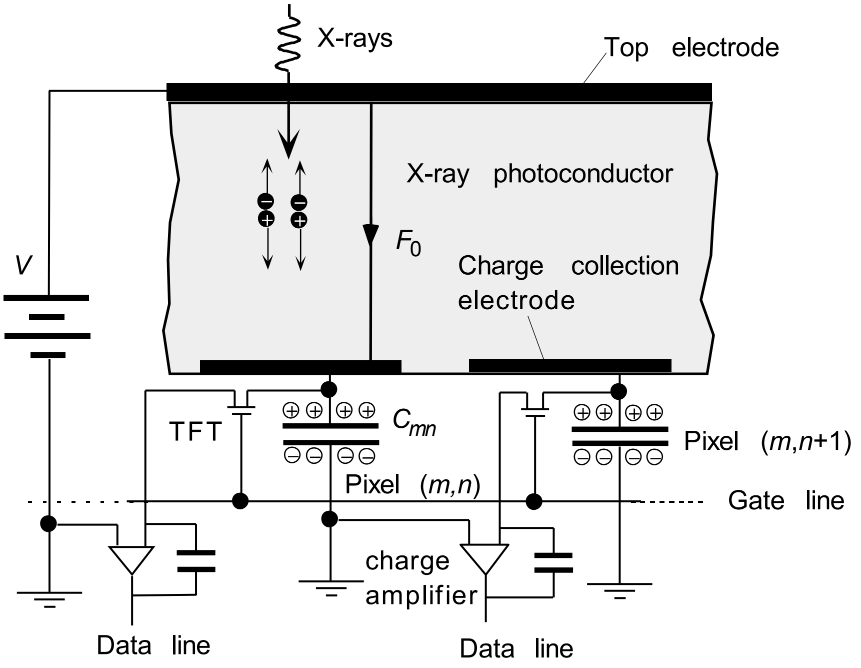

Figure 1.3 A simplified, schematic diagram of the cross sectional structure of two pixels of a direct conversion X-ray image detector [4].

In direct approach, electron hole pairs (EHP) are generated in the photoconductor by the absorption of X-ray photons. If positive voltage is applied the electrons are collected by the top electrode and the holes are accumulated on the pixel capacitor. The stored charges on the pixel capacitor provide a charge signal, Q_{mn} which are readout by scanning the pixel arrays. The magnitude of the charge, Q_{mn} that accumulates at each pixel is proportional to the amount of incident X-ray over that pixel.

Figure 1.4 shows a simplified structure of a single pixel with thin film transistor (TFT) of the direct conversion detector. There are three electrical connections for each TFT. The gate controls on/off state of the TFT; the drain is connected to the pixel electrode and the source is connected to a common data line (Fig. 1.3). The scanning control circuit generates pulses to turn on the corresponding TFT to read out the latent image charge, Q_{mn}.

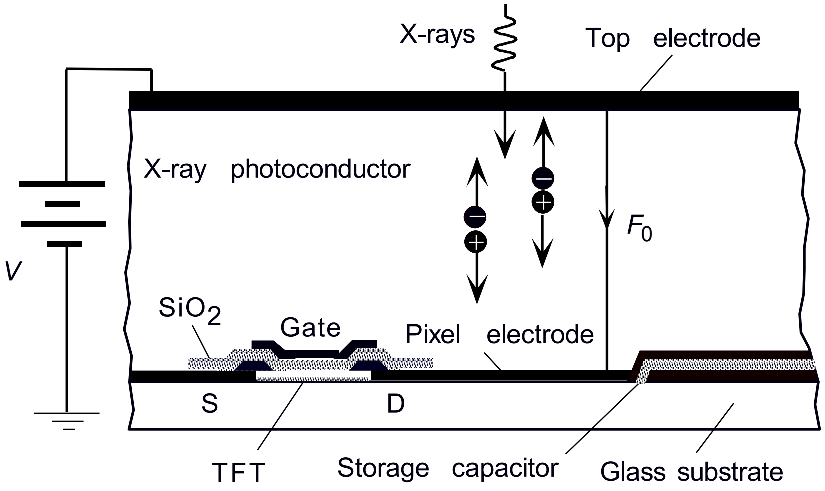

Figure 1.4 Simplified physical cross section of a single pixel (m,n) with a TFT switch of a direct conversion X-ray detector.

The physical structure of a flat-panel active-matrix direct conversion X-ray image sensor is shown in Fig. 1.5. In direct conversion flat-panel detector the light scattering by scintillator is nonexistent. The X-ray generated carriers travel along the applied field lines that are perpendicular to the plane of image. Therefore the lateral spread of the X-ray generated response is negligible which results a spectacularly detailed image. Other advantages of the direct conversion technique are, the absence of noise associated with optical coupling and the easy integration of the photoconductor with the AMA.

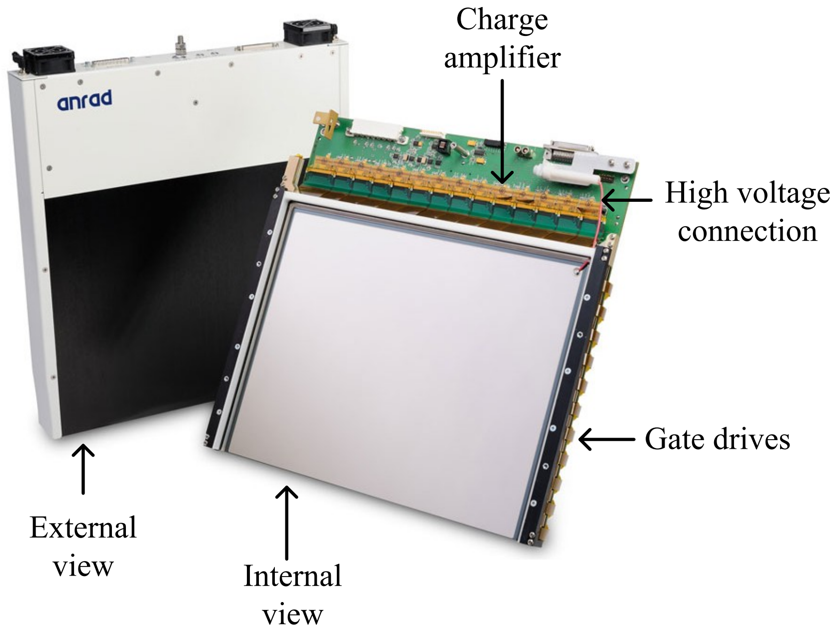

Figure 1.5 The physical structure of a direct conversion flat-panel detector (Courtesy of ANRAD Corporation).

1.6 General Readout Operation

Figure 1.6 shows a small group of pixels of an $X \times Y$ (e.g., 2480 × 3072) flat panel AMA. All TFTs in a row are connected by their gate to a common gate control line. The sources of all the TFTs in each column are connected to a common data line. When the gate control line m is activated, all the TFTs in that row are switched on, and Y data lines from $n = 1$ to Y transfer the charges on the pixel electrodes in the row m to the particular amplifier. These parallel signals are then multiplexed into a serial digital signal, and transmitted into a computer for imaging. Then the next row, $m+1$, is activated and the process is repeated until all the rows have been read out.

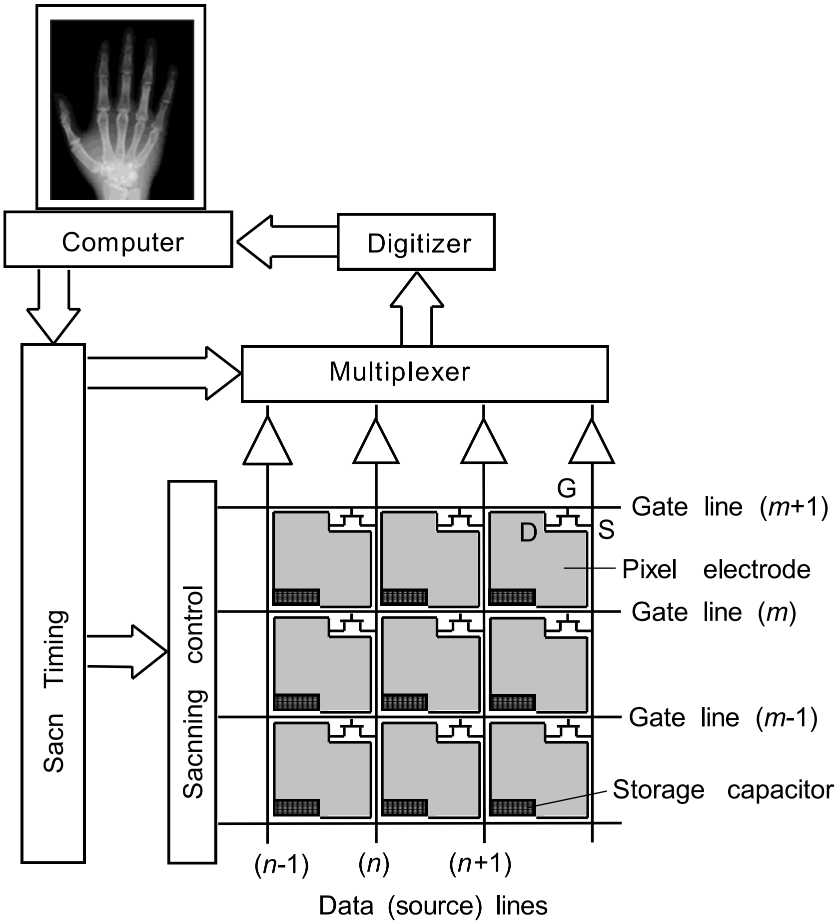

Figure 1.6 Schematic diagram showing a group of pixels of an AMA and the peripheral electronics [5].

1.7 Typical Specifications of Diagnostic X-ray Imaging Systems

The design of a flat-panel X-ray imaging systems depends on the different imaging parameters, such as field of view, dynamic range, spatial resolution, acceptable level of noise. These parameters are related to the clinical need of the particular imaging modality (e.g., mammography, chest radiology, and fluoroscopy). Table 1.1 summarizes the specifications for flat panel detectors for different clinical tasks.

Table 1.1 Criteria for digital X-ray imaging systems for different clinical applications. In this table, kVp is the maximum kV value applied across the X-ray tube during the entire exposure time [5].

Clinical Task	Chest radiology	Mammography	Fluoroscopy
Detector size	35 cm × 43 cm	18 cm × 24 cm	25 cm × 25 cm
Pixel size	200 µm × 200 µm	50 µm × 50 µm	250 µm × 250 µm
Number of pixels	1750 × 2150	3600 × 4800	1000 × 1000
Readout time	~ 1 s	~ 1 s	~1/30 s
X-ray Spectrum	120 kVp	30 kVp	70 kVp
Average exposure	300 µR	12 mR	1 µR
Range of exposure	30 – 3000 µR	0.6 – 240 mR	0.1 – 100 µR

1.8 X-ray Photoconductor

In a direct conversion flat-panel detector the X-ray photoconductor is an X-ray detection media i.e., it act as an X-ray photon to electrical charge transducer. Therefore, the choice and design of the photoconductor strongly influence the performance of the direct conversion X-ray sensors. Before searching for improved performance or better materials, it is useful to identify the parameters that make an X-ray photoconductor nearly perfect. The ideal photoconductor material properties are discussed below:

a) The photoconductor material should be easily deposited onto the large area AMA panel (more than 30×30 cm^2) by conventional vacuum deposition techniques. The deposition should be uniform over the panel and the temperature of the AMA should be maintained below damaging levels (e.g., ~300°C for a-Si panels). The use of single crystal materials is not feasible since it would require much higher temperature, if they were to be grown directly onto the AMA panel.

b) The level of dark current of a photoconductive detector is another important selection criterion for its use in X-ray imaging applications. The current that flows through the detector in absence of light or X-rays is called dark current. The dark current is a source of noise that is added to the signal. It limits the dynamic range due to the accumulation of undesirable charge on the pixel capacitor [11, 12]. Therefore, the metal contacts to the photoconductor should prevent charge injection (i.e., blocking contact) even under very high applied electric field. The rate of thermal generation of carriers from various defects or states in the band-gap of the photoconductor material should also be negligibly small (i.e., dark conductivity is practically zero). Small dark conductivity generally requires a wide band-gap semiconductor. The dark current should be as small as possible (preferably smaller than 100 pA/cm^2) for diagnostic X-ray imaging applications [13, 14, 15] .

c) An X-ray detector should shun unnecessary patient exposure. Thus, the photoconductor should absorb most of the incident X-ray radiation within its practical thickness. That is, over the relevant energy range, the X-ray absorption depth, δ must be considerably less than the photoconductor layer thickness, L.

d) High X-ray sensitivity of the photoconductor is one of the important selection parameters for direct conversion X-ray detectors. This means, the photoconductor must be able to liberate as many EHPs as possible per unit of incident radiation. Therefore the amount of energy required to produce a single EHP, $W_{\pm}$, must be as low as possible. Most of the cases, the EHP creation energy ($W_{\pm}$) is proportional to the band-gap (E_g) of the photoconductor [16].

e) For an ideal photoconductor there should be negligible loss of generated EHP due to deep trapping of carriers. This means, the schubweg for both electron and hole, must be greater than the photoconductor layer thickness, L. The schubweg, $\mu\tau F_0$ (where μ is the drift mobility, τ is the deep trapping time or lifetime, F_0 is the electric field) is defined as the distance that a carrier drifts before it is deeply trapped and unavailable for conduction. Ideally, $\mu\tau F_0 >> L$.

f) The transient artifacts such as image lag (carry over image) and ghosting (change in the X-ray sensitivity) should be minimum (image lag and ghosting are explained in Chapter 2).

The X-ray sensitive crystalline semiconductors are difficult to grow in large areas. Therefore only amorphous and polycrystalline photoconductors are feasible for use in large area X-ray sensors. Amorphous selenium (a-Se) has been used in photocopying industry for over three decades [17]. Hence, it is one of the most highly developed photoconductors for large area detectors. The use of a-Si:H and a-Se has indeed rendered the direct conversion flat panel imaging technology successful. These two key elemental amorphous materials have different properties. However, they can be easily prepared in large areas for TFTs and photoconductor layers. Thick a-Se layers (e.g., 100−1000 μm) can be easily coated onto suitable substrates by conventional vacuum deposition techniques. The deposition of a-Se does not require raising the substrate temperature beyond 60–70°C and it is well below the damaging temperature of the AMA (e.g., ~300°C for a-Si:H panels). Amorphous selenium shows uniform characteristics to very fine scales over large areas. It has an acceptable X-ray absorption coefficient and good charge transport properties. The dark current in a-Se is much smaller than other challenging polycrystalline photoconductors [4, 18]. Therefore a-Se in stabilized form is still the best photoconductor for medical X-ray image sensors. Stabilized a-Se is produced by alloying a-Se with 0.2−0.5% Arsenic (As) and doped with 10−40 ppm Chlorine (Cl).

1.9 Motivations

Under normal operating bias (that creates an applied electric field of ~10 V/μm), the dark current in a simple metal/a-Se/metal structure is particularly high (~1–100 nA/cm^2) which is unacceptable for X-ray imaging applications [13, 19]. It is believed that the main source of this high dark current is charge carrier injection from the metal contacts since the bulk thermal generation current is negligible due to the large mobility gap of a-Se [11, 20]. Recent experiments on a-Se detectors have shown that low dark current can be achieved in a multilayer detector where thin (a few microns) blocking layers are used between the intrinsic layer (i-layer) of a-Se and the metal contacts (i.e., metal/blocking layer/a-Se/blocking layer/metal structure) [5, 21, 22]. The blocking layers are p-type and n-type layers which are appropriately doped a-Se. The p and n layers serve as unipolar conducting layers that can easily trap electrons and holes, respectively, but allow the transport of oppositely charged carriers [4]. This signifies that the p and n layers have a very high concentration of deep trap centers for electrons and holes respectively [20]. The thin blocking layers start trapping charge carriers just after applying the bias field. These trapped charges modify the electric field profile, which actually reduce the electric fields at the metal contacts, and hence reduce subsequent carrier injections from the metal electrodes. Therefore, the initial high dark current decays with time and stabilizes at a much lower value [23]. However, the X-ray generated charge carriers recombine with the oppositely charged trapped carriers in the blocking layers, which can change the amount of trap charges in the blocking layers and the electric field profile. Therefore, these blocking layers control carrier transport, electric field profile across the detector and carrier injections from the metal contacts, and thus have high influence on dark current and X-ray sensitivity. The X-ray sensitivity is defined as the collected charge per unit area per unit exposure of radiation.

Johanson *et al.* have studied the dark current in metal/a-Se/ITO devices [24]. They have found that the dark current for some metal contacts follows an empirical power law relation at high applied electric field, F_0. It has been found that the dark current is not only time and voltage dependent but is also controlled by the metal electrodes. Recently, Kasap and Belev measured the dark current in n-i and single n-layer detector structures (devices are fabricated on cold deposited n-layer) [13, 25]. They have found considerably low dark current in their multilayer detector structures. Until now, no attempt has been made for developing a physical model to explain time dependent dark current behavior in a-Se detectors. The electrical and carrier transport properties of the blocking layers are still unknown. After applying the bias voltage across the detector, the high dark current decays with time by a factor of 10–100 and, most of the cases, reaches a plateau within the time range of 100–1000 s. The exact origin of this drastic decrease in dark current is not known. There are some possibilities such as the formation of blocking contacts and carrier trapping in the blocking layers. A systematic study is essential to investigate the exact origins of the time and voltage dependent dark current. The determination of the physical mechanisms responsible for the dark current, i.e., a quantitative dark current model is the basis for optimization of the dark current consistent with having good transport properties for better overall detector performance (e.g., X-ray sensitivity).

The X-ray sensitivity of a photoconductive detector is an important imaging performance measure. High sensitivity permits the use of low radiation exposure levels which also increases the dynamic range of the image sensor. Recent experiments [26] have shown that the X-ray sensitivity of these detectors changes in subsequent exposures.

The change in the X-ray sensitivity of the X-ray imaging detector as a result of previous X-ray exposures leads to what is called “ghosting”. The change in the X-ray sensitivity with exposure means that the sensitivity of the photoconductor has been altered in a way that depends on the previous image. The effect of ghosting is more pronounced in real-time imaging (e.g., fluoroscopy). The study of ghosting mechanisms and its removal techniques in a-Se based flat panel X-ray imaging detectors is very crucial for a nearly perfect digital X-ray detector.

Sensitivity reduction in a-Se can be attributed to several mechanisms; (i) recombination of drifting carriers with oppositely charged trapped carriers, (ii) creation of X-ray induced meta-stable trap centers and/or (iii) reduction of free carrier generation due to space charge (i.e., due to a non-uniform electric field) [26]. However, the recombination cross-section of the trapped charges and the nature of the X-ray induced meta-stable trap centers are still unknown. Hence, the origins of ghosting have not been fully resolved. Therefore, a systematic study of ghosting under different detector operating conditions and exposures incorporating dark current is essential for understanding the physical nature of ghosting which, in turn, would show ways of neutralizing its negative influence consistent with improvement in the overall detector performance.

A few attempts have been made in the past to describe the ghosting in a-Se detectors by considering metal/a-Se/metal type (called monolayer structure) detector structure [26, 27]. It is found that the amount of ghosting increases with decreasing the applied field because of higher carrier trapping at lower applied electric fields. Bakueva *et al.* [27] have developed an analytical model to describe the ghosting in a-Se detectors by making several unrealistic assumptions; (i) uniform electric field, (ii) no blocking layer, (iii) instantaneous release of deeply trapped holes and, (iv) negligible dark current. Moreover, their model was not appropriately validated with the available experimental results. Recently, Manouchehri *et al.* have studied the time and exposure dependent X-ray sensitivity in multilayer a-Se X-ray imaging detector structures for chest radiology [28]. It has been found that carrier trapping in the intrinsic layer and X-ray induced meta-stable trap center generation are mainly responsible for the reduction of sensitivity. It is well believed that, a-Se has both charge and neutral defects. The carriers trapped by neutral defects participate in a recombination process following Langevin recombination mechanism. On the other hand, those carriers that are trapped by the charged defects become inactive after being trapped. In previous analyses, it has been found that assuming charge trapping by the neutral defects only, the experimental results cannot be matched without using an effective recombination factor, which is less than the Langevin recombination coefficient [28]. This suggests that not all the trapped charges are available for recombination. Therefore, it is necessary to develop a ghosting model considering carrier trapping in both charge and neutral defects. Again, the effect of dark current on the trapped carrier distribution and the collection of dark signal need to be considered for the modeling of ghosting and recovery mechanisms in multilayer a-Se detectors. In order to verify the developed theoretical model, it is necessary to measure dark current and sensitivity at different operating conditions for various a-Se detector structures.

1.10 Research Objectives

The objectives of this research are defined in view of the present challenges (e.g., sensitivity, dark current) in X-ray imaging detectors. The research tasks are as follows:

- Determination of physical mechanisms causing temporal and bias dependent dark current behaviour in X-ray imaging detectors.
- Determination of physical mechanisms causing X-ray induced change in sensitivity (ghosting) in a-Se detectors.
- Determination of trapping and recombination mechanisms in a-Se.
- Determination of physical mechanisms causing change in transport properties of the detector materials with X-ray exposure.
- Investigation of the sensitivity recovery mechanisms and thus the ways of restoring original sensitivity after each exposure.

In this thesis the above mentioned research tasks have been performed through theoretical modelling and verification of the model with the experimental results.

1.10.1 Theoretical Modeling

The bias-dependent transient and steady-state dark current in a-Se detectors has been investigated in this Ph.D. work. The dark current model has been developed by considering metal-semiconductors contact properties, electric field at the contact, and material properties of the blocking layers. The electric field profile in the semiconductor layer has been calculated by considering the concentrations of trap centers, free carriers, and trapped charges through the Poisson's equation. The trap charge distribution has been calculated by solving the trapping rate equation. The dark current model is then incorporated with the ghosting model to describe ghosting phenomenon in a-Se detector. The time and bias dependent dark current model is essential to accurately model the time and exposure dependent sensitivity in X-ray detectors. The dark current analysis also reveals important material parameters of the blocking layers such as the trap center concentrations and metal-semiconductor barrier heights.

In this work, a model has also been developed to describe the transient and steady-state dark current behavoiur in a-Si:H p-i-n photodiodes. Note that the a-Si:H p-i-n photodiodes are used in indirect conversion flat-panel detectors. The concept of the modeling of dark current has also been applied to polycrystalline mercuric iodide (poly-HgI_2) based direct conversion detectors.

This Ph.D. work also includes the modeling of ghosting and its recovery in multilayer a-Se detectors. A numerical model has been developed to study the time and exposure dependent X-ray sensitivity of multilayer a-Se X-ray imaging detectors on repeated X-ray exposures by considering accumulated trapped charges and their effects (trap filling, recombination, electric field profile, electric field dependent electron-hole pair creation), the carrier transport in the blocking layers through the physical equations: (i) semiconductor continuity equations (ii) Poisson's equation, and (iii) trapping rate equations. X-ray induced change in charge carrier trapping and recombination have been considered through the physical equations. The modeling work also considers the possible X-ray induced structural (atomic rearrangements) changes and defect creation in the photoconductor. The carrier trapping time has been calculated based on the trapping cross-sections and the concentrations of trap centers, free carriers and trapped carriers. The cumulative exposure dependent trapped carrier distribution in the photoconductor layer has been determined in the ghosting model.

1.10.2 Experimental Work

The theoretical work mentioned above has been validated by the experimental data. The comparison of the model against the experiment reveals the underlying mechanisms responsible for dark current and X-ray induced change in sensitivity in multilayer a-Se based detectors. The experimental research has been performed at ANRAD Corporation, Montreal.

1.11 Thesis Outline

This doctoral dissertation comprises six chapters. The introductory chapter has started with a brief explanation of X-ray radiation and flat-panel based different X-ray imaging techniques. The typical specifications of diagnostic X-ray imaging systems and the properties of ideal X-ray photoconductor are reported next. Then the motivation of this doctoral research has been described. The chapter concludes with the description of the research objectives and outline of the thesis.

In chapter 2, a review of useful theories and important definitions are described. These include: X-ray attenuation; ionization energy; induced current in photoconductor; X-ray sensitivity; normalized sensitivity; image lag and ghosting; recombination in amorphous photoconductors. The chapter concludes with the analysis of dark current magnitude taking into account different noise sources inherent in the X-ray detection system.

Chapter 3 describes the properties of different potential photoconductors for X-ray image detectors. These materials are amorphous selenium (a-Se), amorphous silicon (a-Si), and polycrystalline mercuric iodide (poly-HgI_2). The comparison of these photoconductor properties are given at the end of third chapter.

In chapter 4, a theoretical model is developed to describe the transient and steady-state behavior of dark current in a-Se based X-ray image detectors. The experimental method of dark current measurement in a-Se based multilayer detectors is described next. The developed dark current model is validated with the measured and the published experimental results for various mono and multi layer a-Se detector structures. A dark model for a-Si:H p-i-n photodiode is also developed and validated with the published experimental results. At the end of chapter 4, the dark current mechanisms for poly-HgI_2 detectors are described and validated with the published data.

In chapter 5, the experimental procedure for ghosting and recovery measurement in a-Se multilayer detectors is explained. Then, a numerical model is developed to describe the ghosting and recovery in a-Se based multilayer X-ray image detectors. The developed model is validated with the measured experimental results for various multilayer a-Se based mammography structures. In this chapter, a ghost removal technique is also investigated by reversing the applied electric field during the natural recovery process.

Chapter 6 concludes this thesis and gives some recommendations for future works.

The references are listed at the end of this dissertation.

CHAPTER 2

BACKGROUND AND THEORIES

In this chapter necessary theories and definitions of important terms related to X-attenuation, charge carrier generation, charge collection mechanism, and imaging characteristic of X-ray image detectors are discussed.

2.1 X-ray Attenuation and Absorption

Attenuation is the removal of incident X-ray photons from an X-ray beam by either absorption or scattering events in a medium. Consider a beam of N_l X-ray photons is incident perpendicularly on a thin plate of thickness dl as shown in Fig. 2.1. The number of X-ray photons that interact with the medium is proportional to the product of the thickness of the medium and the number of X-ray photons in the beam [2]. If α is the probability of interaction, then the reduction of photons (dN_l) from the beam is given by,

$$dN_l = -\alpha N_l dl \,. \tag{2.1}$$

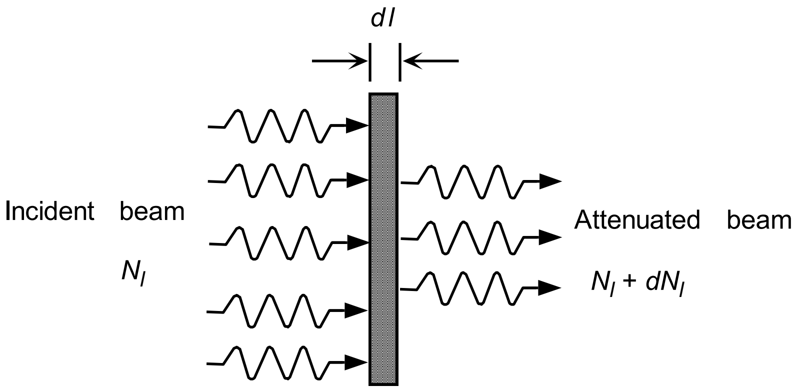

Figure 2.1 Demonstration of X-ray photon attenuation in a medium.

Rearrangement and integration of (2.1) gives,

$$\int_{N_i}^{N} \frac{dN_l}{N_l} = -\alpha \int_0^x dl\,, \tag{2.2}$$

where N_i is the number of incident X-ray photons and N is the transmitted X-ray photons at a thickness x measured from the radiation-receiving surface of the medium. Solution of (2.2) gives,

$$N(x) = N_i e^{-\alpha x} \tag{2.3}$$

The constant α is called the linear attenuation coefficient of the medium. From (2.3) the photon concentration per unit thickness can be expressed as,

$$N_{ph}(x) = \alpha N_i e^{-\alpha x} \tag{2.4}$$

The linear attenuation coefficient of the material is a function of incident photon energy (E_{ph}), atomic number (Z), and density of the material (ρ). When an X-ray photon interacts with a medium, a series of interactions occurs in a random way and, hence not all of its energy is absorbed by the medium. Part of the photon energy is radiated from the medium as scattered radiation and part is converted into kinetic energy of high speed electrons. After many interactions it is possible to calculate the average absorbed energy, E_{ab} by the primary X-ray interaction and, is described by the energy absorption coefficient, α_{en}. The relation between the energy absorption coefficient and the linear attenuation coefficient is given by [2],

$$\alpha_{en} = \alpha \frac{E_{ab}}{E_{ph}} \tag{2.5}$$

From (2.4) the absorbed energy profile can be expressed as

$$E'_{ab}(x) = E_{ab}\alpha N_i e^{-\alpha x} \tag{2.6}$$

It is required to calculate the number of incident photon, N_i which is proportional to the photon fluence, Φ of the incident radiation. The photon fluence is defined as the number of photons per unit area per unit Roentgen (R). If X is the amount of exposure in R, then total number of incident photon on a medium of area A is,

$$N_i = A\Phi X \tag{2.7}$$

From the definition of one Roentgen the expression of photon fluence (photons/cm^2 per unit exposure) can be written as [1],

$$\Phi = \frac{5.45\times10^{13}}{(\alpha_{en}/\rho)_{air} E_{ph}} \tag{2.8}$$

where E_{ph} is the incident photon energy considering monoenergetic beam, $(\alpha_{en})_{air}$ is the energy absorption coefficient of air, ρ_{air} is the density of air. The parameter $(\alpha_{en}/\rho)_{air}$ is called the mass energy absorption coefficient of air which also depends on the photon energy, E_{ph}. Substituting (2.8) into (2.7) and then into (2.6) the absorbed energy profile for an exposure X can be written as,

$$E'_{ab}(x) = \frac{5.45\times10^{13} X}{(\alpha_{en} / \rho)_{air} E_{ph}} A E_{ab} \alpha e^{-\alpha x} \tag{2.9}$$

Using the relation between the energy absorption coefficient and the linear attenuation coefficient (Eq. 2.5) the absorbed energy profile (Eq. 2.9) can be written as,

$$E'_{ab}(x) = \frac{5.45\times10^{13} X}{(\alpha_{en} / \rho)_{air}} A \alpha_{en} e^{-\alpha x} \tag{2.10}$$

The fraction of the X-ray photons that are attenuated in the medium is called the quantum efficiency and is expressed by,

$$\eta = \frac{\int_0^L \alpha N_i e^{-\alpha x} dx}{N_i} \tag{2.11}$$

where L is the total thickness of the medium. Equation 2.11 gives, $\eta = 1 - e^{-\alpha L}$. The attenuation depth, δ is the reciprocal of α, where 63% of the incident X-ray photon beam has been attenuated. The minimization of patient dose requires that most of the X-ray radiation incident on the detector should be absorbed within it, (i.e., the detector length, L, must be greater than δ) and thus, a high absorption coefficient (low δ) is preferred for a particular photoconductor material. Therefore, the required detector thickness depends on the incident photon energy (i.e., type of imaging applications). Typically, the detector length should be several times δ. However, the detector cannot be made very thick since there is a higher probability that the generated charges will be lost due to trapping, as they have to drift greater distances to reach the electrodes. The speed of response of the detector must also be considered if it is designed to operate in real time imaging (e.g., fluoroscopy).

2.2 Ionization Energy ($W_{\pm}$)

An atom is ionized when an energetic electron is ejected by the absorption of an X-ray photon. The interaction mechanisms with a material for diagnostic X-rays (from 10 keV to 120 keV) include photoelectric effect, Rayleigh scattering, and Compton scattering. Among these, the photoelectric effect is the dominant mechanism which results in ionization of the atom. In the photoelectric interaction, the incident X-ray is completely absorbed by the medium, and all of its energy is transferred to the electron. A portion of this transferred energy is used to overcome the binding energy of the electron, and the remaining fraction becomes the kinetic energy of the photoelectron. Initially, a single electron hole pair (EHP) is created. As the energetic photoelectron travels in the solid, it collides with other atoms and causes further ionization along its track and, therefore, many EHPs are created from the absorption of a single X-ray photon.

The ionization energy (or the EHP creation energy), $W_{\pm}$ is the minimum amount of radiation energy absorbed by a medium to create a single EHP. The intrinsic X-ray sensitivity of a photoconductor mostly depends on $W_{\pm}$ because the total free (or collectable) charge generated from an absorbed radiation of energy, E_{ab} is $eE_{ab}/W_{\pm}$, where e is the elementary charge. Therefore, $W_{\pm}$ must be as low as possible in order to maximize the X-ray sensitivity. For most cases $W_{\pm}$ is related to the band-gap energy, E_g of the semiconductor by [29],

$$W_{\pm} \approx 2.8E_g + E_{phonon} \tag{2.12}$$

where the phonon energy term, E_{phonon} is small and hence $W_{\pm}$ typically close to $2.8E_g$. $W_{\pm}$ is well defined for many crystalline materials and it does not depend on the field. However, Eq. 2.12 is not valid for amorphous and polycrystalline materials because they are inherently disorder. Que and Rowlands have shown that in these materials, $W_{\pm}$ should be $2.2E_g + E_{phonon}$ [30]. In some amorphous materials (e.g., a-Se) $W_{\pm}$ depends on the applied electric field and the incident X-ray photon energy [23, 31]. In case of a-Se the origin of the field dependency is possibly due to the recombination of the generated EHPs. However, the exact mechanism of the recombination process has not been conclusively determined [32].

2.3 Induction Current in Photoconductors

The absorption of X-rays in a material creates a cloud of many EHPs due to the photoelectric effect. In a semiconductor (whose band-gap is ~1.0 eV or less) there is enough free charge able to move and surround the created EHPs, which effectively screens the local fields from being sensed at macroscopic distances. Therefore, the charge neutrality is maintained at all points in these materials. If a sensor is fabricated with these semiconductors, no electrode currents are sensed until the moving carriers actually reach the electrodes. In a photoconductor material, there is no reservoir of free carriers available to surround the drifting carriers and, hence on the scale of the carrier transit time the local charge neutrality is not maintained. For a-Se, relaxation time (relaxation time, τ_R is related to resistivity, ρ' by $\varepsilon_{se}\rho'$, where ε_{se} is the dielectric constant of the material) is very long (~ 20−60 minutes) compared to typical carrier transit times (~ μs). Therefore, currents in the photoconductive detector are due entirely to the induced charge on the electrode by the movement of the generated EHPs.

The induced current flowing through the electrode due to the motion of charge carriers in the detector can be determined using the Shockley-Ramo's theorem [33, 34, 35]. Consider a point charge q is drifting with a velocity $v_d(t)$ under a uniform applied electric field F_0, as shown in Fig. 2.2. According to the Shockley-Ramo's theorem the induced current on the negative electrode is [36],

$$i(t) = \frac{qv_d(t)}{L};\ t < t_T \tag{2.13}$$

where L is the photoconductor thickness and t_T is the transit time of the carrier (the required time for a carrier to drift from its generation point to the collecting electrode is called transit time).

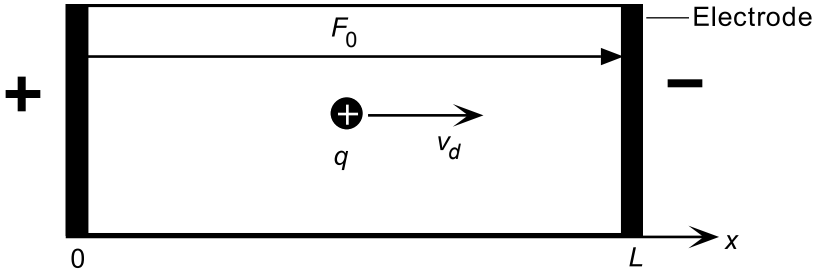

Figure 2.2 A simple photoconductive detector. A point charge drifts under a uniform electric field.

In a typical X-ray detector there is carrier trapping in the photoconductor material. Therefore, only a fraction of X-ray generated carrier is collected in the external circuit. Consider an EHP is generated at a distance x measured from the positive electrode shown in Fig. 2.3. The hole drifts towards the negative electrode and the electron drifts towards the positive electrode, due to the applied electric field. The current contributions from electron and hole are,

$$i_e(t) = \frac{qv_{de}}{L} e^{-t/\tau_e};\ t < t_e, \tag{2.14}$$

$$i_h(t) = \frac{qv_{dh}}{L} e^{-t/\tau_h};\ t < t_h, \tag{2.15}$$

where $v_{de} = \mu_e F_0$, $v_{dh} = \mu_h F_0$, q is the elementary charge, μ is the carrier mobility and τ is the carrier lifetime. The subscripts e and h refer to electrons and holes respectively. Both electron and hole movement induce currents of the same polarity at any electrode and hence, the collected charge at any electrode is the sum of the contributions from both types of drifting carriers. From (2.14) and (2.15) the average collected charge can be written as,

$$Q(x) = \int_0^{t_e} i_e(t)dt + \int_0^{t_h} i_h(t)dt \tag{2.16}$$

where $t_e = x/\mu_e F_0$ and $t_h = (L-x)/\mu_h F_0$ are the electron and hole transit times, respectively. From (2.16) the famous Hecht equation is,

$$Q(x) = \frac{q\mu_e\tau_e F_0}{L}\left(1 - e^{-\frac{x}{\mu_e\tau_e F_0}}\right) + \frac{q\mu_h\tau_h F_0}{L}\left(1 - e^{-\frac{L-x}{\mu_h\tau_h F_0}}\right) \tag{2.17}$$

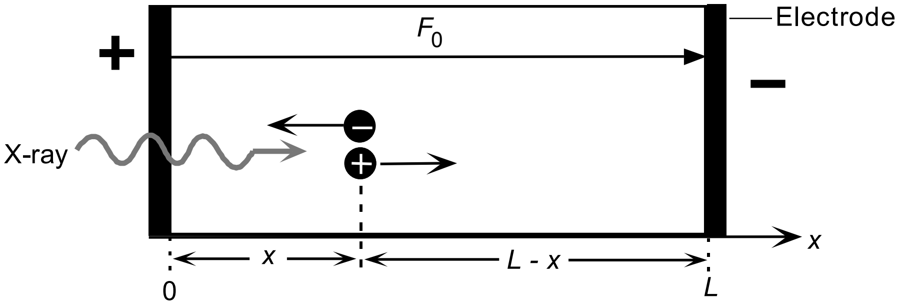

Figure 2.3 A simple photoconductive detector. An electron and a hole drift under a uniform electric field.

2.4 X-ray Sensitivity

The sensitivity of an X-ray image detector is defined as the collected charge per unit area per unit exposure of radiation. The X-ray sensitivity, *S* can be written as,

$$S = \frac{Q}{AX} \tag{2.18}$$

where *A* is the radiation-receiving area in cm^2, *X* is the radiation exposure which is usually measured in Roentgen (R), and *Q* is the collected charge in Coulomb (C). The unit of sensitivity is C/cm^2/R. One Roentgen is the amount of radiation required to create ions carrying a total charge of 2.58×10^{-4} C per kg of air [1]. It has been found that the average energy to produce an ion pair in air is 33.97 eV or 33.97 J/C. Hence, the energy absorbed in air by an exposure of 1 R is, 2.58×10^{-4} C/kg × 33.97 J/C = 0.00876 J/kg of air. The equivalent circuit of an X-ray detector is schematically illustrated in Fig. 2.4. A thick layer of photoconductor is sandwiched between two large area parallel plate electrodes. The top electrode is the radiation-receiving electrode and the bottom electrode is the pixel electrode. The top electrode is biased with a voltage, *V* to establish an electric field, F_0 in the photoconductor. The applied bias voltage may be positive or negative depending on the application. The absorption of X-ray radiation in the photoconductor generates EHPs. The generated carriers are drifted in opposite directions by the applied electric field. The movement of the carrier gives rise to a transient X-ray photocurrent, and the integration of the photocurrent is the collected charge. Actually the charge accumulates on the storage capacitor. The thin film transistor (TFT) is switched on to read this charge via the integrating amplifier. The integration time is longer than the X-ray exposure time.

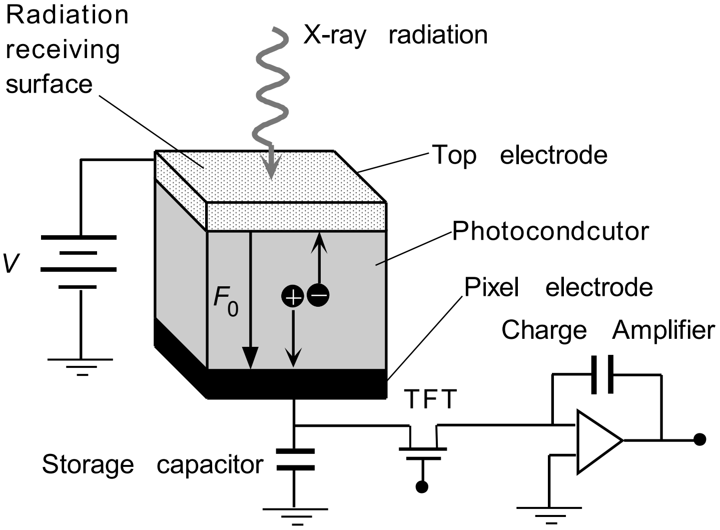

Figure 2.4 Schematic diagram illustrating the equivalent circuit of an X-ray image detector.

2.5 Normalized Sensitivity

The sensitivity of a photoconductor is typically expressed in terms of the normalized sensitivity. The normalized sensitivity, S_n is defined as the ratio of the actual sensitivity to the maximum possible sensitivity that would arise if all of the incident photons were attenuated and all of the liberated carriers were collected by the electrodes. Therefore, it is assumed that the quantum efficiency is unity. In section 2.2, it is mentioned that total collectable charge generated from an absorbed radiation of energy, E_{ab} is $eE_{ab}/W_{\pm}$. Therefore the maximum collectable charge is,

$$Q_0 = \int_0^{\infty} \frac{eE'_{ab}(x)}{W_{\pm}} dx \tag{2.19}$$

In (2.19) the ionization energy (or the EHP creation energy), $W_{\pm}$ is assumed to be independent of applied electric field. Using the expression of absorbed energy profile (Eq. 2.10) and then integrating (2.19) the maximum collectable charge would be,

$$Q_0 = \frac{5.45 \times 10^{13} e}{W_{\pm}(\alpha_{en}/\rho)_{air}} AX \left(\frac{\alpha_{en}}{\alpha} \right) \tag{2.20}$$

If Q' is the actual collected charge then the normalized sensitivity can be expressed as,

$$S_n = \frac{Q'}{Q_0} \tag{2.21}$$

In actual detector with a finite photoconductor thickness, some X-ray photon will be lost. Therefore the X-ray generated charge within the photoconductor thickness, L is given by,

$$Q_g = \frac{5.45 \times 10^{13} e}{W_{\pm}(\alpha_{en}/\rho)_{air}} AX \left(\frac{\alpha_{en}}{\alpha} \right) \eta \tag{2.22}$$

where $\eta = (1 - e^{-\alpha L})$ is the quantum efficiency of the photoconductor. Equations 2.20–2.22 give,

$$S_n = \frac{Q'}{Q_g} \times \eta \tag{2.23}$$

For some photoconductor materials (e.g., a-Se), $W_{\pm}$ depends on the applied electric field. Hence, Q_g will depend on the applied electric field through $W_{\pm}$. However, for uniform applied electric field both $W_{\pm}$ and Q_g will be same throughout the thickness of the photoconductor. Therefore, the normalized sensitivity will depend only on the collected charge Q'. In practical photoconductor the trapped charge modifies the electric field and, hence $W_{\pm}$, which alter the total generated carriers in subsequent exposures. Considering the effect of nonuniform electric field on $W_{\pm}$, the normalized sensitivity can be expressed as,

$$S_n = \frac{Q_{actual}}{Q_g} \times \frac{Q'}{Q_{actual}} \times \eta \tag{2.24}$$

where, Q_{actual} is the actual generated charge due to the nonuniform electric field. The first and the second terms in (2.24) are known as the photogeneration ratio (PGR), and the charge collection efficiency (CCE), respectively. For an ideal photoconductor, both PGR and CCE should be unity and hence, the normalized sensitivity would be equal to the quantum efficiency. However in practical photoconductors, CCE is less than unity since the liberated carrier is lost due to trapping. The PGR would be greater than or less than unity depending on the nonuniform electric field distribution across the thickness of the photoconductor.

2.6 Image Lag and Ghosting

The image lag in image sensor is characterized by the carry-over of the image charge generated by the previous X-ray irradiation into subsequent image frames. The incomplete extraction of charge from the pixel results the residual signal fractions following an X-ray irradiation. Therefore, a change in dark image (i.e., readout of the detector without an X-ray exposure) is observed. Consider a detector is irradiated with X-rays through a small rectangular aperture as shown in Fig. 2.5. The subsequent dark image is shown as well. It is seen that, image lag is manifested as an increase in pixel values in previously exposed areas.

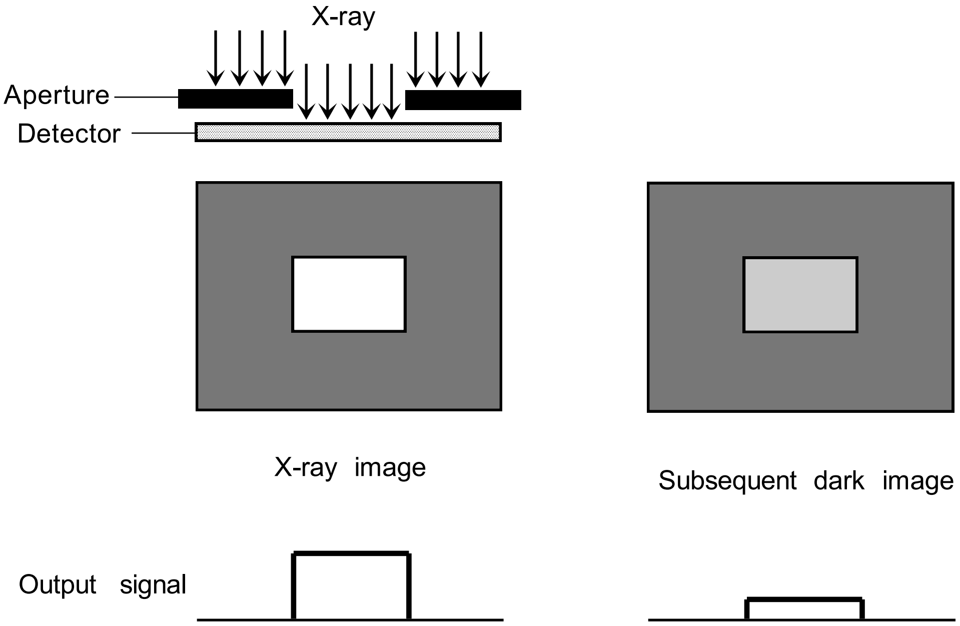

Figure 2.5 Illustration of lag by exposing a detector through a rectangular aperture. A dark image is acquired subsequently.

Ghosting is the change in X-ray sensitivity of an X-ray image detector as a result of previous X-ray exposures. Normally sensitivity of the pixel decreases due to ghosting and hence, a shadow impression of a previously acquired image is visible in subsequent uniform exposure. Consider a detector is irradiated with X-rays through a small rectangular aperture as shown in Fig. 2.6. In the subsequent exposure, the detector is irradiated with uniform X-rays without any aperture. It is evident that the sensitivity of the previously exposed area is less than the sensitivity of the non-exposed area. Ghosting has a large affect on the diagnostic value of X-ray images when images are acquired in a rapid sequence (e.g., fluoroscopy).

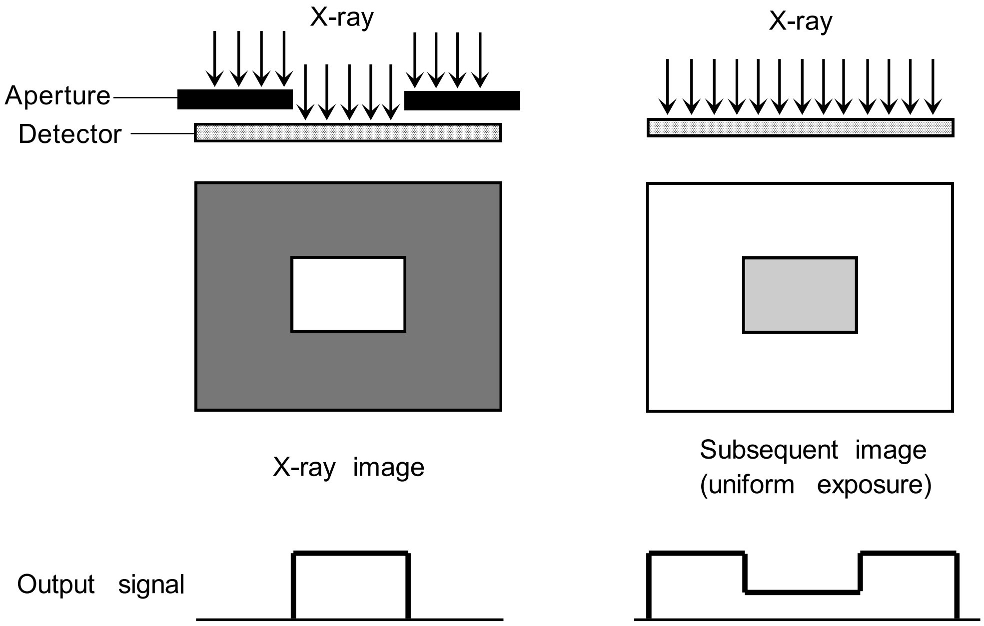

Figure 2.6 Illustration of ghosting by exposing a detector through a rectangular aperture. A shadow impression of a previously acquired image is visible in subsequent uniform exposure.

2.7 Recombination in Amorphous Photoconductors

One of the main reasons for sensitivity reduction is the loss of carrier due to trapping. Instead of trapping, X-ray generated carriers can be lost due to recombination. There are three possible recombination processes in amorphous materials (e.g., a-Se) as shown in Fig. 2.7 [37]. The first mechanism is the recombination between the drifting holes in the valence band (VB) with the drifting electrons in the conduction band (CB). This type of recombination is known as bimolecular recombination, and it is a non-radiative process. The X-ray generated free electrons and holes in a photoconductor move in opposite direction due to the applied electric field. They can come closer during their drift, and eventually recombine. The second process is the recombination of an electron (or hole) in the CB (or VB) with a deep trapped hole (or electron). The third process is the recombination between a trapped hole with a trapped electron. The possibility of the third process is negligible compared to the other two processes. The probability of second type of recombination depends on the concentration of trapped carrier inside the photoconductor and hence, on the carrier lifetime. The release time of trapped charge is longer in amorphous materials. Hence, the trapped carriers accumulate over time inside the photoconductor. Once the concentration of trapped carrier inside the photoconductor becomes large, recombination between the deeply trapped carriers and the drifting carriers at the energy bands (i.e., the second process) becomes dominant.

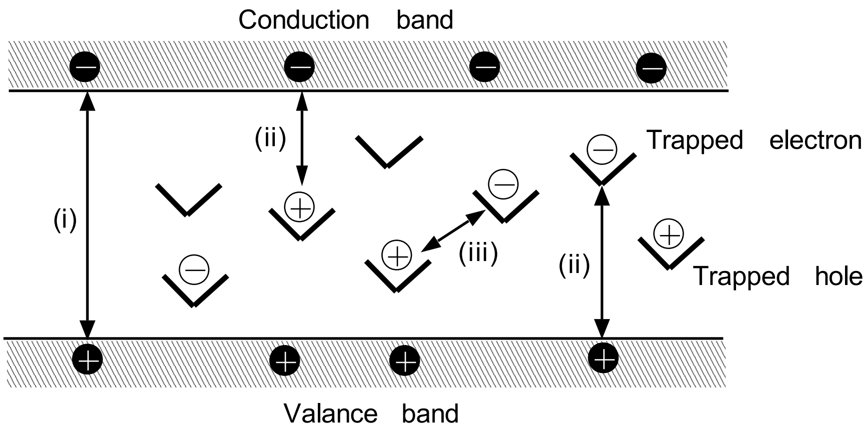

Figure 2.7 Recombination processes in amorphous materials; (i) recombination between drifting carriers in the energy bands, (ii) recombination between a drifting carrier and a trapped carrier, (iii) recombination between trapped carriers.

2.8 Dark Current

The current that flows through the detector without any X-ray irradiation or light is called dark current. It is important to consider the dark current magnitude of a photoconductive detector for its use in X-ray imaging applications. The dark current has many unwanted effects in flat-panel X-ray imagers (FPXIs). The dark current is a source of noise that is added to the signal. It limits the dynamic range due to the accumulation of undesirable charge on pixel capacitors [11, 12]. The charge carrier can be trapped in the photoconductor layer during the flow of dark current, which modifies the internal field and therefore, changes the photo generation efficiency across the thickness of the photoconductor layer.

It is instructive to estimate the acceptable magnitude of dark current taking into account different noise sources inherent in the X-ray detection system. Consider the X-ray image detector shown in Fig. 2.4 with the top electrode negatively biased. Consider that N_{total} is the total number of electrons generated due to the absorption of X-rays. We want to detect N_{total}. The TFT is turned on every δt seconds to read the charge qN_{total} stored on the capacitor. In δt seconds the accumulated charge due to dark current on the capacitor is $J_d A\delta t/q$, where J_d is the dark current density and A is the pixel area. The statistical variation in collected charge due to the dark current should be less than the quantum noise in the signal, which gives,

$$\sqrt{J_d A\delta t / q} < \sqrt{N_{total}} \, . \tag{2.25}$$

In medical imaging applications, N_{total} varies from 10^3 to 10^5 electrons [13]. Taking $A = 10^{-4}$ cm^2, $\delta t = 1$ s, and $N_{total} \sim 10^3$, J_d should be less than 1.6×10^{-12} A/cm^2. Under strong signal condition ($N_{total} \sim 10^5$), J_d should be less than 1.6×10^{-10} A/cm^2.

A noise mechanism associated with the switching action of the TFT is always present in the system. The thermal charge fluctuations in the TFT accumulates a charge of magnitude $\sqrt{(kTC)}$ on the capacitor for every operation of the switch, where k is the Boltzmann constant, T is the absolute temperature, and C is the capacitance of the storage capacitor (Fig. 2.4) [5]. This noise is called reset or kTC noise. The dark current noise should be less than the reset noise, which gives,

$$\sqrt{J_d A\delta t / q} < \sqrt{kTC} / q \, . \tag{2.26}$$

Typically C varies from 0.5 to 2 pF [13]. Taking $C = 0.5$ pF, J_d should be less than 1.3×10^{-10} A/cm^2.

Finally, consider the total electronic noise per pixel in the read circuit. This total electronic noise is the root mean square of the signal expressed as number of electrons, N_s. Depending on the pixel array and the peripheral electronics, N_s varies from 500 to 1000 electrons [13]. The magnitude of the dark current should be within a limit such that,

$$\sqrt{J_d A\delta t / q} < N_s . \tag{2.27}$$

For $N_s = 500$ electrons, $J_d < 4 \times 10^{-10}$ A/cm^2. The summary of the calculated dark current density is given in Table 2.1. Considering the noise sources discussed above, the acceptable levels of dark current density should be in the range of 2 – 100 pA/cm^2.

Table 2.1 Acceptable dark current level based on different noise sources.

Noise criteria	Acceptable J_d (pA/cm^2)
J_d noise < Quantum noise	1.6 − 160
J_d noise < TFT reset noise	130 − 500
J_d noise < Electronic noise	400 − 1600

2.9 Summary

The X-ray attenuation in the medium, quantum efficiency, and ionization energy are described in this chapter. The induction current in photoconductor and the formulation of Hecht equation is explained. The definition of X-ray sensitivity and normalized X-ray sensitivity is given in this chapter. The image lag and ghosting in X-ray imaging detectors are also explained. The recombination process in amorphous materials is described. Finally, the magnitude of dark current has been estimated considering different noise sources inherent in the X-ray detection system.

CHAPTER 3

X-RAY PHOTOCONDUCTORS

The direct conversion flat-panel X-ray image detectors produce superior image quality compared to the indirect conversion detectors, and because of their simpler structure they can be easily manufactured at low cost. The performance of a direct conversion detector critically depends on the selection and design of the X-ray photoconductor. Only amorphous or polycrystalline (poly) photoconductors are currently preferred for large area flat-panel X-ray image detectors. In this chapter, the properties of few candidate materials to be used in flat-panel detectors are discussed.

3.1 Amorphous Materials

The crystalline solids have highly ordered arrangement of atoms as shown in Fig. 3.1 (a). The distances between the atoms (i.e., interatomic spacing) are exact and every atom has an identical number of bonds to its immediate neighbors (i.e., coordination number). The bond length and the bond angle (i.e., angular interval between the bonds) are also well defined. This regular geometric periodicity ideally maintains throughout the entire volume of the material.

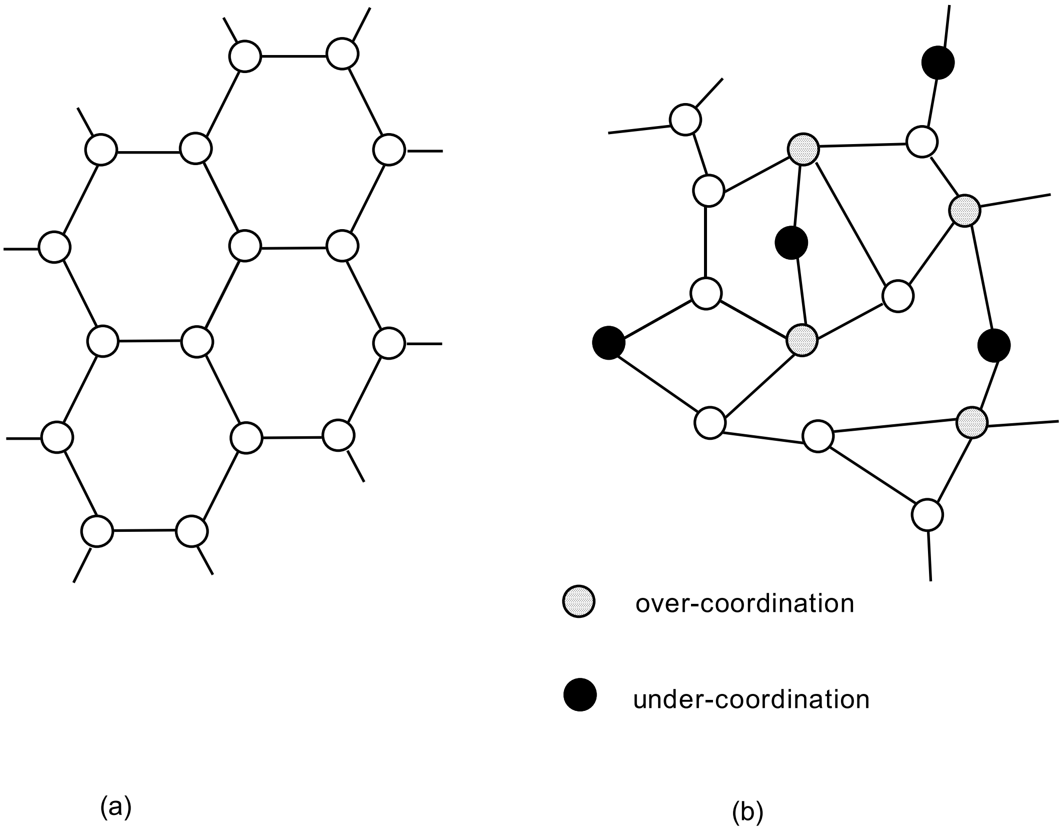

(a) (b)

Figure 3.1 Two dimensional representation of atomic structure for (a) a crystalline semiconductor and (b) an amorphous solids.

The amorphous solids do not have long range order, and they have order only within a few atomic or molecular dimension. They exhibit short range order as the atoms of amorphous solid must satisfy their individual valence bonding requirements. The presence of short range order leads to a slight variation in bond lengths and bond angles between the atoms in the network. This little deviation is sufficient to destroy the long-range order as illustrated in Fig. 3.1(b). The only specific structural feature of amorphous materials is the coordination number of an atom to its neighbor. Hence, the elementary defect of an amorphous semiconductor is a coordination defect when an atom has more (over-coordination) or less (under-coordination) bonds. The short-range electronic structure has the similarity with the crystalline phase of the solids. However, the disorder in the network introduces localized electronic states, which have a profound impact on the electronic and optical properties of amorphous semiconductors.

3.2 Polycrystalline Materials

Polycrystalline material composed of many small crystals in contact with each other. These small crystals are called crystallites. These crystallites are oriented randomly, that means a break in the crystal from one crystallite to the other. The atoms at the border of a crystallite are also linked to the neighbor crystallite ones. However, the atoms at the border cannot follow their normal bonding tendency. This border is called grain boundary as shown in Fig. 3.2. These grains have irregular shapes and orientations and hence, there are vacancy, strained bond and dangling bond at the grain boundary. In addition, there are foreign impurity and interstitial atoms in the grain boundary region [38].

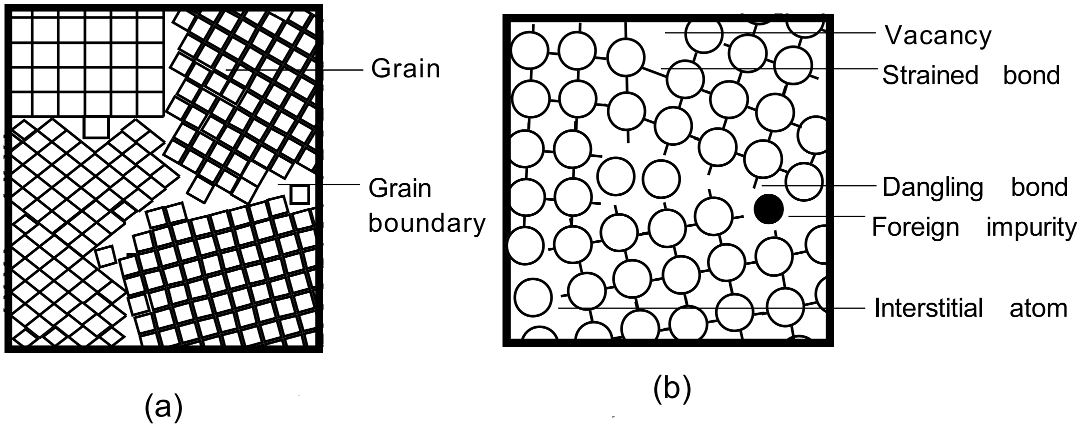

Figure 3.2 (a) Structure of polycrystalline materials showing grain boundary (b) The grain boundaries have dangling bonds, vacancies, misplaced atoms, and strained bonds [38].

3.3 Amorphous Selenium (a-Se)

Amorphous selenium (a-Se) is one of the well studied photoconductor because its alloys have been used in photocopying industries for decades. Currently, stabilized a-Se is one of the preferred photoconductor materials to be used in direct conversion flat-panel X-ray detectors, since it can be easily coated over a large area panel by convention vacuum deposition technique [18]. The atomic number (*Z*) of selenium is 34, and it has six valence electrons. The density of a-Se is 4.3 g/cm^3, the relative permittivity, $\varepsilon_r = 6.7$, and the energy gap, $E_g \sim 2.22$ eV. Pure a-Se crystallizes over time which may vary from months to year depending on the temperature and ambient condition and hence, unsuitable as an X-ray photoconductor. It has been found that alloying pure a-Se with Arsenic (As) can reduce the crystallization time significantly. The atoms of As ($Z = 33$) have three valence electrons. The triply bonded As atoms link Se chains, which causes sufficient increase in viscosity to hinder crystallization of a-Se over the time scale of interest. However, addition of As introduces deep hole traps and hence, reduces the hole lifetime. The As induced deep hole trap can be compensated by doping with a few parts per million (ppm) halogen. Typically Chlorine (Cl) is added for this purpose. The a-Se is called stabilized when it is alloyed with about 0.2−0.5% As and doped with 10−40 ppm Cl [39].

Selenium is located in the group VI of periodic table. The elements of this group are commonly called chalcogens. The electronic structure of Se is [Ar] $4s^2 3d^{10} 4p^4$. Among the six valence electrons, two electrons located in the s-state do not participate in bonding, and form a lone-pair or non-bonding state. Two electrons located in one of the p-states also form a lone-pair. Hence, only two electrons in the p-states are available for covalent bonding with other atoms. These two singly occupied p-states also break into bonding and anti-bonding states. Hence, the atomic coordination of Se is two with an optimum bond angle of 105°. This represents the lowest energy configuration of the Se atom. Selenium form chain-like structures because of the divalent bonding configuration. The trigonally bonded atoms (elements from groups IV or V in the periodic table) can be added to cross-link the divalent chains. This provides stability in the three-dimensional structure of the amorphous solid.

A common feature of all amorphous chalcogenide solids is the presence of structural defects due to the unsatisfied atomic bonds. There are some under-coordinated or over-coordinated atoms, since they cannot satisfy their individual valence requirement. Amorphous selenium is no exception, although the two-fold coordinated neutral structure discussed above represents the lowest energy bonding state. The possible bonding configurations of selenium atoms are shown in Fig. 3.3. The energy of a lone-pair orbital is taken as the zero energy. As a first approximation, the energy per electron of any bonding orbital is taken $-U_B$. Anti-bonding orbitals are always energetically pushed up more than bonding orbitals are pushed down. Thus the energy of an anti-bonding orbital will be $-U_B + \Delta U$, where $U_B >> \Delta U > 0$. The presence of an additional electron on an atomic site requires an additional energy due to the electronic correlation [40]. The electronic correlation is the repulsion of coulombic field between the electrons on the same site. The correlation energy of extra electron in a lone-pair orbital (U_{LP}) is higher than that in an antibonding orbital (U_{AB}), and $U_B >> (U_{LP}, U_{AB})$ [41].

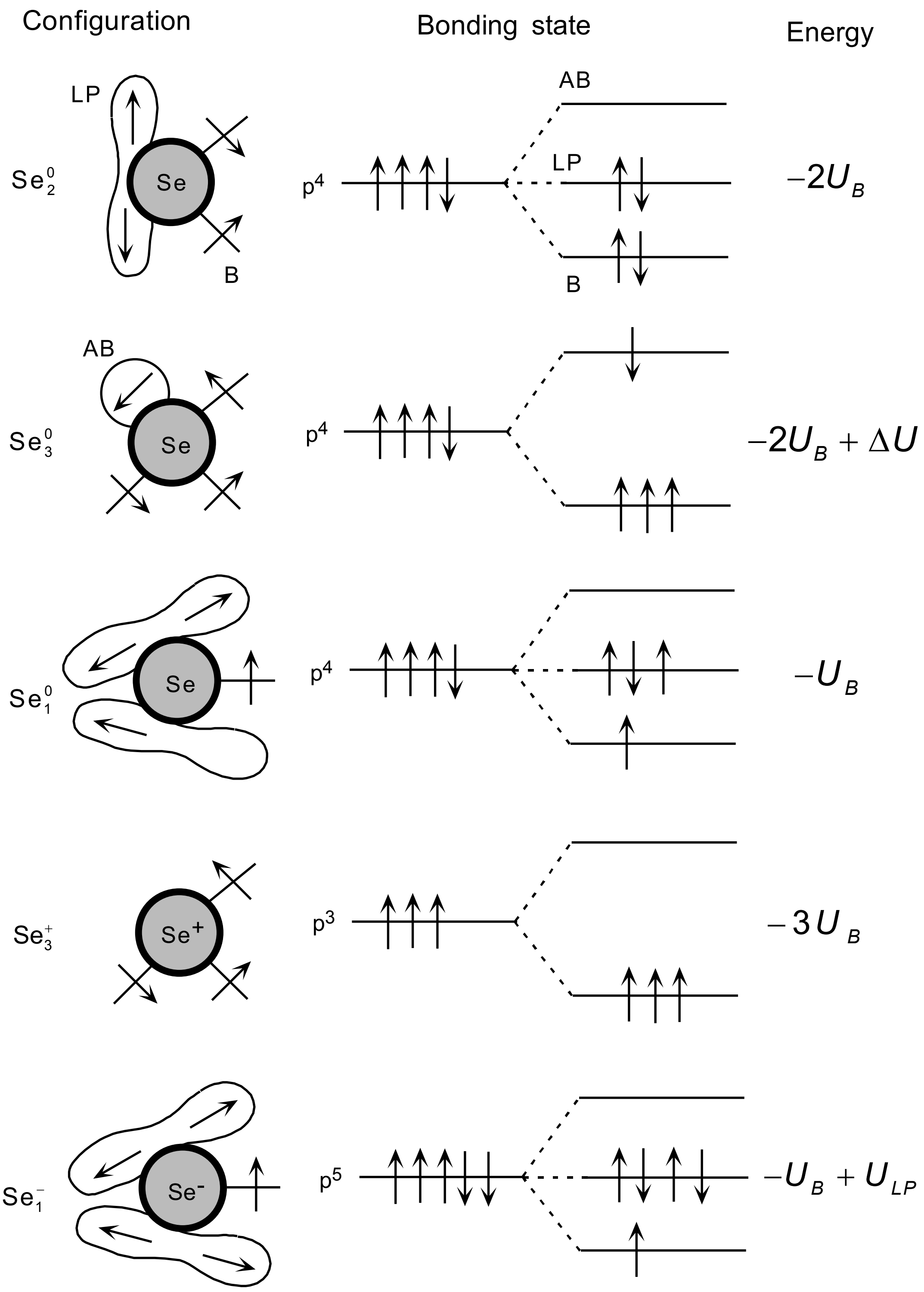

Figure 3.3 Structure and energy of simple bonding configuration for Se atoms. In configuration, straight lines represent bonding (B) orbitals, lobes represent lone-pair (LP) orbitals, and circle represents anti-bonding (AB) orbitals [40, 41].

The lowest energy configuration Se_2^0 is considered as normal structure, and its energy is – 2U_B. The other possible configurations are considered as defects. The trigonally coordinated Se_3^0 has three valence electrons in bonding states and one electron in an anti-bonding state. Its energy is – 2U_B + ΔU, and hence, it is the lowest energy neutral defect. However, this configuration is unstable [42]. The neutral dangling bond or chain end configuration, Se_1^0 has only one electron available for bonding. It costs full bond energy – U_B and hence, energetically unfavorable. A chain end Se_1^0 can lower its energy by approaching an Se_2^0 atom. This interaction creates an Se_3^0 atom, and can release more energy. Consider the reaction,

$$2Se_3^0 \rightarrow Se_3^+ + Se_1^- \tag{3.1}$$

The left side of Eq. 3.1 has a total energy – 4U_B + 2ΔU and the right side has a total energy – 4U_B + U_{LP}. The correlation energy, U_{LP}, is less than 2ΔU and hence, the reaction is energetically favorable. Therefore, the lowest energy structural defect is a pair of charged centers of the type Se_1^- and Se_3^+, which are known as valence alternation pair (VAP). If Se_1^- and Se_3^+ are in close proximity, they are called intimate valence alternation pair (IVAP). A schematic representation of a typical a-Se structure with IVAP centers is shown in Fig. 3.4. These over-coordinated and under-coordinated atoms (VAPs or IVAPs) are thermodynamically derived charged structural defects. The overall structure of Se would appear neutral because of close proximity of positive and negative defects in the IVAP centers. It is believed that the deep trapping of carriers in a-Se photoconductor films is due to these VAPs or IVAPs. These defect states in a-Se can be created by irradiation [43, 44]. The addition of impurities into a-Se can also create charged or neutral defect states and hence, the charge transport properties of a-Se can possibly be controlled by suitably alloying a-Se with other elements.

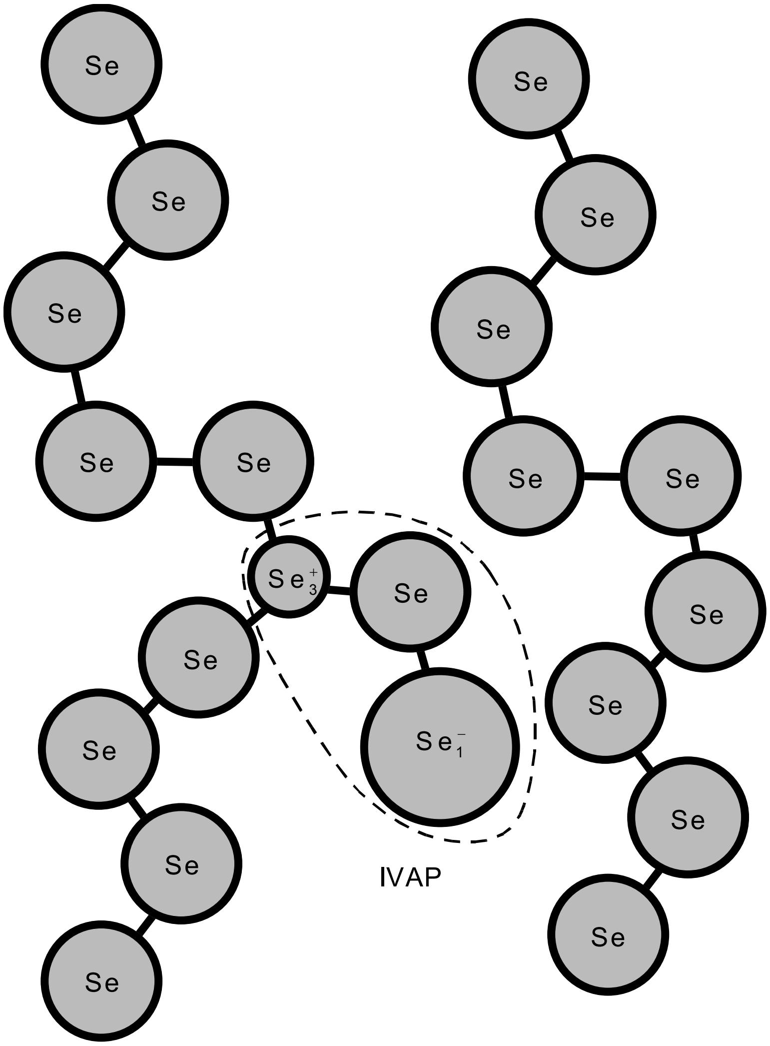

Figure 3.4 Schematic illustration of a-Se structure showing an intimate valence alternation pair (IVAP) defect [17].

In amorphous semiconductors potential is not periodic. Hence, familiar Bloch solutions for the wavefunction to Schrödinger's equation do not apply. A weak disorder potential causes a small perturbation of the wavefunctions, and has the effect of electron scattering. In amorphous semiconductor, an increasing disorder potential causes such frequent scattering that the wavefunction loses phase coherence over a distance of one or two atoms. The multiple scattering of electrons by disorder forms localized states below a certain energy E_C as shown in Fig. 3.5. The schematic wavefunctions in the localized and in the extended states are also shown. The tail of localized states lie at the band edges which decreases almost exponentially, and extends into the forbidden gap. The density of band tail states is low compared to the central region of the band. This implies that the same energy states in the band tail region are well separated in the lattice site and hence, the tunneling probability between these sites becomes small [45]. Thus, the state becomes localized. The boundary (E_C) between the localized state and the extended state is called the mobility edge, which derive its name because at zero temperature, only electrons above E_C are mobile and contribute to the conduction.

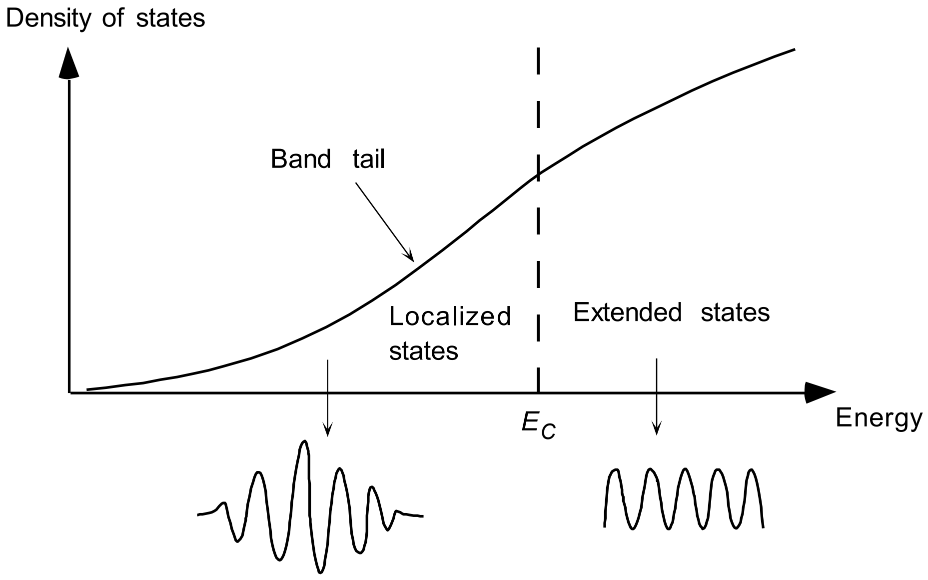

Figure 3.5 Schematic illustration of the localized state and the extended state together with their wavefunctions [45].

The presently accepted model of the electronic density of sates for a-Se is shown in Fig. 3.6. According to this model the mobility gap for a-Se is effectively 2.22 eV. The localized states near the band edges are called shallow traps. The electron and hole shallow traps are located ~0.35 eV below the conduction band (E_C) and ~0.28 eV above the valence band (E_V), respectively [46]. The localized states near the Fermi level are called deep traps. Both shallow and deep states are due to various structural defects. These defects are thermodynamically stable at room temperature.

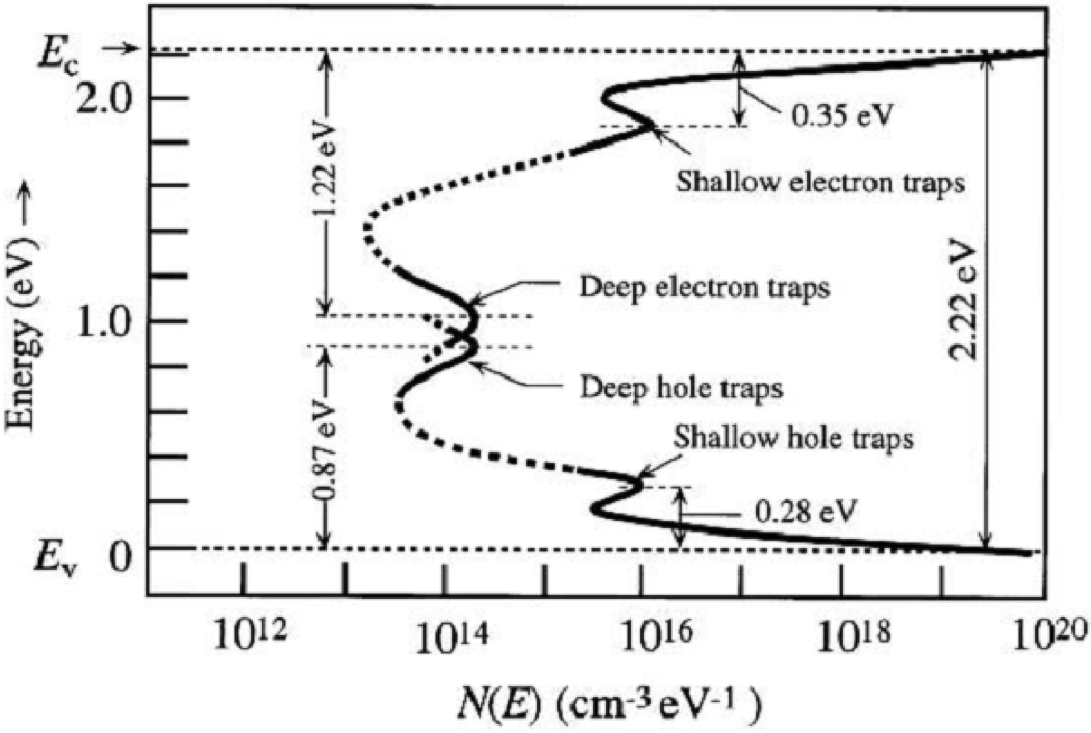

Figure 3.6 Electronic density of states for a-Se. The states between conduction band (E_C) and valence band (E_V) are localized states [17, 46].

Figure 3.7 shows the interactions with shallow and deep traps as the carrier drifts across the a-Se photoconductor. Deep traps actually prevent the carriers from crossing the photoconductor. The trapping and release events in shallow traps reduce the mobility of the carrier and hence, the effective mobility μ of carriers is defined by [47, 48],

$$\mu = \mu_0 \frac{\tau_{cs}}{\tau_{cs} + \tau_{rs}}, \tag{3.2}$$

where μ_0 is the mobility of the carrier in the extended states, and $\tau_{cs(rs)}$ is the average capture (release) time in shallow traps. The capture time is the average time that a free carrier drifts in the extended states before becoming trapped in a shallow trap center. The release time is the average time that a carrier stays in a trap before being released back into the transport band. The carrier remains in a shallow trap for a very short time. The thermal activation process mainly release the trapped carrier from a shallow trap. The carriers may encounter several capture and release events in shallow traps while crossing the detector thickness. The room temperature carrier mobilities in the extended states are $\mu_{0h} \approx 0.3$ cm^2/V-s and $\mu_{0e} \approx 0.1$ cm^2/V-s, where subscript h and e represents hole and electron, respectively [49]. At room temperature, the effective hole mobility, μ_h is about 0.12 cm^2/V-s, whereas the effective electron mobility, μ_e is ~0.003 – 0.006 cm^2/V-s [16]. Therefore, the effective electron mobility is ~20 – 40 times smaller than the effective hole mobility. The value of μ_e tends to decrease with As addition, but μ_h does not change with the addition of As or Cl.

The trapping in the shallow localized states reduces the carrier mobility, whereas the trapping in the deep localized states hinder the carriers from traversing the photoconductor. The localized states peaking at 0.87 eV and 1.22 eV in Fig. 3.6 are responsible for the deep trapping of holes and electrons respectively. The deeply trapped carrier remains immobile until a lattice vibration yield sufficient energy to excite the trapped carrier back into the transport band. The carrier release time from a deep trap state is very long compared to the carrier transit time under high electric field. As a result, carriers are effectively removed from conduction due to deep trapping. Therefore, the deep trap concentration controls the carrier life-time. Various factors such as source materials, additional impurities, and preparation methods strongly control the carrier life-time.

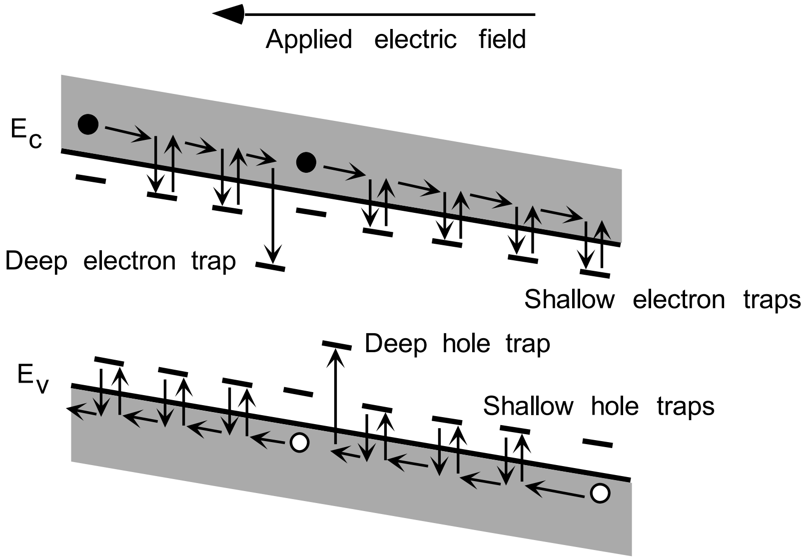

Figure 3.7 Illustration of the carrier movement in the transport bands (E_C and E_V) of a-Se, which is limited by the presence of shallow and deep traps.

The temperature of a-Se substrate during the evaporation process has a dramatic effect on the hole life-time, τ_h, which drops sharply with decreasing substrate temperature [32]. The substrate temperature has no marked effect on the electron life-time, τ_e. Addition of impurity (e.g., As) reduces hole life-time but does not change the hole mobility [50]. Concurrently, As addition increases the electron life-time whereas reducing the electron mobility. However, the electron range ($\mu\tau$ product) increases with As content. The addition of Cl increases the hole life-time, but reduces the electron life-time. The drift mobility of both carriers remains same after Cl doping. The influence of Cl doping on carrier ranges is more pronounced than that of As doping. In stabilized a-Se, $\tau_h \sim 10 - 500$ μs and $\tau_e \sim 100 - 1500$ μs [16].

The release time of the trapped carrier is related to the trap depth E_t by,

$$\tau_r = \left(\frac{1}{v_0}\right) e^{\frac{E_t}{kT}} \tag{3.3}$$

where k is the Boltzmann constant, T is the absolute temperature, and v_0 is the phonon frequency. Taking $v_0 = 10^{12}$/s, T = 300° K (room temperature), and $E_t \sim 0.87$ eV, the release time constant for deeply trapped holes is less than 7 minutes [46, 51]. The release time constant for deeply trapped electrons varies from few hours to several hours. The release time constant for shallow trapped electrons is ~ 100 ns.

The dark current in a-Se photoconductors tends to be relatively small compared with many other competing photoconductors. It has a dark resistivity of the order of 10^{15} Ω-cm which corresponds to a long dielectric relaxation time (~ 20−60 minutes) [11]. At typical operating field (~ 10V/μm) the dark current density below 1 nA/cm^2 in metal/a-Se/metal detectors has been reported [52]. In multilayer a-Se detector structure, the dark current density is <100 pA/cm^2. The detail of the dark current reduction mechanisms in multilayer structure will be discussed in chapter 4.

It is mentioned in chapter 2 that the electron-hole-pair creation energy, $W_{\pm}$ in a-Se depends on the applied electric field. Based on experimental data, it is found that $W_{\pm}$ strongly depends on the electric field, F_0 but weekly depends on the incident X-ray photon energy, E_{ph} [23, 31]. At a given energy, $W_{\pm}$ follows an empirical relationship given by [53],

$$W_{\pm} \approx W_{s\pm} + \frac{B(E_{ph})}{F_0^m} \tag{3.4}$$

where $W_{s\pm}$ is the saturated EHP creation energy (at infinite applied electric field), $B(E_{ph})$ is a photon energy dependant constant, and m typically varies from 0.7 to 1. The field dependence of $W_{\pm}$ is possibly due to the recombination of the generated EHPs. The energetic primary electron creates many EHP, but only a fraction of those EHPs are collected, and the rest are lost due to trapping and recombination.

There are three possible sources of recombination; (i) bimolecular recombination between drifting electrons and holes, (ii) geminate recombination, and (iii) columnar recombination. These three recombination processes are illustrated in Fig. 3.8. In bimolecular recombination, the recombination rate is proportional to the product of hole and electron concentrations. Hence, the collected charge shows a square root dependence on the X-ray intensity. However, it has been found that the collected charge in a-Se increases linearly with the intensity of the X-rays [54]. Hence, this type of recombination has been ruled out. In geminate recombination, the simultaneously generated electron and its hole twin face a strong mutual Coulombic force, and they can, eventually recombine. Columnar recombination involves the recombination of non-geminate electrons and holes generated close to each other within the columnar track of a primary electron, i.e. bimolecular recombination within a track. Research is still going on to find the dominant recombination mechanism between the geminate and the columnar process behind the field dependency of $W_{\pm}$ [30, 55].

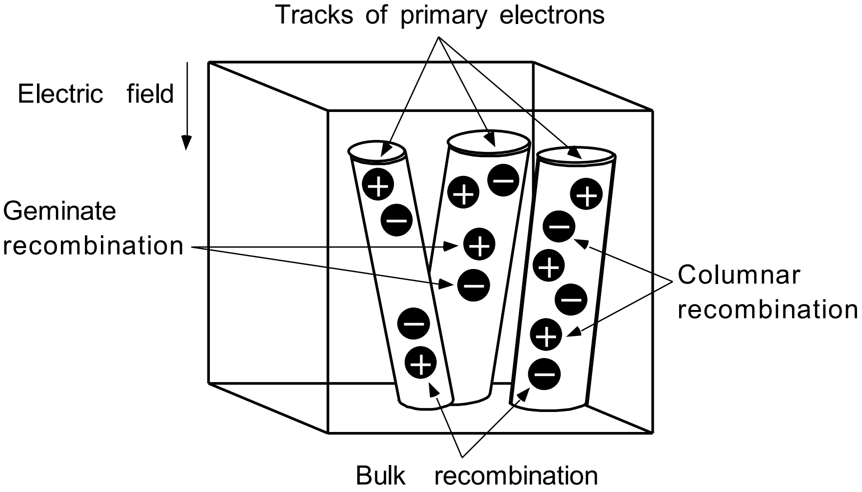

Figure 3.8 Illustration of various recombination mechanisms in a-Se.

3.4 Amorphous Silicon (a-Si)

Hydrogenated amorphous silicon (a-Si:H) p-i-n photodiodes are used in large area indirect conversion flat-panel X-ray detectors. It is usually deposited by plasma decomposition of silane (SiH_4) gas. The hydrogen passivates the dangling bond, and relieves the local stress in the network. About 5−10 atomic percent of hydrogen is bonded to the silicon atoms [56]. Most of the hydrogen form Si−H bonds, either isolated or on the surface of small voids. This removes the corresponding electronic states in the band gap, and thus eliminates most of the trapping and recombination centers. The density of hydrogen free a-Si is very close to that of crystalline silicon (2.33 g/cm^3). However, the density of a-Si:H varies significantly depending upon both the content and the state of the hydrogen [57]. The relative permittivity, ε_r is 11.8, the mobility gap, $E_g \sim 1.75$ eV and the resistivity is 10^{11} Ω-cm [56]. The distinction between direct and indirect is absent in a-Si:H because conservation of momentum no longer applies to electronic transitions. Despite having a larger band-gap, the optical absorption of a-Si:H is actually larger than crystalline silicon in the region of the band edge because of the indirect gap in the crystal.

The atomic number (*Z*) of silicon is 14 and it has four valence electrons. In a crystalline silicon structure, the atoms are fourfold coordinated in a tetrahedral bonding symmetry with a bond angle of 109°. The short range bonding structure of a-Si:H is tetrahedral, but in long range there is significant deviation of the bond lengths and the bond angles. Among the four valence electrons, two electrons exist in the s-state, and two in the p-state as shown in Fig. 3.9. However, only two covalent bonds can be formed with neighboring silicon atoms with that bonding configuration. In order to maximize the number of possible bonds, the s and p states combine to form the four sp^3 hybrid orbitals, located between the s and p levels. This permits bonding with up to four silicon atoms at the tetrahedral angles. When the sp^3 hybrid orbital forms during bonding, another atom contributes a second electron to the state, and the interaction between the two electrons lowers the energy of the state. Therefore, the sp^3 orbital splits into bonding and anti-bonding orbitals. The bonding orbitals form a valence band filled with electrons, and the anti-bonding orbitals form an empty conduction band as shown in Fig. 3.9. The nonbonding orbitals, such as dangling bonds, are not split by the bonding interaction and give states in the mobility gap. The midgap defect density is ~10^{15}–10^{16} /cm^3/eV [56]. Dangling bond defects control the trapping and recombination of carriers, and hence determine the carrier lifetimes, photoconductivity, and depletion layer width of Schottky barriers and p-i-n junctions.

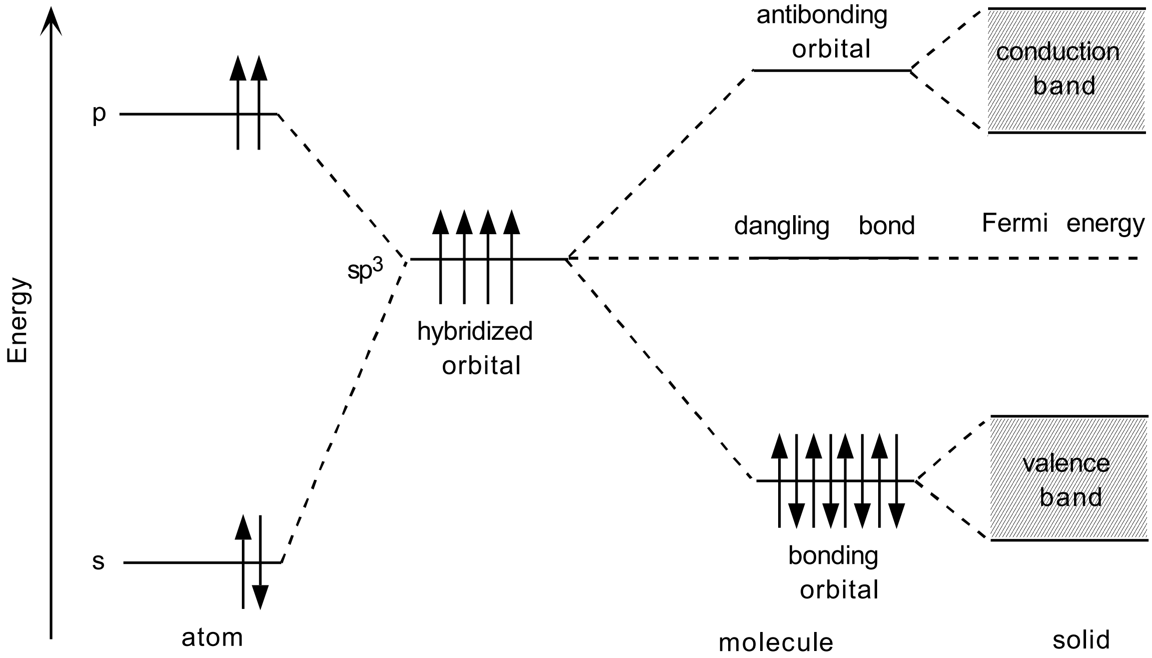

Figure 3.9 Schematic molecular orbital configuration of silicon [57].

In a-Si:H, free electrons and holes have a scattering length of about an interatomic spacing because of scattering from the random potential fluctuation, and consequently a free electron mobility of only about 10–20 cm^2/V-s compared to about 500 cm^2/V-s in crystalline silicon [56]. Figure 3.10 shows a schematic density of states of a-Si:H. There is an approximately parabolic region above the mobility gap. From Fig. 3.10 it is evident that, the conduction band tail is narrower than the valence band tail. Therefore, electrons have a higher mobility than holes. The band mobilities of carriers are μ_{0e} = 10−20 cm^2/V-s and μ_{0h} = 1 cm^2/V-s, where subscript *e* and *h* represents electron and hole, respectively [58]. The room temperature effective electron mobility, μ_e is ~ 0.25−1 cm^2/V-s, whereas the effective hole mobility, μ_h is ~0.003 cm^2/V-s [56, 59].

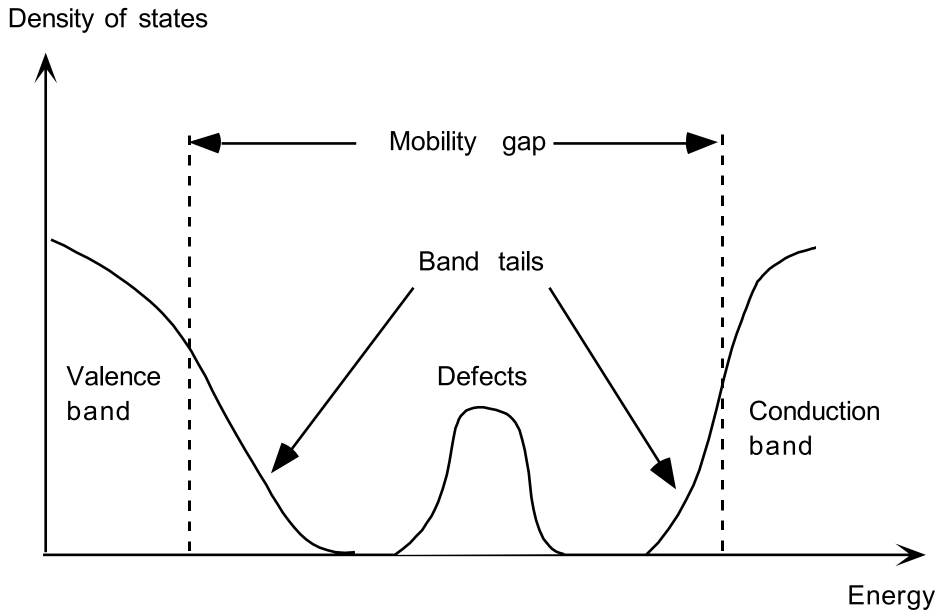

Figure 3.10 Schematic density of states of a-Si:H [56].

In undoped a-Si:H, the defects are neutral which can trap both electrons and holes. However, the capture cross section for holes is greater. Therefore the $\mu\tau$ value of holes is 5−10 times smaller than that for electrons. Typically, $\mu_e\tau_e = 10^{-6}$–10^{-5} and $\mu_h\tau_h$ = (0.5−5) × 10^{-8} cm^2/V [58]. The Fermi energy of undoped a-Si:H is above the middle of band gap by 0.1−0.2 eV and thus, the undoped a-Si:H is slightly n-type [60]. The n-type and p-type a-Si:H are most commonly achieved by adding phosphine (PH_3) and diborane (B_2H_6) to plasma gas. The doping causes a high density of charged dangling bond defects. These charged defects are positive and negative in n-type and p-type materials, respectively. In doped a-Si:H, the defect density increases by 2−3 orders of magnitude. However, the doped layers provide rectifying contacts. For this region, doped layers are mainly chosen for junctions rather than active layers. Therefore, the p-i-n structure is preferred for a-Si:H sensors. The minority carrier lifetime in doped a-Si:H is so small that most holes generated in the n-layer and electrons in the p-layer recombine before they can cross the reverse bias junction. The dark current in a-Si:H p-i-n photodiode is on the order of 10−100 pA/cm^2. It has been found that the dark current decays with time after the application of bias voltage. The decay time constant is ~100 s [61].

Although hydrogen is necessary for the good electronic properties of a-Si:H, it does have some harmful effects. Light can induce defects by breaking of Si−H bonds. The released energy of electron-hole recombination results in breaking the Si−H bond. After breaking of Si−H bond, the free hydrogen can move. The light induced meta-stable changes can be reversed by annealing at elevated temperatures of about 200°C. However, annealing also speeds up the defect generation. Meta-stability is also induced by current flow and charge accumulation. Several studies have been done in order to minimize the effects of meta-stability in devices by careful design, especially in solar cells. The TFTs and sensors based on a-Si:H are stable at room temperature, but they become increasingly unstable at elevated temperature.

3.5 Polycrystalline Mercuric Iodide (poly-HgI_2)

Polycrystalline mercuric iodide (poly-HgI_2) is a promising photoconductor to be used in direct conversion flat-panel X-ray detectors. Fabrication of large area panel with poly-HgI_2 is technologically feasible [12]. It has a high density (6.3 gm/cm^3) and atomic number, and low EHP creation energy ($W_\pm$ ~ 5 eV) [14, 62]. Thus a better X-ray sensitivity can be achieved with a thinner layer of HgI_2 at a lower electric field compared to an a-Se detector. However, HgI_2 based detector exhibits nonuniform response from pixel to pixel due to the adverse effect of large grain size. The ploy-HgI_2 film can be deposited on to the AMA by both physical vapor deposition (PVD) and particle-in-binder (PIB) methods. In either case, a thin layer of insulating polymer is used between the HgI_2 layer and the pixel electrodes to prevent the chemical reaction as well as to reduce the dark current. A bias electrode is deposited on the top of the HgI_2 film followed by a polymer encapsulation layer. The encapsulation is required to prevent evaporative degradation of HgI_2 layer, and to assure long-term stability of the detector. The resistivity of ploy-HgI_2 is ~10^{13} Ω-cm and the band gap energy is 2.1 eV [63]. The detector sizes of 20 cm × 25 cm (1536 × 1920 pixels) and 9.8 cm × 9.8 cm (768 × 768 pixels) have been reported using PVD and PIB method, respectively [14, 64]. The thickness of HgI_2 varies from 80−400 μm and the grain size varies from 20−60 μm.

The dark current of HgI_2 detectors increases super-linearly with the applied bias voltage [64]. The dark current also depends on the fabrication method and the operating temperature. The dark current of a PVD HgI_2 detector shows a strong dependency on the operating temperature. The dark current increases by a factor of ~2 for each 6°C rise in operating temperature [65]. It has been found that the values of dark current at 0.95 V/µm varies from ~0.2 nA/cm^2 at 10°C to ~18 nA/ cm^2 at 35°C. The dark current for medical imaging should be less than 1 nA/cm^2. The wide variation of dark current in PVD HgI_2 detectors emphasizes that these detectors should be operated at relatively low electric fields (preferably ~0.5 V/µm to ~0.8 V/µm) and relatively low temperature (< 25°C). The dark current in the PIB HgI_2 detectors is an order of magnitude smaller than in PVD detectors and more stable against temperature variation. However, the sensitivity of PIB detectors is ~2−4 times less compared to PVD detectors. This is possibly due to lower charge collection efficiency since the carrier ranges ($\mu\tau$ values) are lower for PIB detectors.

In HgI_2 detectors, electrons have much longer ranges than holes. Hence the radiation receiving electrode is negatively biased to have higher sensitivity. The electron range in detectors deposited by PIB method is ~10^{-6}−10^{-5} cm^2/V. The electron $\mu\tau$ in the PVD detectors is ~10^{-5}−10^{-4} cm^2/V [66]. The reason for higher electron range is that, the PVD HgI_2 layer grows in a columnar structure parallel to the growth direction (perpendicular to the substrate) [67]. A charge carrier may drift along a column without having to pass grain boundary regions where it can be lost due to excess trapping and/or recombination. It is reported that, the electron range increases with the grain size in the PVD sample [68]. A sample with larger grain size may have fewer defects at the grain boundary, which may cause higher electron range. However, low electron $\mu\tau$ is observed in large grain PIB samples. Hence another mechanism might screen the grain size dependence in PIB detectors. Larger grain sizes may cause nonuniform response over the entire detector area. The sensitivity variation from pixel to pixel decreases the dynamic range of the detector. It is found that, the grain size must be much smaller than the pixel size to get an acceptable uniform response [68].

3.6 Summary

A summary of the material properties of these potential photoconductors and the photodiode for X-ray image detectors are given in Table 3.1.

Table 3.1 Comparison of material properties of some potential X-ray photoconductors and photodiode for X-ray image sensors.

Photoconductor/ Photodiode	Preparation	E_g (eV)	Density (g/cm^3)	Resistivity (Ω-cm)	Electron $\mu_e\tau_e$ (cm^2/V)	Hole $\mu_h\tau_h$ (cm^2/V)
Stabilized a-Se	Vacuum deposition	2.22	4.3	10^{14}–10^{15}	3×10^{-7} -10^{-5}	10^{-6} – 6×10^{-5}
a-Si:H	Plasma-enhanced chemical vapor deposition	1.75	2.3	~10^{11}	10^{-6}–10^{-5}	5×10^{-9} – 5×10^{-8}
Poly-HgI$_2$	Physical vapor deposition	2.1	6.3	~10^{13}	10^{-5}–10^{-4}	10^{-6}–10^{-5}
	Particle-in-binder	2.1	6.3	~10^{13}	10^{-6}–10^{-5}	10^{-7}

CHAPTER 4

DARK CURRENT MECHANISMS IN IMAGING DETECTORS

The current that flows through the detector due to the applied bias without any X-ray irradiation or light is called dark current. The dark current should be as small as possible (preferably smaller than 100 pA/cm^2) for diagnostic X-ray imaging applications, since it reduces dark current shot noise, and improves dynamic range of the detector. In this chapter, a theoretical model to describe the dark current behavior in a-Se based direct conversion flat-panel X-ray image sensors has been developed. The theoretical dark current model has been validated with the measured and the published experimental results for different a-Se detector structures (e.g., n-i-p, n-i, p-i-n). The concept of the modeling of dark current has also been applied to hydrogenated amorphous silicon (a-Si:H) p-i-n photodiodes, and poly-HgI_2 detectors. Note that, the a-Si p-i-n photodiodes are used in indirect conversion flat-panel detectors.

4.1 Sources of Dark Current

In imaging detectors there are three components of dark current; bulk thermal generation, contact injection, and edge leakage. The detector material is either amorphous or polycrystalline. In these materials, there are localized states in the energy band-gap. The bulk component of dark current originates from charge generation through gap states, commonly known as the thermal generation current. Electrons are excited from the valence band to empty gap states, and from filled traps to the conduction band. These excitations generate electron-hole pairs. The generated electron-hole pairs are separated and collected by the internal field. This mechanism of charge generation also determines the quasi-Fermi energy position under conditions of deep depletion [61]. Depletion of carriers occurs when the sample has an occupied trap sates under zero bias (e.g., a-Si:H).

The contact component of dark current in imaging detectors arises due to injection of carriers from metal-semiconductor or semiconductor-semiconductor (p-i/n-i) junctions. The carrier injection depends on interface electric fields, barrier height, interface band bending, and interface states. The carrier injection mechanism in low-mobility semiconductors (typically $\mu < 1$ cm^2/V-s) is described by the diffusion theory [69]. However, at a very high field the carrier injection modeled by the thermionic-emission-diffusion theory is more applicable. The carriers may tunnel through the barrier if the effective barrier width is small. However, in imaging detectors appropriate metal-semiconductor and (or) semiconductor-semiconductor (p-i/n-i) junctions are created to minimize the tunneling current.

The edge leakage arises due to the areal dependence of the current, since the edge leakage current is proportional to the device size, while the bulk or contact currents are proportional to the device area. Therefore in large-area imaging detectors the edge leakage tends to be least significant [70, 71].

4.2 Dark Current in a-Se X-ray Image Detectors

The dependence of current on the applied voltage ($I-V$ characteristics) in metal/a-Se/metal structures has been reported in several works during the 1960s and 1970s. Most of these studies have explained the observed steady-state dark $I-V$ characteristics in terms of bulk limited currents [72, 73]. However, there is experimental evidence against the dark current in metal/a-Se/metal structures being bulk limited [74]. Another work has reported that, the dark current in Au/a-Se/Cu device is limited by either Schottky emission from the electrode or Poole-Frenkel effect [75]. Further, all these works used pure a-Se or material with unspecified charge transport properties due to its earlier applications as xerographic photoreceptors [17].

Johanson *et al.* [24] have studied both transient and steady-state dark current in metal/intrinsic a-Se/ITO devices with stabilized a-Se samples (which are suitable for direct conversion X-ray image sensors). They have found that, the dark current for some metal contacts follows an empirical power law relation at high applied electric field, F_0. That is, the dark current density can be expressed as,

$$J_d \propto F_0^n \tag{4.1}$$

where $F_0 = V/L$, V is the applied voltage and L is the detector thickness. The parameter n varies from ~1 to 5. The authors found that, the $I-V$ characteristics do not follow a simple power law for many contact metals. In this work, the existence of long transients (~1 hour) after the application of the bias has been reported. It has been found that, the dark current decay with time immediately after the application of a bias voltage. The authors cannot explain dependency of the dark current on the type of the metal. Therefore, a physical model is developed in this thesis to explain the dark current behavior in a-Se based X-ray detectors.

As mentioned in Chapter 1, the magnitude of dark current in metal/a-Se/metal structure is intolerably high (~1–100 nA/cm^2). The dark current in a-Se detectors may have two origins; (i) thermally generated carriers in the bulk, and (ii) carrier injections from the metal contacts to the selenium layer. The thermally generated carrier in the bulk is negligible due to the large mobility gap (2.2 eV) of a-Se [46]. It is therefore, believed that the dark current is mainly controlled by the injection of carriers from the metal contacts. The injection current can be minimized by fabricating a thin insulating dielectric layer between the a-Se photoconductor and the metal electrode [76]. The dielectric layer enhances the effective barrier for injecting carrier from electrodes into a-Se layer. However, the drifting carriers accumulate at the dielectric/a-Se interfaces. These carriers must be eliminated before subsequent exposure. This is achieved by flooding the detector with light to eliminate the trapped charge in the dielectric layer. The requirement of a system reset cycle makes this technique incompatible with real time imaging (e.g., fluoroscopy). The X-ray generated charge is also trapped in the dielectric layer, and thus the X-ray sensitivity of the detector is reduced. The dielectric layer must be thick enough to prevent tunneling of carriers. However, more X-ray generated charge will be lost due to trapping in such a thick dielectric layer.

A more efficient technique to reduce the dark current in a-Se based X-ray imagers is the use of doped a-Se to serve as blocking layers. The physical structure is similar to a p-i-n photodiode. A multilayer a-Se based detector structure is shown in Fig. 4.1. The p and n layers are usually thin (few microns) compared with the i-layer (200−1000 μm). Thus the X-rays are absorbed mainly in the i-layer. The n-layer is produced from a-Se which is appropriately doped that can easily trap holes, but allow the transport of electrons (ideally hole lifetime, $\tau_h = 0$ and electron lifetime, $\tau_e = \infty$). Similarly, the p-layer is produced from a-Se which is appropriately doped that can easily trap electrons, but allow the transport of holes (ideally hole lifetime, $\tau_h = \infty$ and electron lifetime, $\tau_e = 0$). Thus the concentrations of deep trap centers for electrons and holes are very high in the p and n layers, respectively [20]. The i-layer transports both holes and electrons. The carrier schubweg in the i-layer is much longer than the thickness of the photoconductor. The schubweg, $\mu\tau F_0$, is defined as the distance that a carrier drifts before it is deeply trapped and unavailable for conduction, where μ is the drift mobility, τ is the deep trapping time or lifetime, and F_0 is the applied electric field.

The intrinsic a-Se is slightly p-type and thus the Fermi level E_F at zero bias is ~ 0.045 eV below the mid-gap [46]. The definitions of p-type and n-type a-Se are different from conventional semiconductor physics, and are based on the relative magnitude of mobility-lifetime product, $\mu\tau$. In case of n-type a-Se $\mu_h\tau_h << \mu_e\tau_e$, although the exact position of the Fermi level is not known. The subscripts *e* and *h* represent electrons and holes, respectively. The thin n-layer is usually an alkali (e.g., Sodium (Na)) doped a-Se, which is alloyed with a few percentages (up to 10%) of Arsenic (As) for stability (i.e., to prevent crystallization). The p-layer is usually a halogen (Cl) doped a-Se, and also alloyed with some As for stability. However, in practical devices the p-layer is commonly made from As_2Se_3, which is p-type.

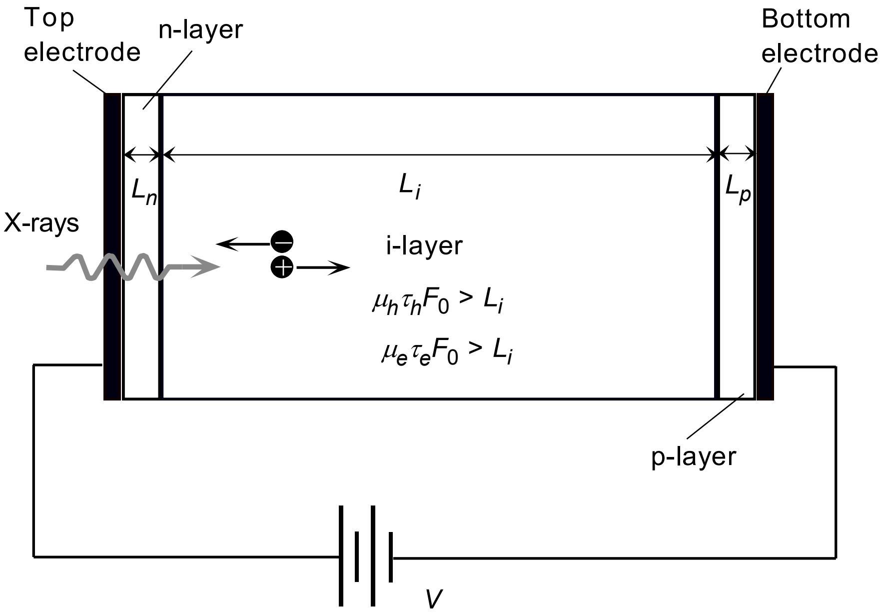

Figure 4.1 A multilayer a-Se structure. For n-layer $L_n << L_i$, $\mu_h\tau_hF_0 < L_n$, $\mu_e\tau_eF_0 > L_n$. For p-layer $L_p << L_i$, $\mu_h\tau_hF_0 > L_p$, $\mu_e\tau_eF_0 < L_p$. For i-layer $\mu_h\tau_hF_0 > L_i$, $\mu_e\tau_eF_0 > L_i$.

The multilayer a-Se based detectors can be n-i-p or p-i-n type depending on the type of collected charge by the bottom (or pixel) electrode. The first letter in the multilayer structure notation refers to the layer next to the X-ray receiving electrode. In both cases the structure is reverse biased. In n-i-p detector, the top electrode is positively biased and

X-ray generated holes are collected at the bottom electrode. In p-i-n detector the top electrode is negatively biased and electrons are collected at the bottom electrode. After applying the bias, the carriers are injected from the metal electrodes to a-Se layers. The injected holes from the positively biased electrode are trapped in the n-layer, and the injected electrons from the negatively biased electrode are trapped in the p-layer. The carrier injection from the metal to the semiconductor depends on the internal electric field at the metal/a-Se interface. The trapped carriers in the blocking layers reduce the electric fields at the metal/a-Se interfaces, which reduces the subsequent carrier injections, and thus reduces the dark current. Concurrently, the electrons and holes created in the i-layer by the absorption of X-ray will pass without trapping through the p and n layers, respectively.

The theoretical modeling of transient and steady-state dark current behavior in multilayer a-Se detector structures will be discussed in the following sub-sections.

4.2.1 Dark Current Model for n-i-p/p-i-n Structure

In a-Se based multilayer detector, the contacts are generally blocking in nature, and the carrier injection is mainly controlled by the Schottky emission. After injection, carriers drift in the a-Se layer through shallow-trap controlled transport [77]. It is believed that, the electric field right after applying bias is uniform but quickly becomes non-uniform due to high initial current, and high carrier trapping in the blocking layers. The steady-state electric field profile before applying any radiation in the a-Se based n-i-p structure is shown in Fig. 4.2. The electric field decreases at the metal contacts due to trapping of carriers. Note that electric field in the i-layer increases since the total electric field remains equal to the initial applied electric field (i.e., the area under the electric field profile has to be equal).

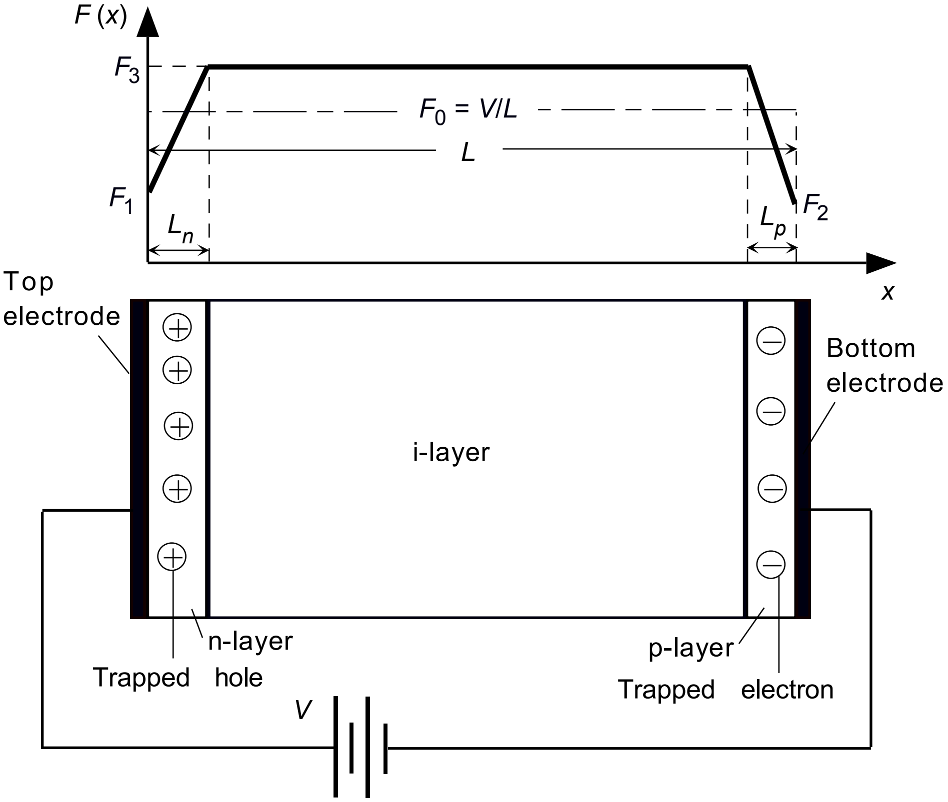

Figure 4.2 A multilayer n-i-p a-Se structure showing time-dependent electric field profile. The dash-dotted line represents the initial uniform electric field and the solid line represents the field distribution sometime after the application of field. L_n is the thickness of the n-layer, L_p is the thickness of the p-layer, and L is the total photoconductor thickness.

It is assumed that the carrier trapping, over a long time, is effectively uniform in the blocking layers and the trapping in the intrinsic layer is negligible as compared to trapping in the blocking layers. This is a reasonable assumption, since the density of deep trap centers for holes in the n-layer is much higher than that in the intrinsic or p-layer and similarly, the density of deep trap centers for electrons in the p-layer is much higher than that in the intrinsic or n-layer [4].

In practical a-Se based detectors, the carrier mobility is independent of electric field under normal operating bias [78, 79]. As a result the drift velocity of the carrier would be proportional to the instantaneous electric field at the metal/semiconductor interface. Therefore, the injected current densities due to hole and electron injections can be written as, [20, 69],

$$J_h(t) = qN_V v_{dh}(t)\left(\frac{v_R}{v_{dh}(t)+v_R}\right)\exp\left\{-\frac{\varphi_h - \beta_s\sqrt{F_1(t)}}{kT}\right\}, \tag{4.2}$$

$$J_e(t) = qN_C v_{de}(t)\left(\frac{v_R}{v_{de}(t)+v_R}\right)\exp\left\{-\frac{\varphi_e - \beta_s\sqrt{F_2(t)}}{kT}\right\}, \tag{4.3}$$

where q is the elementary charge, $F_1(t)$ is the instantaneous electric field at the metal/n-layer interface, $F_2(t)$ is the instantaneous electric field at the metal/p-layer interface, $\beta_s = \sqrt{(q^3/4\pi\varepsilon_{se})}$ is the Schottky coefficient, ε_{se} ($=\varepsilon_0\varepsilon_r$) is the permittivity of the photoconductor, T is the absolute temperature, k is the Boltzmann constant, $v_R = A^*T^2/qN_C$ is the thermal velocity, A^* is the effective Richardson constant, $N_{V(C)}$ is the effective density of states in the valence (conduction) band, $v_d(t) \approx \mu_0 F(t)$ is the instantaneous drift velocity of the injected carriers, μ_0 is the band mobility of carriers, and φ is the effective barrier height for injecting carriers from metal into the a-Se layer considering the effect of surface states. The total injection current density, $J_{inj}(t)$ is the algebraic sum of current densities due to hole and electron injections, and is given by,

$$J_{inj}(t) = J_h(t) + J_e(t) \tag{4.4}$$

Once the carriers are injected into the a-Se layer, they move by drift mechanism (diffusion component of current is negligible compared to its drift component because of very high applied field as described in the appendix A). That is, hole and electron current densities in the a-Se layer can be written as,

$$J_h(t) \approx q\mu_h p(t) F_1(t), \tag{4.5}$$

$$J_e(t) \approx q\mu_e n(t) F_2(t), \tag{4.6}$$

where $\mu_{h(e)}$ is the effective drift mobility of holes (electrons) considering shallow trapping [80]. Therefore, the drifting hole and electron concentrations near the interfaces are,

$$p(t) = N_V \frac{\mu_{0h}}{\mu_h}\left(\frac{v_R}{v_{dh}(t)+v_R}\right)\exp\left\{-\frac{\varphi_h - \beta_s\sqrt{F_1(t)}}{kT}\right\}, \tag{4.7}$$

$$n(t) = N_C \frac{\mu_{0e}}{\mu_e}\left(\frac{v_R}{v_{de}(t)+v_R}\right)\exp\left\{-\frac{\varphi_e - \beta_s\sqrt{F_2(t)}}{kT}\right\}. \tag{4.8}$$

The instantaneous electric field $F_1(t)$ and $F_2(t)$ can be determined by solving the Poisson's equation in the a-Se layers. The instantaneous electric field $F_2(t)$ and $F_3(t)$ shown in Fig. 4.2, can be written as,

$$F_3(t) = F_1(t) + \frac{qp_t(t)}{\varepsilon_{se}} L_n, \tag{4.9}$$

$$F_2(t) = F_3(t) - \frac{qn_t(t)}{\varepsilon_{se}} L_p$$

$$= F_1(t) + \frac{qp_t(t)}{\varepsilon_{se}} L_n - \frac{qn_t(t)}{\varepsilon_{se}} L_p, \tag{4.10}$$

where L_n is the n-layer thickness, L_p is the p-layer thickness, $p_t(t)$ and $n_t(t)$ are the instantaneous trapped hole and electron concentrations in the n- and p-layer, respectively. The boundary condition gives,

$$V = F_0 L = \frac{F_1(t) + F_3(t)}{2} L_n + F_3(t) \times (L - L_n - L_p) + \frac{F_3(t) + F_2(t)}{2} L_p \tag{4.11}$$

where V is the applied bias voltage, and L is the total photoconductor layer thickness. Substituting (4.9) and (4.10) into (4.11), the instantaneous electric field, $F_1(t)$ can be written as,

$$F_1(t) = F_0 - \frac{q}{\varepsilon_{se}} \left[\left(L_n - \frac{L_n^2}{2L} \right) p_t(t) - \frac{L_p^2}{2L} n_t(t) \right] \tag{4.12}$$

Thus, the instantaneous electric field, $F_2(t)$ can be written as,

$$F_2(t) = F_0 - \frac{q}{\varepsilon_{se}} \left[\left(L_p - \frac{L_p^2}{2L} \right) n_t(t) - \frac{L_n^2}{2L} p_t(t) \right] \tag{4.13}$$

The trapping rate equations for holes (in the n-layer) and electrons (in the p-layer) considering trap filling and carrier detrapping from a single discrete state can be expressed as [20],

$$\frac{dp_t(t)}{dt} = C_{th} N_{th} \theta_h \left(1 - \frac{p_t(t)}{N_{th}}\right) p(t) - \frac{p_t(t)}{\tau_{rh}}, \tag{4.14}$$

$$\frac{dn_t(t)}{dt} = C_{te} N_{te} \theta_e \left(1 - \frac{n_t(t)}{N_{te}}\right) n(t) - \frac{n_t(t)}{\tau_{re}}, \tag{4.15}$$

where C_t is the deep trapping capture coefficient, N_t is the concentration of the deep trap centers in the blocking layers, τ_r is the release time constant for the deeply trapped carriers, $\theta = \mu/\mu_0$, and μ_0 is the mobility in the extended states of a-Se layers. Note that in the presence of shallow traps, the effective capture coefficient becomes $C_t\theta$ [80]. The release time, τ_r is related to the trap depth E_t by $v_0^{-1}\exp(E_t/kT)$, where v_0 is the phonon frequency. The relation between v_0 and C_t can be determined by the principle of detailed balance, which gives $v_0 = N_V C_{th}$ for trapped holes [81, 82].

The coupled algebraic-differential equations (4.2) – (4.15) are simultaneously solved using MATLAB to get the instantaneous electric field profile, trapped carriers, and dark current due to carrier injection from the metal electrodes. Note that there will be a separate trapping rate equation for each discrete deep trap level, and the total trapped carrier will be the sum of the trapped carriers in all trap levels.

The steady-state thermal generation current in a-Se arises from the carriers excited from the deep states near Fermi level to the band edges of the intrinsic layer. The blocking layers are much thinner compared to the intrinsic layer, and there is negligible trapped charge in the intrinsic layer. Therefore the electric field is constant throughout the i-layer and nearly close to the applied field (F_0). Considering uniform thermal emission of trapped carriers throughout the i-layer, the continuity equation for holes and electrons can be written as [83],

$$\frac{\partial p(x,t)}{\partial t}+\mu_h F_0\frac{\partial p(x,t)}{\partial x}=-\frac{1}{\tau_h}p(x,t)+g_h\,, \tag{4.16}$$

$$\frac{\partial n(x,t)}{\partial t}-\mu_e F_0\frac{\partial n(x,t)}{\partial x}=-\frac{1}{\tau_e}n(x,t)+g_e\,, \tag{4.17}$$

where τ the effective charge carrier lifetime, $p(n)$ is the the concentration of holes (electrons), and g is the carrier generation rate. The lifetime, τ is related to trap center concentration in the intrinsic layer, N_{ti} by $(\theta C_t N_{ti})^{-1}$. The lifetime in a-Se is easily measured by interrupted field time-of-flight (IFTOF) experiments [84].

In a-Se the trap levels are likely to be charged defect (positive or negative) and thus field enhanced thermal generation occurs [46]. The thermal generation rate is dominated by the emission from traps within kT of the Fermi level. The generation rate for holes and electrons can be expressed as [85],

$$g_h=N\left(E_F\right)kTv_0\exp\left[-\left(E_F-E_V-\beta_{pf}\sqrt{F_0}\right)/kT\right] \tag{4.18}$$

$$g_e=N\left(E_F\right)kTv_0\exp\left[-\left(E_C-E_F-\beta_{pf}\sqrt{F_0}\right)/kT\right] \tag{4.19}$$

where $N(E_F)$ is the density of states of a-Se at energy E_F near the mid-gap, $E_{V(C)}$ is the energy of valence (conduction) band edge, and β_{pf} = $\surd(e^3/\pi\varepsilon_{se})$ is the Poole-Frenkel coefficient. In (4.18) and (4.19), it is assumed that $N(E_F)$ is constant over kT near E_F. At steady-state, the solution of (4.16) is expressed as,

$$p(x) = g_h \tau_h \left[1 - \exp\left(-\frac{x}{\mu_h \tau_h F_0} \right) \right]. \tag{4.20}$$

The hole current density is given by

$$J_{sh} = \frac{e\mu_h F_0}{L} \int_0^L p(x)dx. \tag{4.21}$$

Therefore, the steady-state thermal generation current density due to holes can be expressed as,

$$J_{sh} = e\mu_h \tau_h F_0 g_h \left[1 - \frac{\mu_h \tau_h F_0}{L} \left\{ 1 - \exp\left(-\frac{L}{\mu_h \tau_h F_0} \right) \right\} \right]. \tag{4.22}$$

Similarly, the steady-state thermal generation current density due to electrons can be expressed as,

$$J_{se} = e\mu_e \tau_e F_0 g_e \left[1 - \frac{\mu_e \tau_e F_0}{L} \left\{ 1 - \exp\left(-\frac{L}{\mu_e \tau_e F_0} \right) \right\} \right]. \tag{4.23}$$

It is evident from (4.22) and (4.23) that, the thermal generation current depends on the applied field due to trapping of the generated carriers. After adding the transient and the steady-state current, the time and voltage dependent total dark current in a-Se based n-i-p detector is,

$$J_d(t) = J_{inj}(t) + J_{sh} + J_{se}. \tag{4.24}$$

The dark current model for p-i-n detector is exactly the same as for n-i-p detector. The only difference is that, the hole current equation will be the electron current equation and vice versa. The developed dark current model can be applied to metal/a-Se/metal structure, if a significantly thick interface layer exists between the metal and the a-Se. In this case, the interface layers serve the purpose of n/p layers that are able to trap charge carriers.

4.2.2 Dark Current Model for n-i Structure

In a-Se the electron range, $\mu_e\tau_e$ is almost an order of magnitude lower than the hole range, $\mu_h\tau_h$. Thus, it is believed that the dark current in metal/a-Se/metal structures is mainly dominated by the injection of holes from the positive electrode rather than the injection of electrons from the negative electrode [24]. In multilayer structure the n-layer can be the most important blocking layer, as it is a hole trapping layer. Recently, Kasap and coworkers [11, 13, 19, 21] have reported that a low dark current level can be achieved in n-i structures in which the n-layer is produced by cold deposition technique. The cold deposited n-layer has the same hole-trapping effect. The deposition technique is simpler for implementation as it avoids the necessity to produce the doped materials [13]. Although the dark current in n-i structures is higher than that in n-i-p/p-i-n structures, it is acceptable for diagnostic X-ray imaging applications [11].

It is instructive to modify the developed dark current model for n-i structure. Note that, due to the absence of p-layer the electric field profile will be different compared to n-i-p structure. The steady-state electric field profile before applying any radiation in the a-Se based n-i structure is shown in Fig. 4.3. The electric field at the metal/n-layer interface decreases due to trapping of holes in the n-layer. However, the electric field at the metal/i-layer interface increases since the total electric field remains equal to the initial applied electric field.

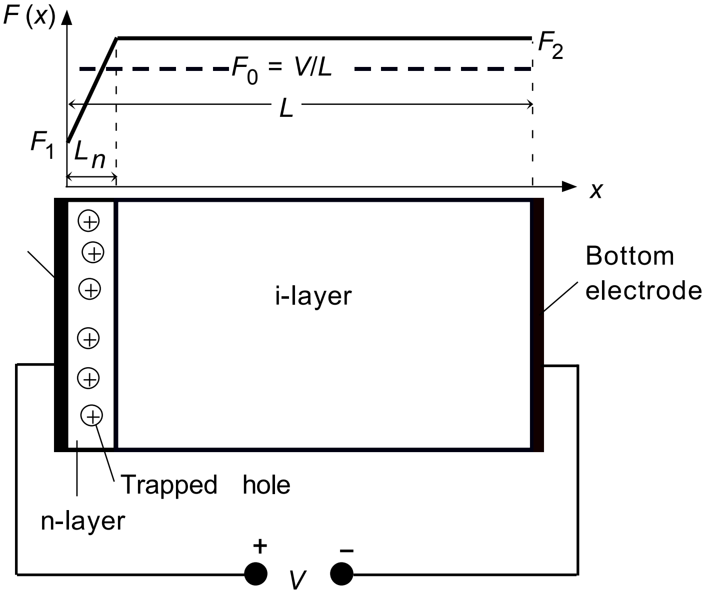

Figure 4.3 A multilayer n-i a-Se structure showing time-dependent electric field profile. The dash line represents the initial uniform electric field and the solid line represents the field distribution sometime after the application of field. L_n is the thickness of the n-layer and L is the total photoconductor thickness.

The instantaneous electric field $F_1(t)$ and $F_2(t)$ for n-i structure are determined by solving the Poisson's equation in a-Se layers, and are given by,

$$F_1(t) = F_0 - \frac{q}{\varepsilon_{se}}\left(L_n - \frac{L_n^2}{2L}\right)p_t(t), \tag{4.25}$$

$$F_2(t) = F_0 + \frac{q}{\varepsilon_{se}}\frac{L_n^2}{2L}p_t(t). \tag{4.26}$$

From (4.3) and (4.26) it is evident that, the electron current increases due to trapping of holes in the n-layer. The trapped carrier concentrations are calculated using (4.14) and (4.15) as described in section 4.1.1. Finally, the total dark current density in a-Se based n-i detectors is calculated using (4.24).

4.2.3 Dark Current Model for metal/a-Se/metal Structure

Although it is believed that the hole injection mainly controls the dark current in a-Se based detectors, the electron injection can also have a significant effect, if the barrier for the electron injection is small. The barrier for the electron injection depends on the work function of the metal contact. Belev *et al.* have compared the dark current in the metal/a-Se/metal structure by using aluminum (Al), gold (Au) and platinum (Pt) as the negatively biased top contact [19]. The a-Se used in this study is produced by cold deposition technique and thus, it works as a hole trapping layer (i.e., n-layer). They have found that, the dark current depends on the work function of the metal electrode. The authors have compared the dark current between the metal/a-Se (i-type)/metal and the metal/a-Se (n-type)/metal structures. Note that the intrinsic a-Se is slightly p-type and thus, it traps electrons.

It is required to modify the developed dark current model for metal/a-Se/metal structures. The steady-state electric field profile before applying any radiation in the metal/a-Se (n-type)/metal structure is shown in Fig. 4.4. It has been assumed that the trapping of holes is uniform throughout the n-type a-Se layer. The instantaneous electric field $F_1(t)$ and $F_2(t)$ are given by,

$$F_1(t) = F_0 - \frac{qL}{2\varepsilon_{se}} p_t(t)\,, \tag{4.27}$$

$$F_2(t) = F_0 + \frac{qL}{2\varepsilon_{se}} p_t(t)\,. \tag{4.28}$$

From (4.27) and (4.28) it is evident that the electric field at the negative electrode increases, whereas it decreases at the positive electrode with increasing p_t. Thus, carrier trapping in the metal/a-Se (n-type)/metal structure enhances the electron injection, and reduces the hole injection. The total dark current density in metal/a-Se (n-type)/metal detectors is calculated using (4.24) as described in section 4.1.1.

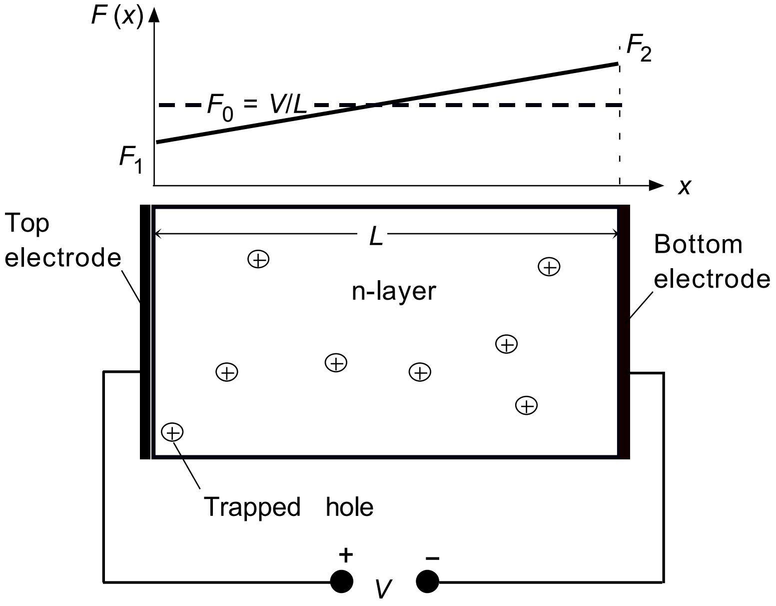

Figure 4.4 A metal/a-Se (n-type)/metal structure showing time-dependent electric field profile. The dash line represents the initial uniform electric field and the solid line represents the field distribution sometime after the application of field.

Figure 4.5 shows the steady-state electric field profile before applying any radiation in the metal/a-Se (i-type)/metal structure. Assuming uniform trapping of electrons throughout the i-type a-Se layer, the instantaneous electric field $F_1(t)$ and $F_2(t)$ can be written as,

$$F_1(t) = F_0 + \frac{qL}{2\varepsilon_{se}} n_t(t), \tag{4.29}$$

$$F_2(t) = F_0 - \frac{qL}{2\varepsilon_{se}} n_t(t). \tag{4.30}$$

From (4.29) and (4.30) it is evident that, the electric field at the positive electrode increases whereas it decreases at the negative electrode due to the trapping of electrons. Thus, carrier trapping in the metal/a-Se (i-type)/metal structure enhances the hole injection, and reduces the electron injection. The total dark current density in metal/a-Se (i-type)/metal detectors is calculated using (4.24) as described in section 4.1.1.

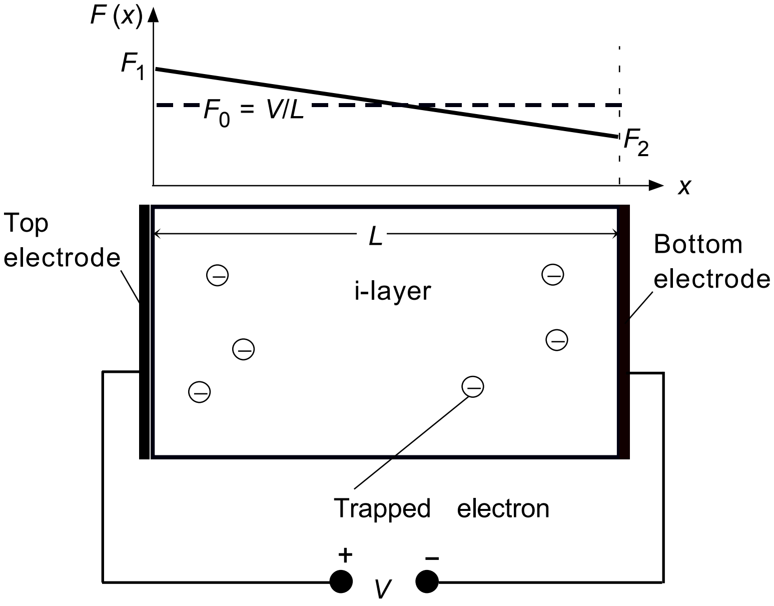

Figure 4.5 A metal/a-Se (i-type)/metal structure showing time-dependent electric field profile. The dash line represents the initial uniform electric field and the solid line represents the field distribution sometime after the application of field.

4.2.4 Experimental Details

The dark current measurement is performed on several n-i-p and p-i-n samples. The a-Se was deposited onto indium tin oxide (ITO) substrate, and coated with metallic electrodes (e.g., Al). For the dark current measurements, a bias voltage is applied on test samples using one automated Bertan 205B power supply, and the resulting current is converted into voltage and digitized using a current Keitley amplifier model 428 and one Tektronic digital oscilloscope TDS784D. Prior to applying the bias voltage a reference level was acquired, and subtracted from the subsequent current signals under bias. One acquisition every 2 seconds was found to give a satisfactory temporal resolution. Knowing the amplifier conversion factor and the surface area of the metal electrode, all the results are presented in pA/cm^2.

4.2.5 Results and Discussion

The developed dark current model is verified with the measured and the published experimental data. As mentioned in chapter 3 for a-Se, the band mobilities of electrons and holes are, μ_{0e} = 0.1 cm^2/V-s and μ_{0h} = 0.3 cm^2/V-s whereas their effective mobilities are, μ_e = 0.003 cm^2/V-s and μ_h = 0.12 cm^2/V-s [16, 49, 86]. The parameters, $v_0 = 10^{12}$ /s, $\varepsilon_r = 6.7$, $\tau_e = 7.3\times10^{-4}$ s, $\tau_h = 7.1\times10^{-5}$ s, $E_C - E_F = 1.155$ eV, and $E_F - E_V = 1.065$ eV are taken in the calculations [46, 49]. The effective density of states is assumed to be $N_C = N_V = 10^{19}$ /cm^3 in all layers and the density of states near mid-gap in the i-layer is, $N(E_F) = 10^{14}$ /cm^3/eV [46, 87].

Unless otherwise specified all the parameters mentioned above are fixed for all the theoretical calculations shown in this section. Other parameters such as effective barrier height (φ), trap center concentration (N_t), and trap depth in the blocking layer depend on the fabrication processes and therefore, these are considered as variable parameters in the model. Assuming $A^* = 120$ A/cm^2/K^2 and $T = 295$ K, the thermal velocity, v_R is ~6.5×10^6

cm/s. At a very high field of 100 V/μm, v_{dh} is ~3 × 10^5 cm/s. Therefore, even at a very high field, v_{dh} in a-Se is approximately one order of magnitude smaller than the thermal velocity. Since $v_R >> v_{dh}$, the hole injection current is dominated by v_{dh} (Eq. 4.2).

I. Dark current in n-i-p structure

The dark current density as a function of time for three different applied biases for the n-i-p structure is shown in Fig. 4.6. The symbols represent experimental data and the solid lines represent the theoretical validation to the experimental data. The proposed model has a good agreement with the experimental results. The sample 531-1 has a total photoconductor thickness of 1000 μm. The thicknesses of n and p layers are 20 μm and 5 μm, respectively. We consider two discrete deep trapping states for trapped carriers in the blocking layers to validate the experimental data. For holes, the depths of these two trapping states are 0.76 eV (τ_{rh1} = 5.7 s) and 0.81 eV (τ_{rh2} = 33 s) from the mobility edge of the valence band. For electrons, the depths of the two trapping states are 1.29 eV (τ_{re1} = 1 h) and 1.27 eV (τ_{re2} = 2 h) from the mobility edge of the conduction band. These results are equivalent to a broadened state of widths ~0.02−0.05 eV. The validated parameters are N_{t1} = 8 × 10^{15} /cm^3, N_{t2} = 2 × 10^{15} /cm^3, for both holes and electrons. The values of effective barriers are, φ_h = 0.9 eV, and φ_e = 0.98 eV. All the parameters mentioned above are constant for all the applied fields. It has been found that the thermal generation current is ~0.5 pA/cm^2, whereas the carrier injection current is ~19 pA/cm^2 at steady-state for 10 V/μm applied electric field. Therefore, the thermal generation current in n-i-p sample is negligible. Form Fig. 4.6 it is evident that, the model and the measured data differ particularly in the time period right after applying the bias. The deviation is possibly due to the change in interface states, which causes the change in effective barrier for injecting carrier with the time as well as with the applied electric field [88, 89, 90]. This effect has not been included in the model.

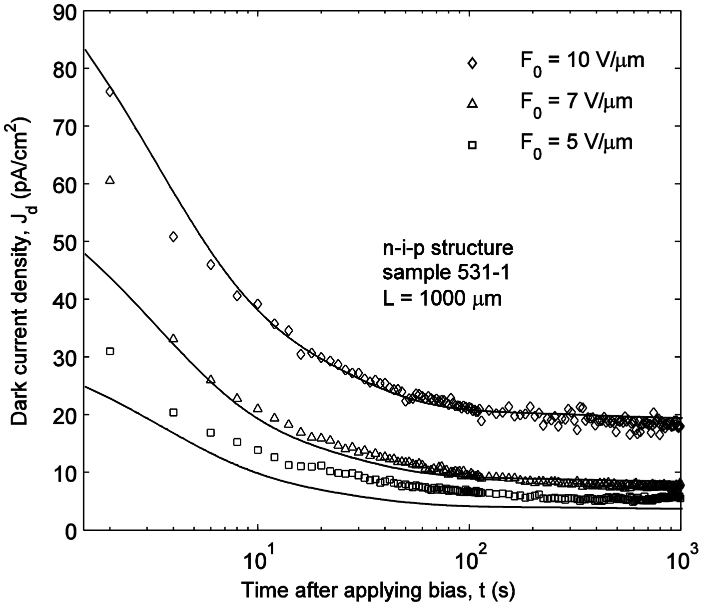

Figure 4.6 Dark current density of an a-Se n-i-p sample as a function of time for three different positive applied biases. The symbols represent experimental data and the solid lines represent the theoretical validation to the experimental data [20].

It is instructive to compare the magnitudes of electron and hole current density in n-i-p detector structure. Figure 4.7 shows the theoretical hole and electron injection current densities as a function of time at 10 V/μm for the sample mentioned in Fig. 4.6. The total dark current density is also shown for comparison. It is evident from Fig. 4.7 that, the electron injection current is almost twenty times smaller than the hole injection current because of high effective barrier for the injecting electron. For the same effective barrier height and electric field, the dark current due to electron injection is much smaller than that due to hole injection [as evident from (4.2) and (4.3)] because of very low electron mobility in a-Se. Therefore, the dark current in n-i-p a-Se detectors is mainly controlled by hole injection, which has also been experimentally observed by Kasap and Belev [13].

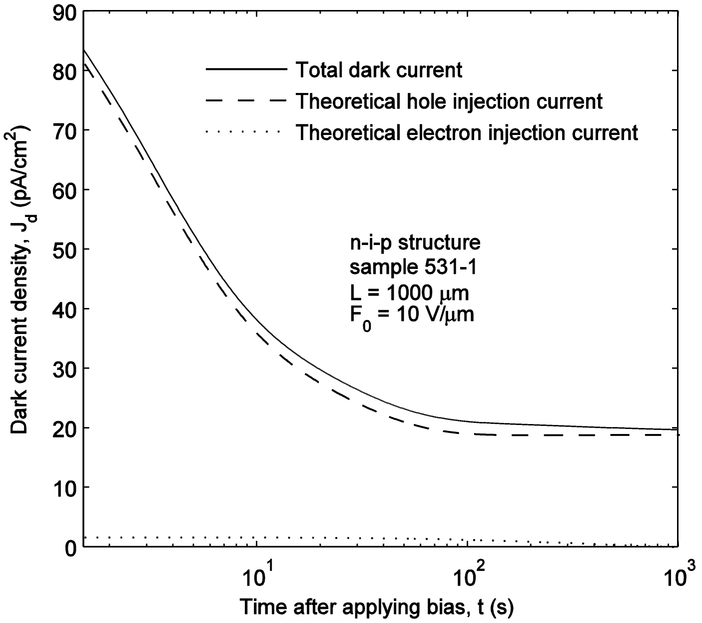

Figure 4.7 The hole and electron injection current density as a function of time at 10 V/μm for the a-Se n-i-p sample mentioned in figure 4.6. Both the hole and electron injection currents decrease with time.

Figure 4.8 shows the trapped carrier concentrations as a function of time at 10 V/μm for the sample mentioned in Fig. 4.6. It is evident from Fig. 4.8 that, the trapped carrier concentrations increase with time, and reach a saturation level when the trapping and the release rates reach equilibrium. The concentrations of deep trap center in the n and p layers are found to be ~10^{15} – 10^{16} /cm^3 (Note that the concentration of deep trap centers in the i-layer is in the range of 10^{12} – 10^{13} /cm^3) [46]. The saturation value of trapped holes and electrons concentrations are ~1.2×10^{14} /cm^3 and ~7.5×10^{14} /cm^3. It has been found that the saturation value of trapped carriers increases with increasing applied electric field. It is evident that, the trap centers are not fully filled with trapped carriers.

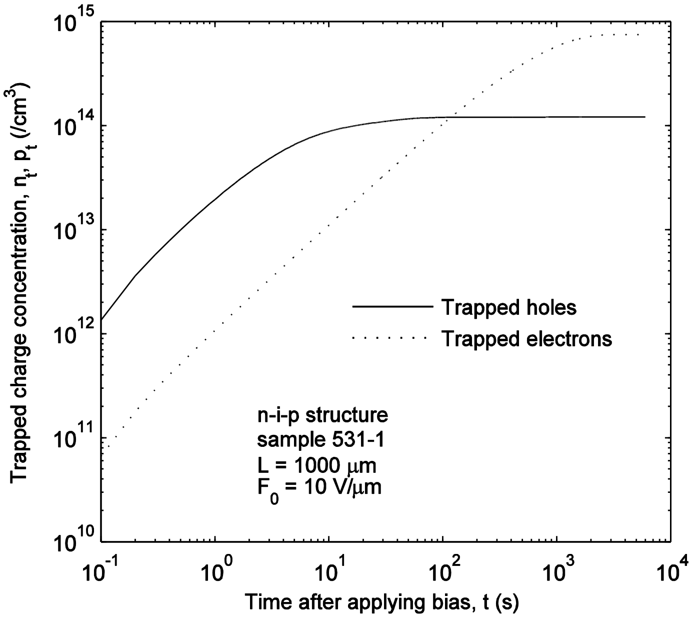

Figure 4.8 Trapped holes and electrons concentrations as a function of time at 10 V/μm applied electric field. The trapped carrier concentrations reach saturation level some time after the application of electric field.

Figure 4.9 show the electric field profile across the n and p layers (left and right figures, respectively) as a function of time at 10 V/μm for the sample mentioned in Fig. 4.6. The initial field is shown for a reference as well. The high initial dark current shown in Fig. 4.6 is due to high initial electric field at the metal/a-Se interfaces. However, the dark current decreases with time and reaches a steady value within the time scale of ~100−1000 seconds. The trapped carrier concentrations in the blocking layers increase with time and the transient electric field at the interfaces decrease significantly which eventually reduce the dark current. It is evident from Fig. 4.9 that the electric field at the metal contact reduces to 30−40% of initial applied electric field. When the carrier trapping rate becomes equal to the release rate, the trapped carrier concentrations in the blocking layers reach a steady-state. The time required to reach this condition depends on the release time constant.

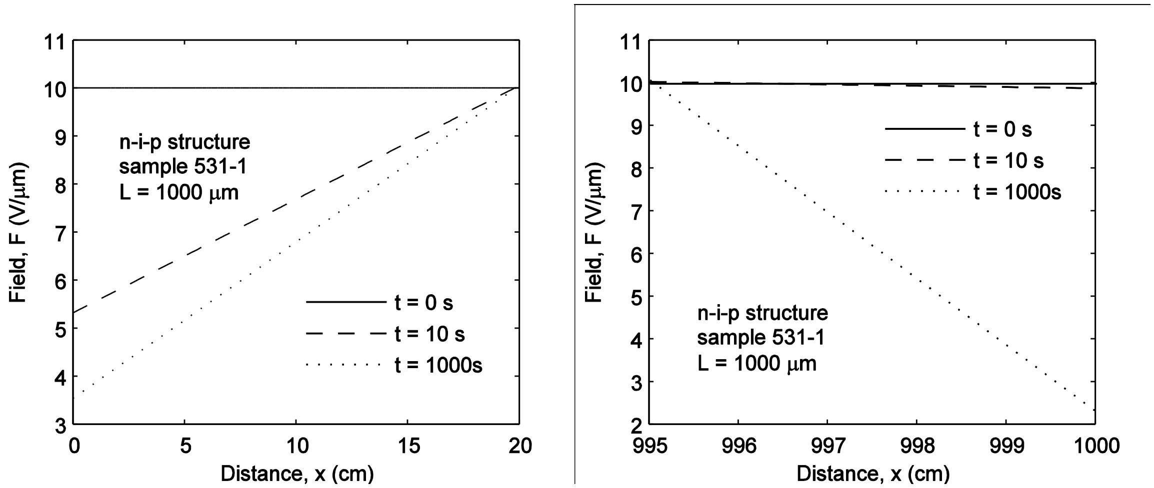

Figure 4.9 The electric field profile across the n-layer (left figure) and the p-layer (right figure) as a function of time at 10 V/μm for the sample mentioned in Fig. 4.6.

The transient dark current depends on many factors such as effective barrier heights, concentrations of trap centers in the blocking layers, and characteristics carrier release times. Note that the parameters of the n-layer are more important than the p-layer, as the dark current in n-i-p structures mainly dominated by the hole injection. Figure 4.10 shows the transient dark current behavior for various levels of trap centers in the *n*-layer and a fixed effective barrier height of ϕ_h ~0.89 eV. The release time constants for deeply trapped holes are same as in Fig. 4.6. The trap center concentrations, effective barrier height, and depths of the trapping states for electrons are also fixed. It is found that, the steady-state dark current decreases with increasing trap centers in the n-layer provided that the effective barrier height remains the same.

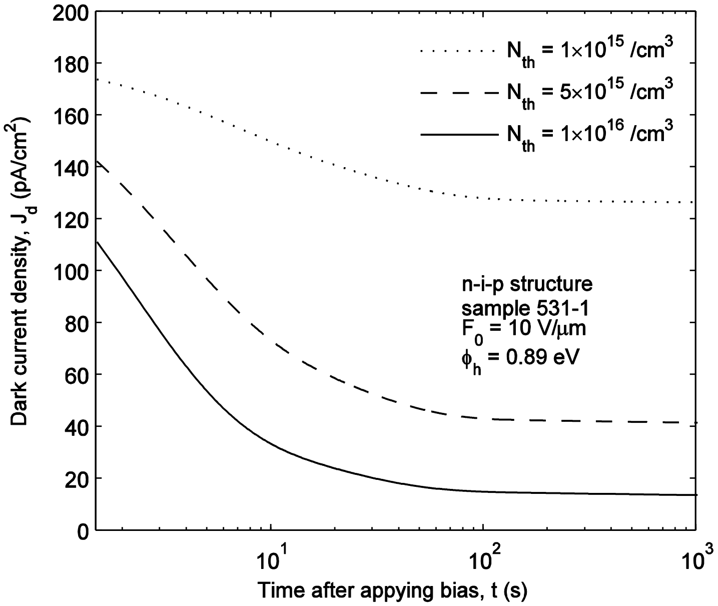

Figure 4.10 Transient dark current behavior of the a-Se n-i-p sample mentioned in figure 4.6 for various levels of trap centers and a fixed effective barrier height of φ_h ~0.89 eV [20].

Figure 4.11 shows the transient dark current behavior for various effective barrier heights for hole injection keeping the same total deep hole trap center concentration of 10^{16} cm^{-3}. The other parameters are same as in Fig. 4.6. The initial dark current increases exponentially with decreasing the barrier height. It is evident from Figs. 4.10 and 4.11 that, the initial dark current mainly depends on the equilibrium barrier heights, and the steady state dark current depends on the trap center concentration in the blocking layers. Increasing trap centers in the blocking layers may apparently be beneficial for lowering the dark current. However, we need to increase the doping for increasing trap centers, which may change the effective barrier height and the depth of the trap centers.

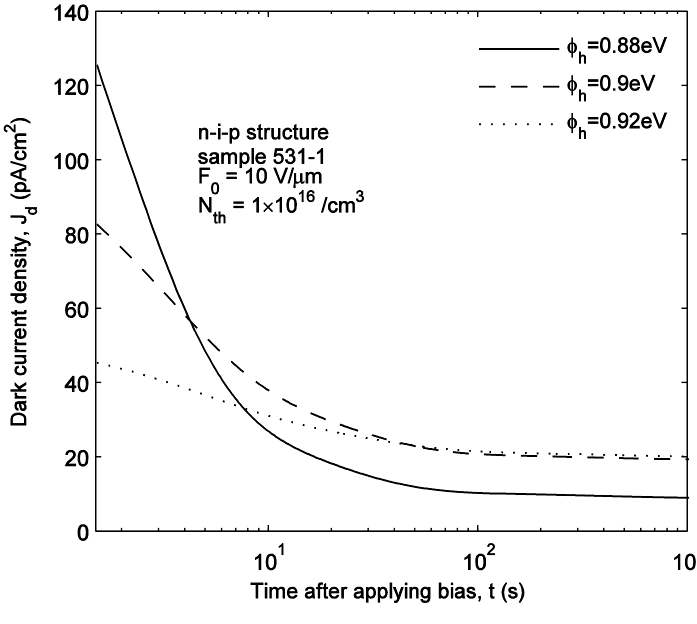

Figure 4.11 Transient dark current behavior of the a-Se n-i-p sample mentioned in figure 4.6 for various effective barrier heights and a fixed total deep hole trap center concentration of 10^{16} cm^{-3} [20].

It is necessary to investigate the dark current behavior for a different n-i-p sample. The dark current density as a function of time for the n-i-p structure for two different applied electric fields is shown in Fig. 4.12. The symbols represent experimental data and the solid lines represent the theoretical validation to the experimental data [91]. The proposed model has a good agreement with the experimental data. The sample 531-5 has a total photoconductor thickness of 1000 μm. The thicknesses of *n* and *p* layers are 20 μm and 5 μm, respectively. Two discrete deep trapping states have been considered for trapped carriers in the blocking layers to validate the experimental data. For holes, the depths of these two trapping states are 0.76 eV (τ_{rh1} = 5 s) and 0.8 eV (τ_{rh2} = 27 s) from the mobility edge of the valence band. For electrons, the depths of the two trapping states are 1.29 eV (τ_{re1} = 1 h) and 1.27 eV (τ_{re2} = 2 h) from the mobility edge of the conduction band. These results are equivalent to a broadened state of widths ~0.02−0.04 eV. The validated parameters are $N_{t1} = 4 \times 10^{15}$ /cm^3, $N_{t2} = 10^{15}$ /cm^3, for both holes and electrons. The values of effective barriers are, φ_h = 0.89 eV, and φ_e = 0.98 eV. All the parameters mentioned above are constant for both the applied electric fields. Comparing Figs. 4.6 and 4.12, it is evident that the transient behavior of dark current is similar in both n-i-p samples. In case of both samples the dark current reaches a plateau within 100 s. However, the initial and the steady-state dark current are higher in this sample. The possible reasons of higher dark current are due to the dependence of the blocking layers trap densities, and the effective barrier height for injecting holes on the fabrication process. Note that, the validated trap densities in the blocking layers and the effective barrier for hole injection are smaller in this sample.

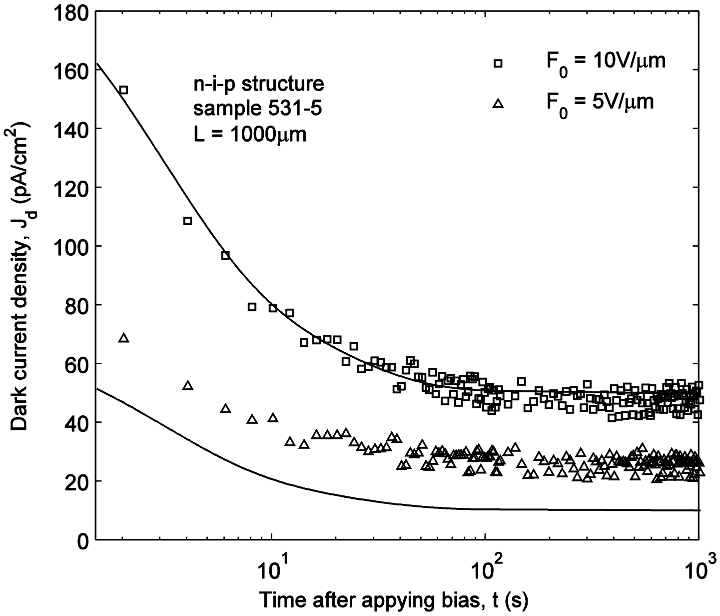

Figure 4.12 Dark current density of an a-Se n-i-p sample as a function of time for two different positive applied biases. The symbols represent experimental data and the solid lines represent the theoretical validation to the experimental data [91].

It is instructive to compare the steady-state dark current density in n-i-p structure at different applied electric fields. Figure 4.13 shows the steady-state dark current density as a function of applied electric field for a-Se based n-i-p detector structure. The squares represent experimental data and the stars with solid line represent the theoretical validation to the experimental data. The experimental data has been extracted from Fig. 6 of [11]. The dashed line represents the electron injection current, and the dotted line represents the bulk thermal generation current. The proposed model shows a very good match with the experimental data. The total photoconductor thickness is 200 μm. The thicknesses of n and p layers are 6 μm and 5 μm, respectively. The dark current reaches a plateau within 1000 s after the application of field as shown in Fig. 4.6. Therefore the trapping rate equations have been solved up to 1000 s to get the steady-state dark current. For all the applied electric fields, two discrete deep trapping states for trapped carriers in the blocking layers have been considered to validate the experimental data. For holes, the depths of these two trapping states are 0.78 eV (τ_{rh1} = 12 s) and 0.81 eV (τ_{rh2} = 42 s) from the mobility edge of the valence band. For electrons, the depths of the two trapping states are 1.29 eV (τ_{re1} = 1 h) and 1.27 eV (τ_{re2} = 2 h) from the mobility edge of the conduction band. These results are equivalent to a broadened state of widths ~0.02−0.03 eV. For all the applied electric fields, the validated parameters are $N_{t1} = 8 \times 10^{15}$ /cm^3, $N_{t2} = 4 \times 10^{15}$ /cm^3, for both holes and electrons. The validated effective barrier for injecting holes varies from 0.89 eV to 0.86 eV with varying the applied field from 3 V/μm to 10 V/μm. The effective barrier for injecting electrons is 1 eV for all the applied electric fields. The saturated values of trapped holes are 1.84×10^{14}, 3.11×10^{14}, 4.38×10^{14}, 6.28×10^{14} /cm^3 for the applied electric fields of 3, 5, 7 and 10 V/μm, respectively. The saturated value of trapped charges increases with increasing applied electric field. From Fig. 4.13, it is evident that at steady-state, the thermal generation current is ~0.1 pA/cm^2 at 10 V/μm applied field which is about one order of magnitude smaller than the injection current because of large energy band gap in a-Se. The thermal generation current increases almost exponentially with increasing the applied electric field. At 10 V/μm applied electric field, the dark current in this sample is much lower (~ 1 pA/cm^2) compared to the other samples discussed before.

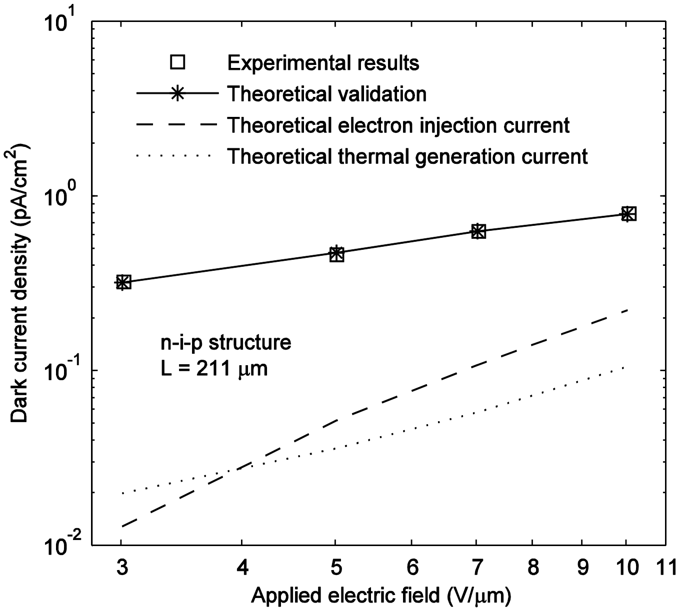

Figure 4.13 Steady-state dark current density in n-i-p structure versus applied electric field. The squares represent the experimental data and the stars with solid line represent the theoretical validation to the experimental data.

In conclusion, it has been found that the dark current in a-Se based n-i-p detector structures mainly dominated by the injection of holes from the positive electrode. The electron injection current is relatively lower in this structure. The thermal generation current is negligible due to the large energy band gap in a-Se.

II. Dark current in p-i-n structure

As mentioned before the radiation receiving electrode in p-i-n structure is connected to the p-layer and the charge collection electrode is connected to the n-layer. To reverse bias the structure, the top electrode (radiation receiving electrode) is negatively biased with respect to the bottom electrode (charge collection electrode). Thus, the X-ray generated holes will move towards the top electrode and the electrons will move towards the bottom electrode. The dark current model is exactly the same as for n-i-p detector. The only difference is that, the hole current equation will be the electron current equation and vice versa.

The dark current density as a function of time for three different applied biases for a p-i-n structure is shown in Fig. 4.14. The symbols represent experimental data and the solid lines represent the theoretical validation to the experimental data. The proposed model has a good agreement with the experimental results. The sample 553-5 has a total photoconductor thickness of 1000 μm. The thicknesses of the n- and p-layer are 20 μm and 5 μm, respectively. We consider two discrete deep trapping states for trapped carriers (both holes and electrons) in the blocking layers to validate the experimental data. For holes, the depths of these two trapping states are 0.75 eV (τ_{rh1} = 4.5 s) and 0.8 eV (τ_{rh2} = 30 s) from the mobility edge of the valence band. For electrons, the depths of the two trapping states are 1.29 eV (τ_{re1} = 1 h) and 1.27 eV (τ_{re2} = 2 h) from the mobility edge of the conduction band. These results are equivalent to a broadened state of widths ~0.02−0.05 eV. The validated parameters are $N_{t1} = 7 \times 10^{14}$ /cm^3, $N_{t2} = 1.5 \times 10^{14}$ /cm^3, for both holes and electrons. The values of effective barriers are, φ_h = 0.85 eV, and φ_e = 0.98 eV. All the parameters mentioned above are constant for all the applied fields.

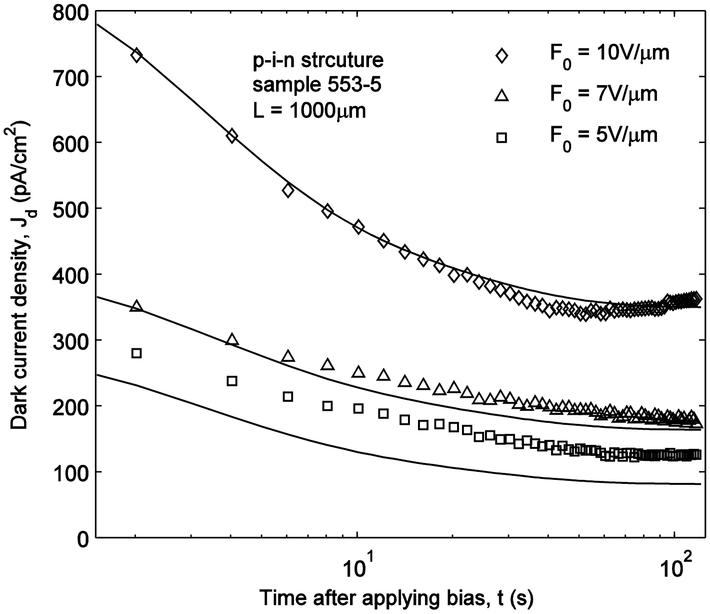

Figure 4.14 Dark current density of an a-Se p-i-n sample as a function of time for three different positive applied biases. The symbols represent experimental data and the solid lines represent the theoretical validation to the experimental data.

From Fig. 4.14 it is evident that, the dark current in p-i-n structure decays with time up to around 100 s. However, there is a trend of increasing dark current after 50 s at 10 V/μm. Therefore, it is necessary to measure the dark current in p-i-n structure for a longer period, and compare with the dark current behavior in n-i-p structure. The dark current density as a function of time at 10 V/μm for another p-i-n sample is shown in Fig. 4.15. The symbols represent experimental data and the solid lines represent the theoretical validation to the experimental data. The sample 445-2 has the same thicknesses of different layers as in the previous p-i-n sample. We consider two discrete deep trapping states for trapped carriers (both holes and electrons) in the blocking layers to validate the experimental data. For holes, the depths of these two trapping states are 0.75 eV (τ_{rh1} =

4.5 s) and 0.82 eV (τ_{rh2} = 54 s) from the mobility edge of the valence band. For electrons, the depths of the two trapping states are the same as in the previous analysis. These results are equivalent to a broadened state of widths ~0.02−0.07 eV. The validated parameters are, $N_{t1} = 10^{15}$ /cm^3, $N_{t2} = 2 \times 10^{14}$ /cm^3, for both holes and electrons. The values of effective barriers are, φ_h = 0.86 eV, and φ_e = 0.98 eV. From Fig. 4.15 it is evident that, the dark current in p-i-n samples does not stabilize as like n-i-p samples. In this sample the current starts increasing after ~100 s, and the increasing trend sustains up to 1000 s. Afterwards, the current starts decreasing over time, and eventually crosses the first minima. In this sample, the current does not increase significantly after reaching the first minima.

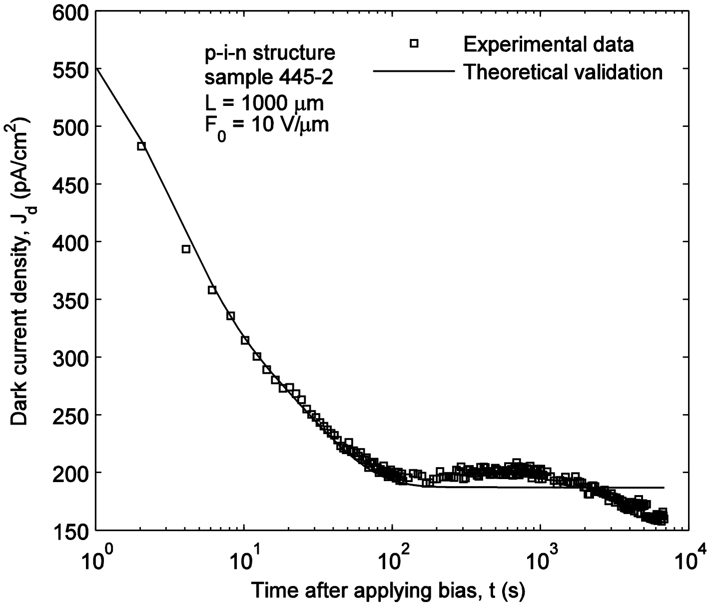

Figure 4.15 Dark current density of a p-i-n sample (445-2) as a function of time at 10 V/μm. The symbols represent experimental data and the solid line represents the theoretical validation to the experimental data.

Figure 4.16 shows the dark current density as a function of time at 10 V/μm for another p-i-n sample. The symbols represent experimental data and the solid lines represent the theoretical validation to the experimental data. The sample 441-4 has the same thicknesses of different layers as in the previous sample. We consider two discrete deep trapping states for trapped carriers (both holes and electrons) in the blocking layers to validate the experimental data. For holes, the depths of these two trapping states are 0.74 eV ($\tau_{rh1} = 3$ s) and 0.79 eV ($\tau_{rh2} = 20$ s) from the mobility edge of the valence band. For electrons, the depths of the two trapping states are the same as in the previous analysis. These results are equivalent to a broadened state of widths ~0.02−0.05 eV. The validated parameters are $N_{t1} = 2 \times 10^{15}$ /cm^3, $N_{t2} = 4.5 \times 10^{14}$ /cm^3, for both holes and electrons. The values of effective barriers are, $\varphi_h = 0.87$ eV, and $\varphi_e = 0.98$ eV.

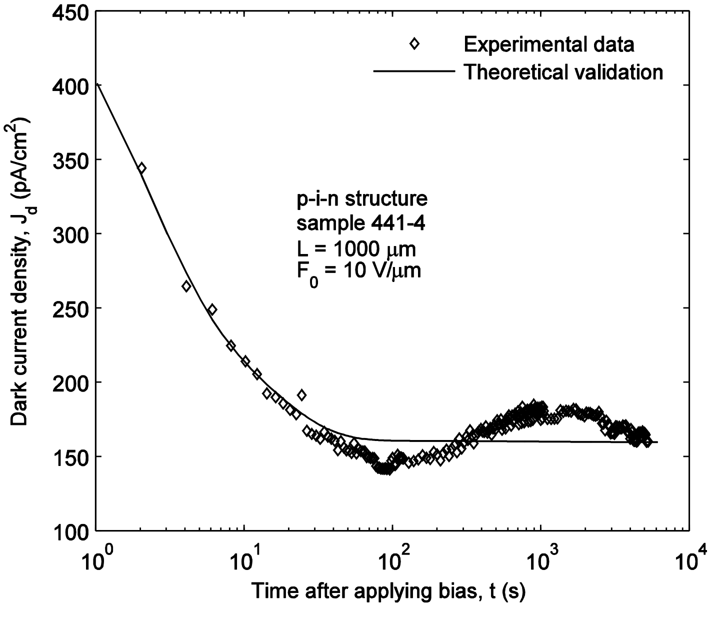

Figure 4.16 Dark current density of a p-i-n sample (441-4) as a function of time at 10 V/μm. The symbols represent experimental data and the solid line represents the theoretical validation to the experimental data.

From Fig. 4.16 it is evident that, the dark current shows a distinct minima and maxima after the initial decay. We tried another sample to measure the dark current density in p-i-n structure. Figure 4.17 shows the dark current density as a function of time at 10 V/μm. The symbols represent experimental data and the solid lines represent the theoretical validation to the experimental data. The sample 442-5 has the same thicknesses of different layers as in the previous sample. We consider two discrete deep trapping states for trapped carriers (both holes and electrons) in the blocking layers to validate the experimental data. For holes, the depths of these two trapping states are 0.74 eV (τ_{rh1} = 3 s) and 0.79 eV (τ_{rh2} = 20 s) from the mobility edge of the valence band. For electrons, the depths of the two trapping states are 1.29 eV (τ_{re1} = 1 h) and 1.27 eV (τ_{re2} = 2 h) from the mobility edge of the conduction band. These results are equivalent to a broadened state of widths ~0.02−0.05 eV. The validated parameters are $N_{t1} = 1.5 \times 10^{15}$ /cm^3, $N_{t2} = 4.5 \times 10^{14}$ /cm^3, for both holes and electrons. The validated effective barriers are, $\varphi_h = 0.87$ eV, and $\varphi_e = 0.98$ eV.

Comparing Figs. 4.16 and 4.17, it is evident that the samples 441-4 and 442-5 show almost similar dark current behavior of maxima and minima. However, in case of 442-5 the dark current shows a decreasing trend towards the minima (after the reaching the maxima), and eventually crosses the first minima. Similar behavior is found for the sample 445-2.

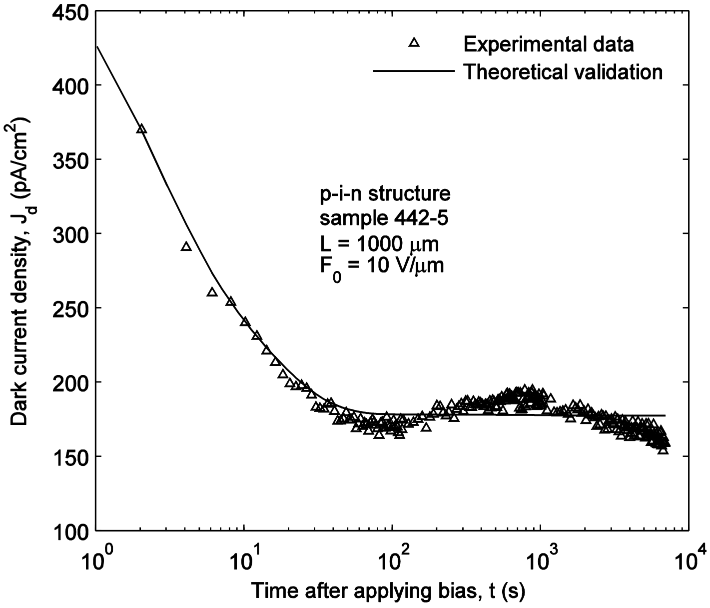

Figure 4.17 Dark current density of a p-i-n sample (442-5) as a function of time at 10 V/μm. The symbols represent experimental data and the solid line represents the theoretical validation to the experimental data.

Finally, it can be concluded that the dark current in p-i-n structure is higher than the n-i-p structure. In p-i-n structures holes are injected from the bottom electrode, which is indium tin oxide (ITO). The hole injection efficiency of ITO is higher compared to metallic electrodes (e.g., Al) [92]. As the dark current in a-Se detectors is mainly dominated by hole injection, higher dark current is expected in p-i-n structures. It has been found that the dark current behaviour in p-i-n structures shows distinct minima and maxima after the initial decay. The increase in current after reaching the minima may be due to the release of trapped holes over time from the bulk of the n-layer [21]. The oscillation is also present in n-i-p sample. However, the maxima and the minima are not distinct due to low magnitude of dark current in n-i-p samples. The possible reason for the oscillation is the reduction of hole barrier due to the trapping of electrons at the a-Se/metal interface states. Reduction of electron barrier due to hole trapping at the interface for a-Si based imagers has been reported [93]. All the dark current data for p-i-n structures shows the maxima around 1000 s. Considering a typical phonon frequency of 10^{12} /s, the location of the interface states is about 0.86 eV above the valence band edge.

III. Dark current in n-i structure

As mentioned before, the parameters of n-layer mainly controls dark current in multilayer a-Se detectors. Thus, it is instructive to study the dark current behavior in n-i structures. In this structure, the n-layer is deposited at a low substrate temperature, which is below the glass transition temperature of the material. The cold deposited n-layer has reduced hole transport with respect to i-layer, but has better electron transport than the doped n-layer [11]. Therefore, the structure can be made from a single composition of a-Se using vacuum deposition technique [13].

The developed dark current model has been verified with the published experimental data. Figure 4.18 shows the dark current density as a function of time for the n-i structure. The symbols represent the experimental data and the solid line represents the theoretical validation to the experimental data. The experimental results have been extracted from Fig. 5 of [11]. The total photoconductor thickness is 130 μm and the n-layer thickness is 20 μm. The proposed model has a good agreement with the experimental results. We consider two discrete deep trapping states for holes in the n-layer to validate the experimental data. The depths of these two trapping states are 0.78

eV (τ_{rh1} = 13 s) and 0.83 eV (τ_{rh2} = 87 s) from the mobility edge of the valence band. This result is equivalent to a broadened state of width ~0.05 eV. The validated parameters are N_{t1} = 1.9 × 10^{15} /cm^3, N_{t2} = 4 × 10^{14} /cm^3, φ_h = 0.85 eV, and φ_e = 0.99 eV. The concentration of deep hole trap center in the n-layer is found to be ~10^{14} – 10^{15} /cm^3 (Note that the concentration of deep trap centers in the i-layer is in the range of 10^{12} – 10^{13} /cm^3) [46]. The trapped hole concentration, p_t increases with time and its saturation value is ~1.96 × 10^{14} /cm^3. It has been found that, the thermal generation current is ~0.07 pA/cm^2 whereas the carrier injection current is ~5.9 pA/cm^2.

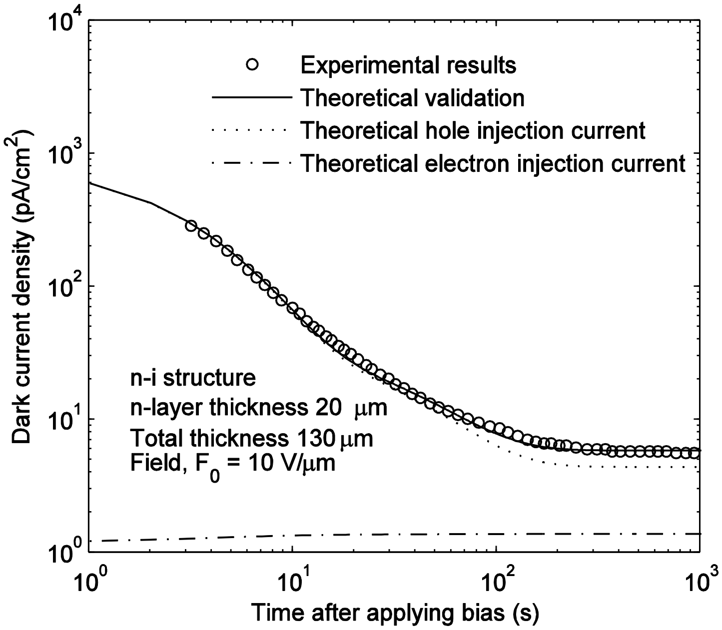

Figure 4.18 Dark current density in the n-i structure as a function of time at 10V/μm applied field. The symbol represents experimental data and the solid line represents the theoretical validation to the experimental data [11, 83].

It is evident from Fig. 4.18 that, the electron injection current is almost three times smaller than the hole injection current because of high effective barrier for the injecting electron. However, the electron current increases slightly with time since the sample does not have electron blocking layer (e.g., p-layer). Therefore, the dark current in a-Se based n-i detector is mainly controlled by hole injection, which has also been found for n-i-p/p-i-n structures.

It is instructive to compare the steady-state dark current density in the n-i structure at different applied electric fields. Figure 4.19 shows the steady-state dark current density as a function of applied electric field for the same a-Se based n-i structure shown in Fig. 4.18. The square symbol represents experimental data and the star symbol with solid line represents the theoretical validation to the experimental data. The experimental results have been extracted from Fig. 6 of [11]. The dash-dotted line represents the electron injection current and the dashed line represents the bulk thermal generation current. The proposed model shows a very good validity with the experimental result. The dark current reaches a plateau within 1000 s after the application of field as shown in Fig. 4.18. Therefore, the trapping rate equations have been solved up to 1000 s to get the steady-state dark current. The validated effective barrier for injecting holes varies from 0.89 eV to 0.85 eV with varying the applied field from 2.5 V/µm to 10 V/µm. The other parameters are the same as in Fig. 4.18. From Fig. 4.19 we find that, at steady-state, the thermal generation current is ~0.1 pA/cm^2 at 10 V/µm applied field, which is about two orders of magnitude smaller than the injection current because of large energy band-gap in a-Se. The thermal generation current increases almost exponentially with increasing the applied field.

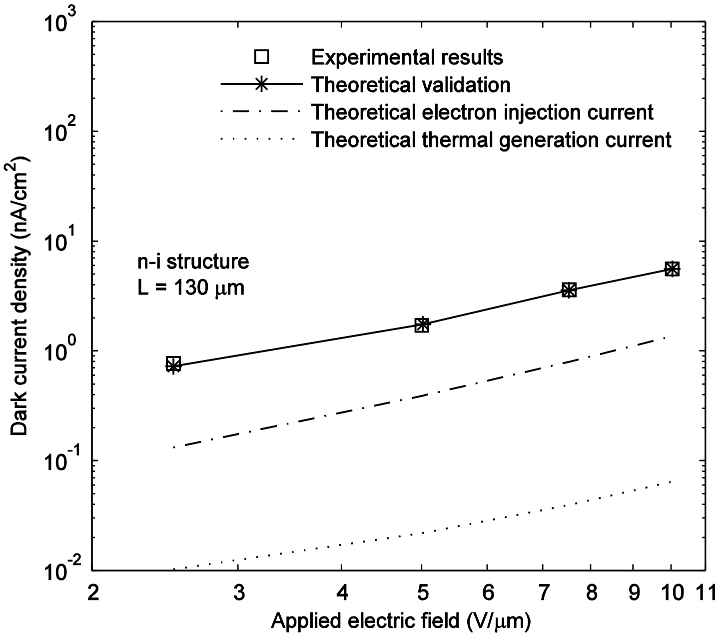

Figure 4.19 Dark current density in the n-i structure versus applied electric field. The square symbol represents experimental data and the star symbol with solid line represents the theoretical validation to the experimental data [11, 83].

It is instructive to analyze the effect of n-layer thickness on the dark current density in multilayer structures. Figure 4.20 shows the steady-state dark current density versus blocking layer (n-layer) thickness of n-i structure for two applied electric fields. The square and diamond symbols represent experimental data and the star symbols with solid lines represent the theoretical validation to the experimental data. The experimental results have been extracted from Fig. 4 of [19]. The proposed model shows a very good validity with the experimental results. The i-layer thickness is 130 μm for all the samples.

We have solved the trapping rate equation up to 1000 s to get the steady state dark current. For both the applied fields, two discrete deep trapping states for holes in the n-layer have been considered and the validated parameters are, $N_{t1} = 4\times10^{14}$ /cm^3 and $N_{t2} = 1.5\times10^{14}$ /cm^3. The depths of these trapping states are 0.77 eV (τ_{rh1} =8 s) and 0.79 eV (τ_{rh2} =18 s) from the mobility edge of the valence band. This result is equivalent to a broadened state of width ~ 0.02 eV. The validated effective barrier for injecting electrons is 0.99 eV for both the applied fields. The validated effective barrier for injecting holes varies from 0.78 eV to 0.83 eV with varying the blocking layer (n-layer) thickness from 5 μm to 50 μm.

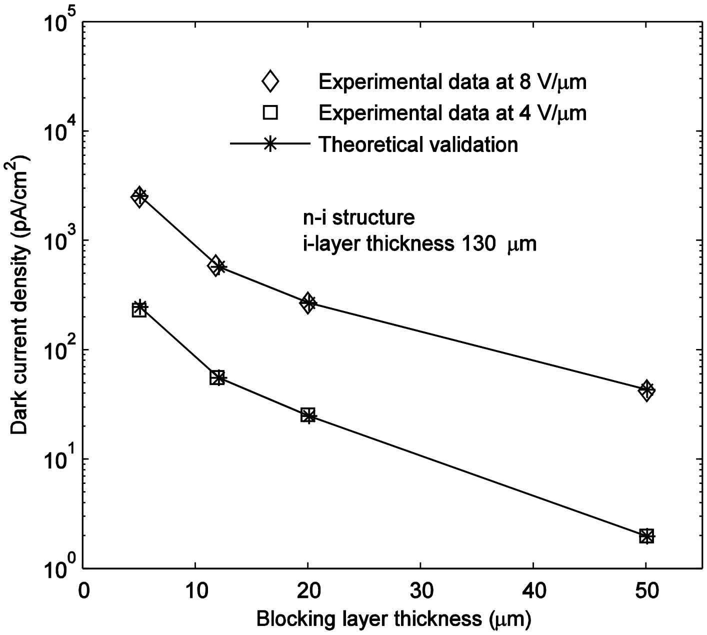

Figure 4.20 Dark current density in the n-i structure versus blocking layer (n-layer) thickness at two applied electric fields. The square and diamond symbols represent experimental data and the star symbols with solid lines represent the theoretical validation to the experimental data [19, 83].

From Fig 4.20 it is evident that, the dark current decreases with the blocking layer (n-layer) thickness. The total trap charge in the n-layer increases with the n-layer thickness, L_n and thus reduces the interface electric field $F_1(t)$ as well as the dark current. It requires more time to grow the thicker n-layer, and hence the thermal annealing occurs. Therefore, the thicker n-layer ensures more uniformity between metal and a-Se interface, and thus provides less interface states [88, 89, 94]. As a result the effective barrier for the injecting holes increases with the blocking layer (n-layer) thickness which eventually reduces the dark current in n-i structures. However, the X-ray generated carrier in the wide blocking layer (n-layer) will move slowly under lower electric field which will reduce the overall charge collection efficiency of the detector. Therefore, a tradeoff between the lower dark current (wider n-layer) and the higher sensitivity (thinner n-layer) is necessary to find an optimum n-layer thickness in n-i structures for X-ray imaging applications.

In conclusion, the steady-state dark current in n-i structure (Fig. 4.19) is higher than the n-i-p structure (Fig. 4.13). Although the n-i-p structure (Fig. 4.13) has thinner n-layer compared to the n-i structure discussed here, the hole blocking layer is cold deposited n-layer, which is less efficient in hole trapping compared to the doped a-Se based n-layer (i.e. n-layer produced by doping intrinsic a-Se).

IV. Dark current in metal/a-Se/metal structure

As mentioned before, the dark current in metal/a-Se/metal structures can be controlled by electron injection if electron barrier is low. The electron barrier depends on the work function of the negatively biased metal electrode. Figure 4.21 shows the steady-state dark current density versus work function of the negative electrode material in the metal/a-Se (n-type)/metal structure for two applied electric fields. The square and diamond symbols represent experimental data and the star symbols with solid lines represent the theoretical fit to the experimental data. The experimental results have been extracted from Fig. 5 of [19]. The dotted lines represent the electron injection current from the top electrode. The bottom electrode is Al for all the samples. The trapping rate equations have been solved up to 1000 s to get the steady-state dark current. For both the applied fields, we have considered two discrete deep trapping states for holes in the n-layer and the validated parameters are, $N_{t1} = 4 \times 10^{14}$ /cm^3 and $N_{t2} = 1.5 \times 10^{14}$ /cm^3. The depths of these trapping states are 0.77 eV ($\tau_{rh1} = 8$ s) and 0.8 eV ($\tau_{rh2} = 30$ s) from the mobility edge of the valence band. This result is equivalent to a broadened state of width ~0.03 eV. The validated effective barrier for injecting holes is ~0.82 eV for both the applied fields. The validated effective barrier for injecting electrons increases from 0.89 eV to 0.98 eV with changing the top electrode from Al to Pt.

It is evident form Fig. 4.21 that, the electron injection current is significant in the metal/a-Se (n-type)/metal structure whereas it is less significant in the multilayer (n-i, n-i-p, p-i-n) structure. It has been found that the effective barrier for injecting electron increases with the metal work function, which eventually reduces the dark current in the metal/a-Se (n-type)/metal structure. Therefore, metals with high work function used as a negative electrode can reduce the dark current.

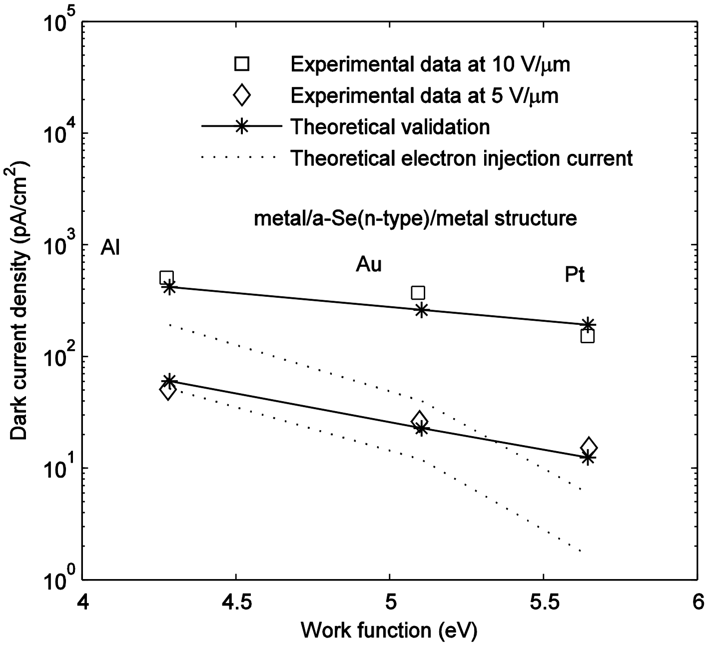

Figure 4.21 Dark current density in the metal/a-Se (n-type)/metal structure versus work function of the negative electrode material at two applied electric fields. The square and diamond symbols represent experimental data and the star symbols with solid lines represent the theoretical validation to the experimental data [83].

It is instructive to compare the steady-state dark current density in the metal/a-Se (n-type)/metal structure at different applied electric fields. Figure 4.22 shows the steady-state dark current density as a function of applied electric field for a-Se based metal/a-Se (n-type)/metal structure. The squares represent the experimental data and the solid line represents the theoretical validation to the experimental data. The experimental results have been extracted from Fig. 4 of [25]. The dotted line represents the electron injection current, the dashed line represents the hole injection current, and the dash-dotted line represents the bulk thermal generation current. The proposed model shows a very good validity with the experimental result. The trapping rate equations have been solved up to 1000 s to get the steady state dark current. Two discrete deep trapping states for holes in the n-layer have been considered. For all the applied electric fields, the depths of these two trapping states are 0.76 eV (τ_{rh1} = 5 s) and 0.81 eV (τ_{rh2} = 40 s) from the mobility edge of the valence band. This result is equivalent to a broadened state of width ~0.05 eV. For all the applied electric fields, the validated parameters are $N_{t1} = 2 \times 10^{15}$ /cm^3, $N_{t2} = 8 \times 10^{14}$ /cm^3, for both holes and electrons, respectively. The validated effective barrier for the injecting hole is ~0.93 eV for all the applied fields. The validated effective barrier for injecting electrons varies from 0.99 eV to 0.86 eV with varying the applied field from 0.96 V/µm to 10 V/µm.

From Fig. 4.22 it is evident that, at very low electric field (< 1 V/µm), the dark current mainly controlled by the electron injection. Although the electron effective barrier is higher (~0.99 eV), the dark current is dominated by the electron injection due to very high interface electric field. From 2 V/µm to 3 V/µm applied electric fields, the interface electric fields are not as high as at ~1 V/µm. Hence, the electron current is less than the hole current due to high electron effective barrier as well as low electron mobility. From 4 V/µm to 5 V/µm applied electric fields, the electron effective barrier is comparable to hole barrier. Thus, the electron current is higher than the hole current due to high interface electric field. From 6 V/µm to 10 V/µm applied electric field, the electron effective barrier varies from 0.9 eV to 0.86 eV. Therefore, the dark current mainly dominated by the electron current.

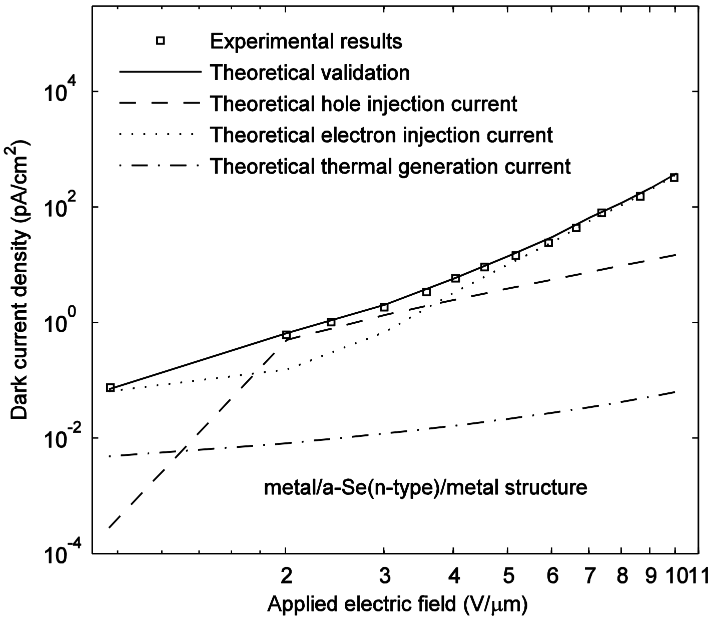

Figure 4.22 Dark current density in metal/a-Se (n-type)/metal structure versus applied electric field. The squares represent experimental data and the solid line represents the theoretical validation to the experimental data.

It is instructive to show the variation of dark current with the applied electric field in metal/a-Se (i-type)/metal structure. The intrinsic a-Se is slightly p-type, and thus electron trapping changes the electric field distribution after applying the bias. Figure 4.23 shows the steady-state dark current density as a function of applied electric field for a-Se based metal/a-Se (i-type)/metal structure. The squares represent the experimental data and the solid line represents the theoretical validation to the experimental data. The experimental results have been extracted from Fig. 6 of [11]. The dashed line represents the electron injection current, and the dotted line represents the bulk thermal generation current. The proposed model shows a very good validity with the experimental result. The trapping rate equations have been solved up to 1000 s to get the steady state dark current. Two discrete deep trapping states for electrons in the i-layer have been considered. For all the applied electric fields, the depths of these two trapping states are 1.29 eV (τ_{re1} = 1 h) and 1.27 eV (τ_{re2} = 2 h) from the mobility edge of the conduction band. These results are equivalent to a broadened state of widths ~0.02−0.03 eV. For all the applied electric fields, the validated parameters are $N_{t1} = 10^{14}$ /cm^3, $N_{t2} = 6 \times 10^{13}$ /cm^3, for both holes and electrons, respectively. The validated effective barrier for the injecting electrons is ~1 eV for all the applied fields. The validated effective barrier for injecting holes varies from 0.89 eV to 0.87 eV with varying the applied field from 1 V/μm to 10 V/μm.

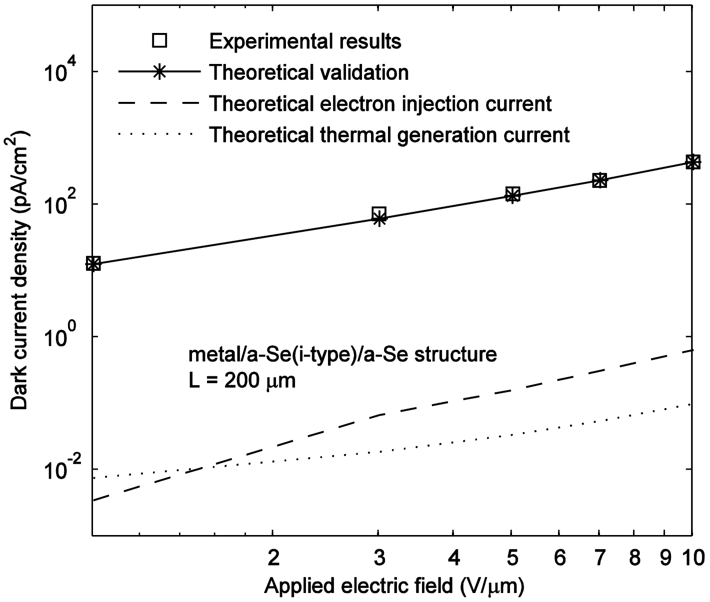

Figure 4.23 Dark current density in metal/a-Se (i-type)/metal structure versus applied electric field. The squares represent experimental data and the solid line represents the theoretical validation to the experimental data.

From Figs. 4.22 and 4.23 it is evident that, the dark current in metal/a-Se (i-type)/metal structure is mainly controlled by the hole injection, whereas in metal/a-Se (n-type)/metal structure the dark current is dominated by electron injection. Figure 4.24 compares the steady-state dark current density in the mono- and multi- layer a-Se detector structures. The acceptable limits of dark current for FPXIs are between 100 and 500 pA/cm^2 [11]. From Fig. 4.24 it is evident that, the dark current densities in the n-i-p and n-i structure are well below the acceptable range.

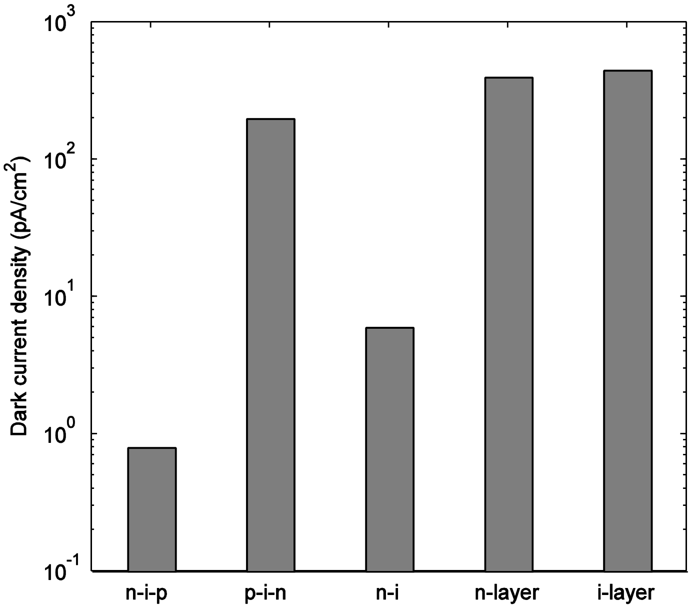

Figure 4.24 Comparison of steady-state dark current density for different a-Se based X-ray detector structures at 10 V/μm applied electric field.

In this section an analytical model for describing the transient and steady-state behavior of dark current in a-Se based detectors for X-ray imaging applications has been developed. The proposed theoretical model shows a very good agreement with the experimental results. The dark current in a-Se based detectors is mainly governed by the injection of holes from the metal electrode. The thermal generation current is much smaller compared to the injection current due to the large band gap in a-Se. The carrier injection from the metal/*n*-layer interface depends on the concentration of trap centers in the blocking layer (*n*-layer), average depth of the trap center from the valence band edge, and the effective barrier height.

4.3 Dark Current in a-Si p-i-n Photodiodes

Hydrogenated amorphous silicon (*a*-Si:H) p-i-n photodiodes are being used in large area indirect conversion medical imaging sensors and solar cells [15, 95]. The reverse-bias dark current in these applications is a sensitive measure of the device performance. In a typical *a*-Si:H p-i-n detector structure, the thickness of the i-layer is ~1 μm whereas the thickness of the p- or n- layer is ~50 nm [96]. The possible sources of dark current in *a*-Si:H p-i-n photodiodes are the bulk thermal generation in the i-layer, emission of carriers from the p-i and i-n interfaces, and contact injection [70, 97]. It has been found that, for p-i-n detector structures that provide good blocking contact layers, the contact injection currents are negligible because of almost zero electric field at the contacts.

Several theoretical models have been proposed to describe the leakage currents of *a*-Si:H p-i-n detectors [70, 98, 99, 100]. Street derived an analytical expression for the steady-state thermal generation current [70]. The steady-state thermal generation model given by Street has no voltage dependency. In practice, there is a significant voltage dependency of the steady-state thermal generation current at low biases [101]. The one-dimensional steady-state carrier transport in *a*-Si:H p-i-n detector structures under reverse bias has been studied by using amorphous semiconductor device modeling program (ASDMP) [98, 100]. All these analyses are concentrated on the steady-state reverse bias dark current. The authors of [99] investigated the transient dark current behavior in p-i-n diodes by combining Street's model for thermal generation current with the interface injection current. However, it overestimated the injection current at low biases. Therefore, a first principles model is necessary to describe the transient and steady-state dark current behavior in a-Si:H p-i-n photodiodes.

4.3.1 Analytical Model

The i-layer is slightly n-type, and thus the Fermi level, E_F at zero bias is above the mid-gap. After applying the bias, electrons are depleted from the i-layer, and the steady state quasi-Fermi level, E_{FD} lies below E_F. Figure 4.25 shows the energy band diagram near p-i interface at steady state. The quasi-Fermi level, E_{FD} bends near the interface to align with the Fermi level of the p-layer. The amount of band bending, $\Delta\phi$ within the p-layer, and near p-i interface due to the applied voltage can be determined by solving the Poisson's equation. Note that, the doping concentration near the interface can be somewhat lower than the bulk value in some structures, which creates an additional bending of the conduction band at the interface [96].

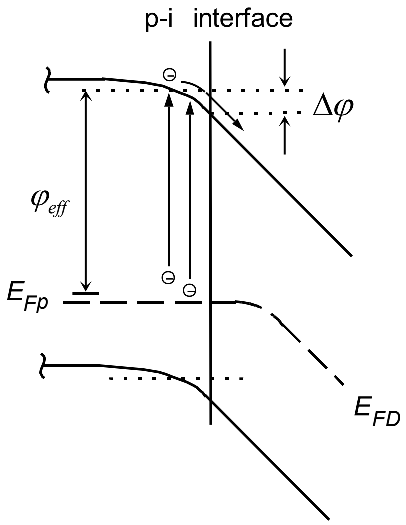

Figure 4.25 Schematic energy band diagram at the p-i interface of an a-Si:H p-i-n photodiode [85].

The width of the depletion layer in the p-region depends on the doping concentration of the p-layer [101]. Assuming full depletion of i-layer at high voltage and a constant quasi-Fermi level in the p-layer, and solving Poisson's equation at the p-i interface, the amount of band bending can be expressed as [85],

$$\Delta\varphi = \frac{\varepsilon_{si}}{2N_a} F_{pi}^2, \tag{4.31}$$

where N_a is the active dopant concentration in the p-layer, ε_{si} (= $\varepsilon_0\varepsilon_r$) is the permittivity of the amorphous silicon, and F_{pi} is the electric field at the p-i interface. Assuming built-in voltage, V_{bi} ~1.2 V and i-layer thickness of 1 μm, the built-in electric field in the i-layer is ~10^4 V/cm, whereas the typical applied field is ~10^5 V/cm [61].

The quasi-Fermi level is a function of position within a small region of thickness, x_1 in the i-layer near p-i interface. The thickness, x_1 can be expressed as [85],

$$x_1 \approx \frac{kT \ln(N_a / n_i) - \Delta\varphi}{eF_{pi}} \tag{4.32}$$

where n_i is the intrinsic carrier concentration in the i-layer. Assuming $N_a \sim 2 \times 10^{18}$ cm^{-3}, $n_i \sim 10^8$ cm^{-3}, and $F_{pi} = 10^5$ V/cm, the estimated values of $\Delta\phi = 0.016$ eV and $x_1 \sim 60$ nm [102]. Therefore, for a typical device length of about 1 μm it is reasonable to assume a constant difference between the Fermi level and the conduction band throughout the i-layer.

The initial decay in thermal generation current of *a*-Si:H detector can be explained by depletion of electrons from the i-layer. The temporal behavior of the carrier depletion process is determined by the detrapping (release) time constants. Therefore, the transient current due to electron depletion can be expressed as [85, 103],

$$J_{dep}(t) = \frac{eL}{2} \int_0^{E_C} \frac{N(E)}{\tau_r(E)} \left\{ \frac{1}{1 + \exp\left[(E - E_F)/kT\right]} - \frac{1}{1 + \exp\left[(E - E_{FD})/kT\right]} \right\} \exp\left[-\frac{t}{\tau_r(E)} \right] dE\,, \tag{4.33}$$

with mean detrapping (release) time constant,

$$\tau_r(E) = \nu_0^{-1} \exp\left[\left(E_C - E - \beta_{pf} \sqrt{F_0} \right) / kT \right] \tag{4.34}$$

where $N(E)$ is the density of states of a-Si:H at energy E in the mid-gap, F_0 (= V/L) is the applied field, V is the bias voltage, and L is the intrinsic layer thickness. Assuming uniform carrier depletion throughout the i-layer, the electric fields at the p-i and n-i interfaces can be written as,

$$F_{pi}(t) = F_0 + \frac{qL}{2\varepsilon_{si}} n_d(t), \tag{4.35}$$

$$F_{ni}(t) = F_0 - \frac{qL}{2\varepsilon_{si}} n_d(t). \tag{4.36}$$

where $n_d(t)$ is the time-dependent depleted electron concentration in the *i*-layer, F_{pi} and F_{ni} are the electric fields at the p-i and n-i interfaces respectively.

In p-i-n structure, besides thermal generation in the i-layer, electron injection through p-i interface is a possible source of current at higher fields. Hole injection through n-i interface is negligible because of the lower electric field at the n-i interface [this is also evident from Eqs. (4.35) and (4.36)], and the low hole mobility [104]. The p-i interface is a high field region, contains a high defect density and thus, at room temperature, interface field enhanced generation can be the dominating process at higher applied fields [101]. The carriers are injected from the distributed trap states near E_{Fp} at the p-i interface as shown in Fig. 4.25. We can define an effective barrier height, φ_{eff} for the injected electrons. The band bending, $\Delta\varphi$ defined previously, lowers the physical barrier at the interface in addition to Poole-Frenkel barrier lowering effect. Once the carriers are injected into the intrinsic layer, they move by drift mechanism (diffusion component of current is negligible compared its drift component because of very high applied voltage) [83]. Therefore, the reverse current density in low mobility (effective drift mobility, μ < 1 cm^2/V-s) semiconductor due to electron injection through p-i interface can be written as [20, 85],

$$J_i(t) = qN_C\mu_e F_{pi}(t)\left(\frac{v_R}{\mu_e F_{pi}(t) + v_R}\right)\exp\left\{-\frac{\varphi_{eff} - \beta_{pf}\sqrt{F_{pi}(t)} - \Delta\varphi}{kT}\right\}$$

$$\cong q\mu_e n_{inj} F_{pi}(t) \tag{4.37}$$

where n_{inj} is the average injected carrier concentration through p-i interface.

The steady-state thermal generation current in *a*-Si:H detectors arises from the carriers excited from the deep states near E_{FD} to the band edges of the intrinsic layer. The perturbation of applied electric field in the i-layer due to the space charge is usually very small. As the electric field at the p-i interface is usually 1.1~1.3 times higher than that at the n-i interface, the thermally generated carriers will move with a slightly higher velocity near p-i interface compared to near n-i interface. Therefore, assuming a constant average drift velocity of the carriers throughout the sample will not make any significant difference in the calculation of charge collection. Under thermal equilibrium condition, the trap levels are identified with the neutral defect observed by electron-spin resonance [105]. Therefore, the trapped electron and hole states are most likely charged defect (positive or negative) states, and thus field enhanced thermal generation is neglected. Considering uniform thermal emission of trapped carriers throughout the i-layer, the continuity equation of electrons at reverse bias can be written as [85],

$$\frac{\partial n(x,t)}{\partial t} + \mu_e F_0 \frac{\partial n(x,t)}{\partial x} = -\frac{1}{\tau_e} n(x,t) + g_e \,. \tag{4.38}$$

For *a*-Si:H, the thermal generation rate is dominated by the emission from traps within *kT* of E_{FD}. If the excitation rates for electrons and holes are equal, E_{FD} is very close to the middle of band-gap. The generation rate for a fully depleted sample is determined by the average carrier release time and is given by [106],

$$g = N\left(E_{FD}\right) kT \nu_0 \exp\left[-\left(E_C - E_{FD}\right)/kT\right] \tag{4.39}$$

It is assumed in Eq. (4.39) that, the density of states is constant over *kT* near E_{FD}. The steady-state thermal generation current is similar to Eqs. (4.22) and (4.23). After adding the transient and the steady-state current, the time and voltage dependent total dark current (or reverse bias current) in a-Si:H p-i-n photodiode is,

$$J_d(t) = J_{dep}(t) + J_i(t) + J_{sh} + J_{se} \tag{4.40}$$

4.3.2 Results and Discussion

The developed dark current model is validated with the published experimental data. The parameters μ_e = 1 cm^2/V-s, μ_h = 0.003 cm^2/V-s, $N_C = 6 \times 10^{20}$ /cm^3, $E_C - E_F$ = 0.81 eV, $E_C - E_{FD}$ = 0.93 eV, $\nu_0 = 10^{13}$ /s, ε_r = 11.8, $\tau_e = 3 \times 10^{-7}$ s and $\tau_h = 1.67 \times 10^{-5}$ s are taken in all calculations [107, 108]. The theoretical estimates of ν_0 varies from 10^{12} to 10^{13} /s [105]. A number of authors have taken $\nu_0 = 10^{13}$ /s in the literature [59, 70]. However, varying ν_0 from 10^{12} to 10^{13} /s does not make any change in the conclusion on the physical process of the dark current behavior. Unless otherwise specified, all the parameters mentioned above are fixed for all the theoretical calculations shown here. Other parameters such as effective barrier height and trap center concentration depend on the fabrication processes and therefore, these are considered as variable parameters in the model.

Figure 4.26 shows the transient reverse bias current of a p-i-n photodiode fabricated by conventional plasma-enhanced chemical vapor deposition (PECVD) at the applied bias voltage of -5V and -10V. The symbols represent the experimental data and the solid lines represent the theoretical validation to the experimental data. The experimental data have been extracted from Fig. 3 of [109]. For both the applied biases, the validated parameters are $N(E_{FD}) = 7 \times 10^{15}$ /cm^3/eV, $\varphi_{eff} = 1.05$ eV, and $N_a = 2.3 \times 10^{18}$ /cm^3. The dark current shows a monotonic decay to a steady-state value due to initial depletion of electrons from the i-layer. This behavior indicates that, the transient dark current is determined by the carrier depletion from the i-layer. This also supports that, PECVD photodiodes have very good junction properties. The dark current increases with the applied bias mainly due to the increase in injection current through the field dependent barrier lowering effect as described in Eq. (4.37).

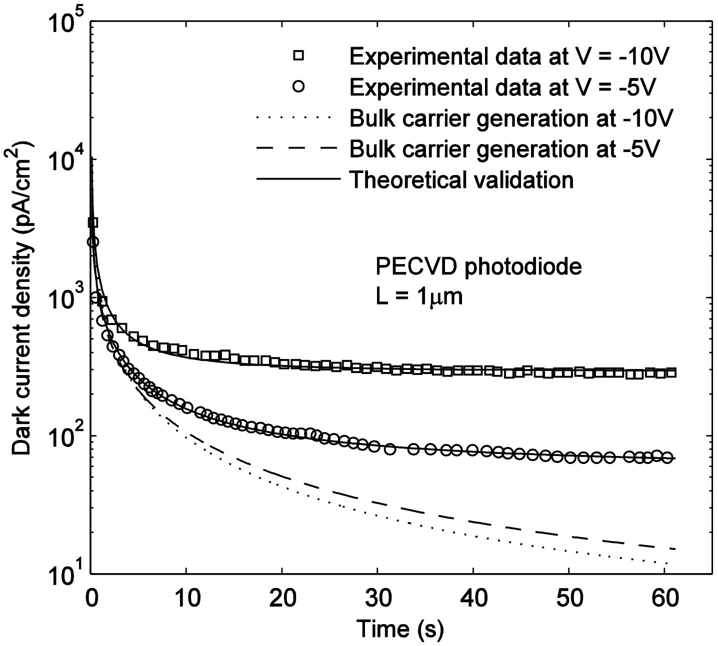

Figure 4.26 Dark current density of a PECVD photodiode as a function of time at two different bias voltages of −5 V and −10V. The symbols represent experimental data and the solid lines represent the theoretical validation to the experimental data [85, 109].

Figure 4.27 shows the steady-state leakage current of ion-shower and PECVD photodiodes as a function of reverse applied voltage. The symbols represent experimental data and the solid lines represent the theoretical validation to the experimental data. The experimental data have been extracted from Fig. 2 of [109]. For both photodiodes, the validated parameters are $N(E_{FD})$ = 1.3 × 10^{16} /cm^3/eV and N_a = 1.7 × 10^{18} /cm. The validated effective barrier heights are 1.02 eV and 1.09 eV for ion-shower and PECVD photodiodes, respectively. For ion-shower photodiode, i-layer is fabricated by the conventional PECVD method. Therefore, bulk trap center concentration is assumed to the same in both photodiodes. It is evident that, the effective barrier for injecting electrons in ion-shower photodiode is lower as compared to that in PECVD photodiode. The reverse-biased dark current in ion-shower photodiode is higher than that in PECVD photodiode mainly due to poor p-i interface properties [109].

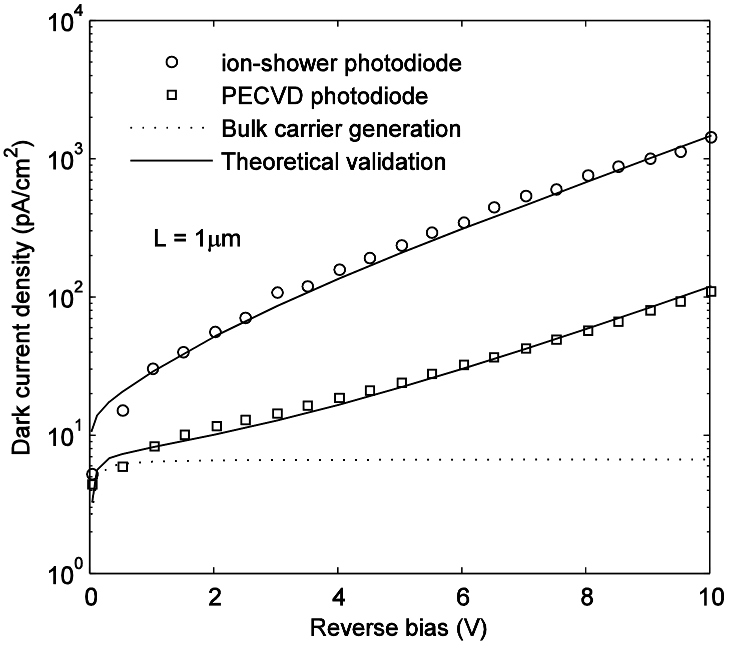

Figure 4.27 Dark current density as a function of reverse bias for the ion-shower and PECVD photodiodes. The symbols represent experimental data and the solid lines represent the theoretical validation to the experimental data [85, 109].

Figure 4.28 shows the transient reverse current density of an ion-shower photodiode at an applied electric field of 10V/μm for different radiation doses. The symbols represent experimental data and the solid lines represent the theoretical fit to the experimental data. The experimental data have been extracted from Fig. 3 of [96]. For both the radiation doses, the validated parameters are $N(E_{FD}) = 2.5 \times 10^{16}$ /cm^3/eV and $N_a = 9 \times 10^{17}$ /cm^3. The fitted effective barrier heights are 1.06 eV and 1.05 eV for 30kGy and 40kGy radiation doses respectively. The depleted carrier concentration in the i-layer and hence, the electric field at the p-i interface increase with time. The thermal generation current decreases, but the interface injection current increases with time. Therefore, the dark current decays initially and then rises to a steady-state value after full depletion of electrons from the i-layer. This behavior indicates that, the injection current is also a significant component for the transient dark current. The dark current also increases with the radiation dose. The irradiation of X-rays can create defects in the bulk as well as in the interface region, which enhances both bulk generation and interface injection current.

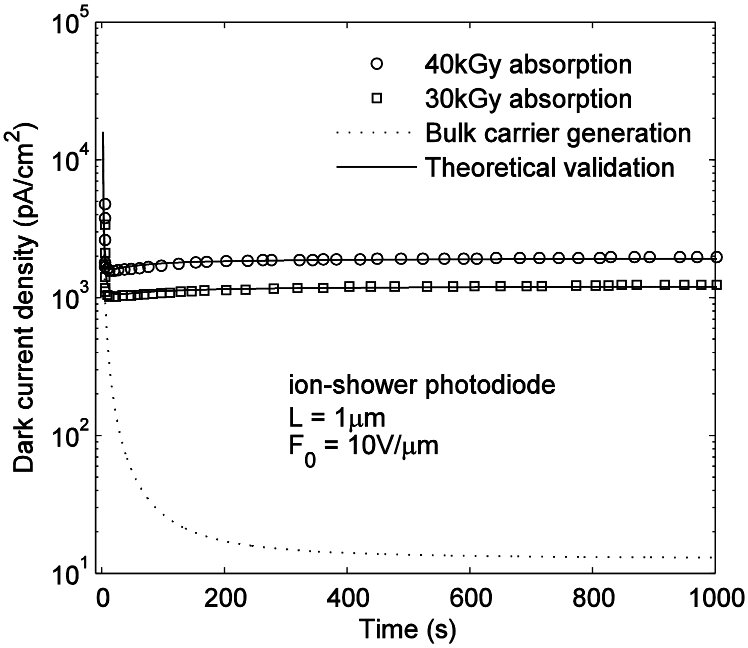

Figure 4.28 Dark current density of ion-shower photodiodes as a function of time at a bias voltage of -10 V for two different radiation doses. The symbols represent experimental data and the solid lines represent the theoretical validation to the experimental data [85, 96].

In this section, an analytical model for describing the bias-dependent transient and steady-state behavior of dark current in hydrogenated amorphous silicon (*a*-Si:H) p-i-n photodiode has been developed. There are two main component of dark current in a-Si:H p-i-n photodiode; the thermal generation in the i-layer and the electron injection through p-i interface. The proposed theoretical model shows a very good agreement with the experimental results. The validation of the physics-based model with the experimental results estimates the active dopant in the p-layer in the range of $\sim 10^{18}$ /cm^3 and the mid-gap defect density changes from $\sim 10^{16}$ /cm^3/eV to $\sim 2 \times 10^{16}$ /cm^3/eV due to X-ray radiation. Photodiodes that have very good junction properties, the high initial dark current decreases with time monotonously and reaches a plateau and, in case of poor junctions, the dark current decays initially and then rises to a steady-state value.

4.4 Dark Current in HgI$_2$ Image Detectors

Recently, poly-HgI$_2$ photoconductor are being used in large area direct conversion imaging detectors. A cross-sectional view of this detector is shown in Fig. 4.29. The barrier layer is a doped polymer material, which plays an important role to minimize the carrier injection from the metal [62]. The HgI$_2$ is grown by either physical vapor deposition (PVD) or particle-in-binder (PIB) methods. The polymer encapsulation prevents the evaporation of HgI$_2$ and thus, ensures long-term stability of the detector. The top electrode (radiation receiving electrode) is negatively biased. After applying the bias, the dark current decreases with time and reaches a plateau by ~60 s and ~1600 s for PIB and PVD detectors, respectively [62]. Until now no attempt has been made to describe the time and voltage dependent dark current behavior in poly-HgI_2 detectors. The transient dark current behavior is probably due to the depletion of charge carriers from the defect states within the band gap [62, 110]. It has been found that the HgI_2 is slightly n-type [110]. Therefore, electron depletion determines the position of quasi-Fermi level. The transient dark current is described by taking a mean detrapping time constant (Eq. 4.34) and using Eq. (4.33).

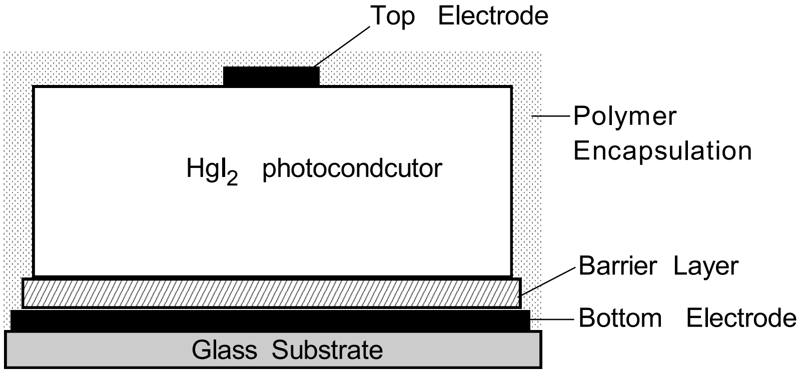

Figure 4.29 Schematic diagram of a HgI_2 detector structure. A thin polymer encapsulation is required to prevent evaporation of HgI_2.

The steady-state dark current in poly-HgI_2 detectors has two origins; (i) thermal emission of trapped carriers from the bulk and (ii) carrier injections from the metal contacts to the HgI_2 layer. It has been reported that, the thermal generation and the carrier injections are dominated by Poole-Frenkel effect and Richardson-Schottky effect, respectively [62]. The carrier injection current can be described by the thermionic-emission-diffusion theory (similar to a-Se). Assuming uniform depletion of electrons from the bulk, the interface electric fields at the metal electrodes is determined using Eqs. (4.35) and (4.36). The hole injection has been neglected considering the minimizing role of the barrier layer, the low hole mobility in HgI_2, and the low interface electric field. Considering the thermal generation rate given by Eq. (4.39) the steady-state thermal generation current is similar to Eqs. (4.22) and (4.23). The total dark current is obtained by adding the thermal generation current with the injection current.

The developed dark current model is validated with the published experimental data. The parameters μ_e = 88 cm^2/V-s, μ_h = 4 cm^2/V-s, $N_C = 3.8 \times 10^{19}$ cm^{-3}, $E_C - E_F$ = 0.95 eV, $E_C - E_{FD}$ = 1.05 eV, $N(E_{FD}) = 5.0 \times 10^{15}$ /cm^3/eV, $\nu_0 = 10^{13}$ /s, $\varepsilon_r = 8.3$ are taken in the calculations [41, 110, 111, 112]. The electron lifetimes are $\tau_e = 1.1 \times 10^{-6}$ s and τ_h = 2.5×10^{-8} s for PVD detectors [113]. In PIB detectors, the electron lifetime is an order of magnitude lower than the PVD detectors. Unless otherwise specified, all the parameters mentioned above are fixed for all the theoretical calculations shown here. The effective barrier height depends on the fabrication processes and therefore, it is considered as variable parameters in the model.

Figure 4.30 shows the steady-state dark current as a function of electric field for PVD detector. The symbols represent experimental data and the solid line represents the theoretical validation to the experimental data. The experimental data have been extracted from Fig. 3 (b) of [14]. The proposed model has a very good agreement with the experimental result. The total thickness of the sample is 280 μm. It is evident from Fig. 4.32 that, the bulk thermal generation current is considerably low compared to the electron injection current due to large energy band gap of poly-HgI_2. Therefore, the dark current in poly-HgI_2 detector is mainly controlled by the electron injection from the metal/poly-HgI_2 contact. The validated effective barrier for injecting electrons varies from 1.14 eV to 1.04 eV with varying the applied field from 0.02 V/μm to 0.65 V/μm [113].

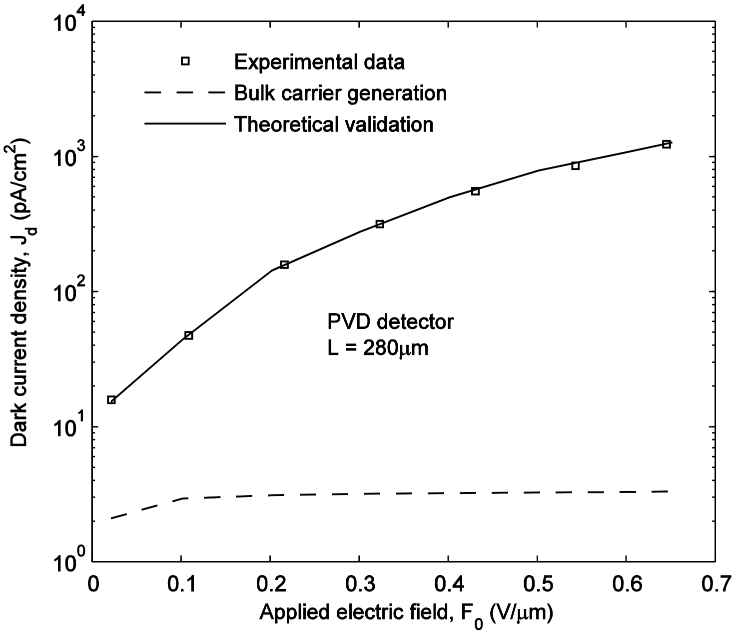

Figure 4.30 Dark current density as a function of electric field for PVD HgI_2 detector. The symbols represent the experimental data, the solid line represents theoretical validation to the experimental data and the dashed line represents the thermal generation current [14, 113].

Figure 4.31 shows the steady-state dark current as a function of electric field for another PVD detector sample. The symbols represent experimental data and the solid line represents the theoretical validation to the experimental data. The experimental data have been extracted from Fig. 5 of [62]. The proposed model has a very good agreement with the experimental result. The total thickness of the sample is 230 μm. The validated effective barrier for injecting electrons varies from 1.07 eV to 1 eV with varying the applied field from 0.2 V/μm to 2 V/μm. It is evident from Fig. 4.33 that, the dark current in this sample is mainly controlled by the electron injection.

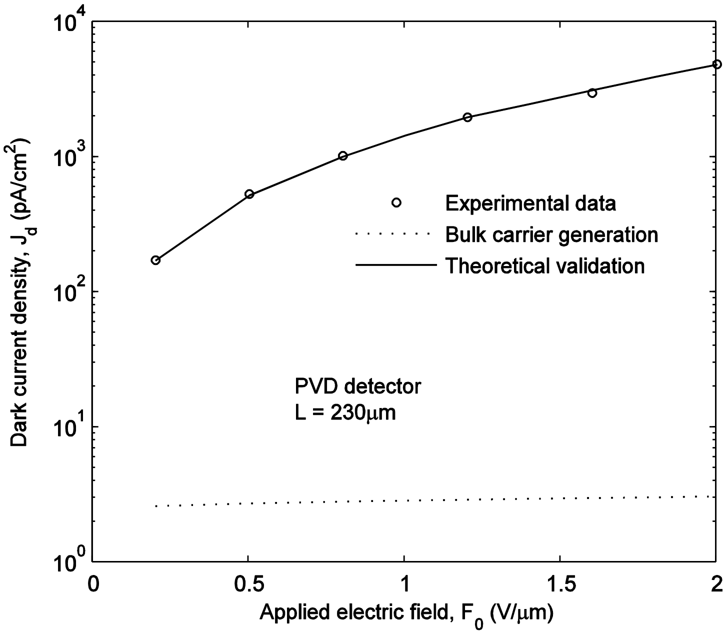

Figure 4.31 Dark current density as a function of electric field for PVD detector. The symbol represents experimental data, the solid line represents theoretical validation to the experimental data and the dotted line represents thermal generation current [62, 113].

Figure 4.32 shows the steady-state dark current as a function of electric field for PIB detector. The symbols represent experimental data and the solid line represents the theoretical validation to the experimental data. The experimental data have been extracted from Fig. 5 of [62]. The proposed model has a very good agreement with the experimental result. The total thickness of the sample is 320 μm. The validated effective barrier for injecting electrons varies from 1.1 eV to 1.06 eV with varying the applied field from 0.2 V/μm to 2 V/μm. The comparison of Figs. 4.33 and 4.34 reveals that, the dark current in the PIB detector is lower than the PVD detector due to higher electron barrier in PIB detectors.

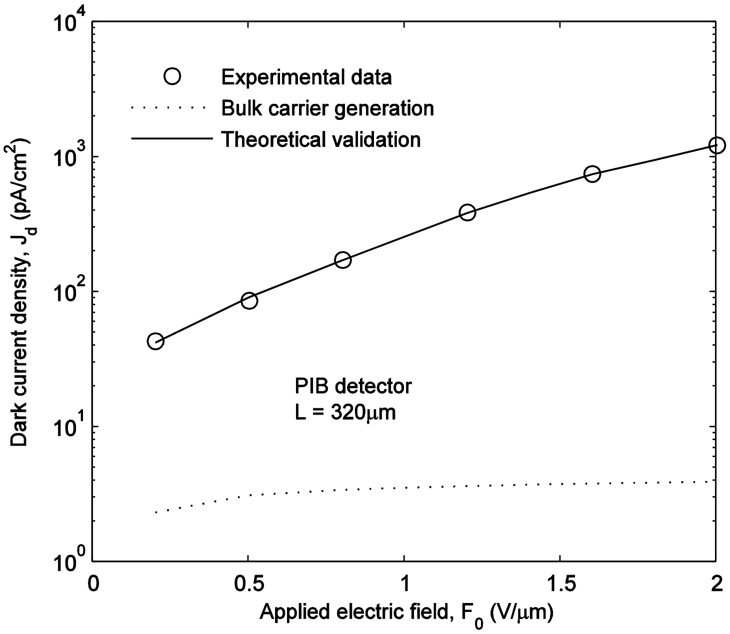

Figure 4.32 Dark current density as a function of electric field for PIB detector. The symbol represents experimental data, the solid line represents theoretical validation to the experimental data and the dotted line represents thermal generation current [62, 113].

In this section, an analytical model for describing the bias-dependent transient and steady-state behavior of dark current in poly-HgI_2 detectors has been developed. The proposed theoretical model shows a very good agreement with the experimental results. The dark current in poly-HgI$_2$ detectors is mainly controlled by the injection of electrons from the metal electrode. The bulk thermal generation current is considerably low compared to the electron injection current due to large energy band gap of poly-HgI$_2$. The validation of the physics-based model with the experimental results estimates the effective barrier height for electron injection, which varies from ~1 eV to ~1.1 eV.

4.5 Summary

In this chapter, an analytical model to describe the transient and steady-state dark current behavior in a-Se based direct conversion flat-panel X-ray image sensors has been developed. A theoretical model describing the transient and steady-state dark current in a-Si:H p-i-n photodiode has also been developed. The concept of the modeling has been used to describe the dark current mechanisms in poly-HgI$_2$ detectors. The theoretical model has been validated with the measured and published experimental results. The dark current in multilayer a-Se based detector is mainly controlled by the injection of holes from the metal electrode. For both a-Se and poly-HgI$_2$, the thermal generation current is much smaller compared to the injection current due to the large band gap. In poly-HgI$_2$ detectors, the electron injection mainly controls the dark current. The dark current in a-Si:H p-i-n photodiode is controlled by the thermal generation in the i-layer, and the electron injection through the p-i interface.

CHAPTER 5

GHOSTING AND RECOVERY MECHANISMS IN AMORPHOUS SELENIUM DETECTORS

The ghosting is defined as the change in the X-ray sensitivity of the X-ray imaging detector as a result of previous X-ray exposures. The X-ray sensitivity of an imaging detector is defined as the collected charge per unit area per unit exposure of radiation, and is an important imaging performance measure. In this chapter, a theoretical model has been developed to calculate time and exposure dependent sensitivity in multilayer a-Se based direct conversion flat-panel X-ray image sensors, which is used to describe the ghosting and its recovery mechanisms. The ghost removal technique has also been investigated here. The theoretical model has been validated with the measured experimental results for different a-Se detector structures. The samples are prepared by Anrad Corporation, Montreal, Canada. The experiments are also performed at Anrad.

5.1 Review of Ghosting in a-Se Detectors

There are several possible mechanisms, which can change the sensitivity in a-Se in subsequent X-ray exposures. The trapped charge in a-Se due to previous X-ray exposure may recombine with subsequently generated oppositely charged carriers. The effective carrier lifetime is reduced since the recombination cross-section is much higher than the trapping cross-section [114]. The trapped charges alter the electric field distribution across the photoconductor, change the conversion gain and hence, modify the free carrier generation in subsequent exposures [115, 116, 117]. It is also reported that, X-ray exposure can create new meta-stable deep trap centers in the bulk of a-Se [43, 118, 119]. Rau *et al.* measured the hole lifetime as a function of exposure or dose [120]. They observed a rapid decrease of hole lifetime at low dose, and a slow decrease at higher dose. They suggested that, the initial rapid drop in hole lifetime is due to the recombination, and the slow drop is due to the generation of X-ray induced additional deep trap centers. However, the recombination cross-section of the trapped charges and the nature of the X-ray induced meta-stable trap centers are still unknown. It has been reported that, the X-ray induced defects decay to zero over time [121]. The decay in X-ray induced defects is due to the relaxation of atomic arrangement with time. The reported structural relaxation time constant is ~15 − 30 hours [122]. Therefore, ghosting effect can be recovered by resting the sample for a long time.

It is mentioned in chapter 3 that, a-Se has both charge (VAP) and neutral (IVAP) defects. The IVAPs behave as low cross-sectional deep trapping center rather than behaving as high cross-sectional bimolecular recombination centers. The trapping of hole in IVAP (Se_1^- and Se_3^+) converts the defect of the form Se_1^0 and Se_3^+ [123]. This converted IVAP turns into an exposed positively charged defect with higher cross-section, and may participate in Langevin recombination process [43, 124, 125]. However, the release of trapped hole from the Se_1^0 defect restores the previous IVAP state. It may happen that, the Se_3^+ of the pair (Se_1^0 and Se_3^+) interact with the nearby Se_1^- to create an IVAP, and the Se_1^0 is separated from its initial pair. The energetically unfavorable Se_1^0 defect can become a stable defect as explained in chapter 3.

The trapping of electron in IVAP converts the defect into an exposed negatively charged defect (Se_1^- and Se_3^0) with a higher cross-section. This charged defect may attract a drifting hole by Langevin recombination process. It is possible that, the Se_1^- of the pair (Se_1^- and Se_3^0) interact with the nearby Se_3^+ to create an IVAP, and the Se_3^0 is separated from its initial pair. The unstable Se_3^0 defect can be transformed to VAP. From the above discussion it is suggestive that, only a certain fraction of the trapped charges act as recombination centers for oppositely charged drifting carriers [126].

Several works describe the ghosting mechanisms in a-Se based detectors by considering a metal/a-Se/metal (called monolayer structure) detector structure [26, 120]. In a-Se, the carriers trapped by neutral defects participate in a recombination process following the Langevin recombination mechanism. On the other hand, those carriers that are trapped by the charged defects become inactive after being trapped. In previous analyses, it has been found that assuming charge trapping by the neutral defects only, the experimental results cannot be validated without using an effective recombination factor, which is less than the Langevin recombination coefficient. This suggests that, not all the trapped charges are available for recombination. In this thesis, we consider carrier trapping in both charged and neutral defect states. The relative amount of the existing charged and neutral defect states, and the nature of X-ray induced trap centers are determined by fitting the model with the experimental data.

In this thesis, the ghosting mechanisms have been studied in multilayer a-Se mammography detectors by considering carrier transport (including trapping, recombination, trap filling and detrapping) in all three layers, space charge effects, electric field dependent electron-hole pair creation energy, carrier injection from the metal contacts, and X-ray induced meta-stable deep trap center generations. The effect of dark current is also considered in the ghosting model. Note that, the dark current has a significant effect on the variation in X-ray sensitivity when the amount of injected carriers is comparable to the amount of X-ray generated carriers. The ghosting recovery mechanisms (e.g., recombination between trapped and oppositely charged free carrier, trapping of oppositely charged free carriers, or relaxation of trap centers) in a-Se detectors are also studied in this research work. The theoretical ghosting recovery model considers that, the trapped carriers are released exponentially and also, the total amount of meta-stable trap centers is decreased exponentially with time.

The characteristic release times for the trapped holes and electrons are in the range of a few minutes and several hours, respectively. The trapped holes are released quickly, but the trapped electrons remain in the sample on the time scale of hours. Therefore, the ghosting effect can be minimized if the trapped electrons could be removed from the selenium bulk after each exposure. This work suggests a ghost removal technique by reversing the bias polarity during the natural recovery process under no irradiation. We have also tried to recover sensitivity by shining blue light from the back contact. The theoretical model considers carrier injection from the metal contacts during the reverse bias. The validation of the simulation results with the experimental data quantitatively explains the carrier dynamics and the sensitivity recovery mechanisms under reverse bias.

5.2 Experimental Details

The time and exposure dependent relative sensitivity in n-i-p a-Se mammography samples under positive bias is measured. The selenium layers are thermally evaporated on indium tin oxide (ITO) coated glass, acting as the bottom electrode and allowing good surface preparation. During the evaporation process, stabilized a-Se (a-Se alloyed with 0.2–0.5% As and doped with 10–40 ppm Cl) is deposited to form the i-layer in between the blocking layers. Alloying pure a-Se with As greatly improves the stability of the composite film, and helps to prevent crystallization. A metallic electrode is then deposited on the structure to form the top electrode. For the purpose of the actual study, the structure described above was found to be a good representative of commercially available a-Se detectors.

Figure 5.1 shows the schematic diagram of the experimental setup. The mammography X-ray source has molybdenum (Mo) anode, and an internal 30 μm Mo filter. The thickness of the added aluminum (Al) filter is 2 mm. The X-ray exposure is measured in roentgen (R) by a dosimeter, which is connected to an ion chamber. The ion chamber is placed at a distance of 46 cm from the X-ray port and 12 cm above the detector top electrode in order to reduce the effect of back scatter from the detector. The exposure at the detector entrance is calculated using the inverse square law. The detector sample is connected to a dual mode power supply, which can provide both positive and negative voltages. The output signal from the detector is amplified and viewed on the oscilloscope. A gain of 10^7 is used to amplify the signal current. The filter reduces the effect of noise on the output signal. The output signal is transferred to a host computer, which controls the different experimental sequences.

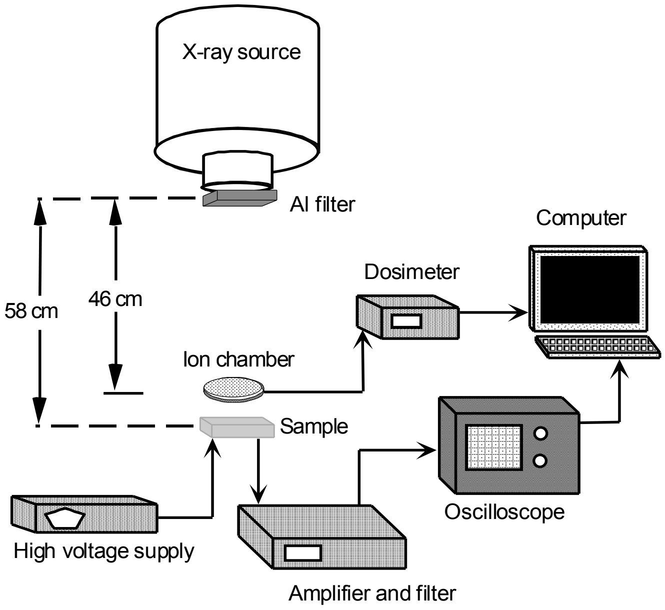

Figure 5.1 Schematic diagram of the experimental setup for ghosting and recovery measurement.

The experimental sequences of the ghosting and recovery experiment are demonstrated in Fig. 5.2. Initially, probe pulses are applied to measure the sensitivity {step (i) of Fig. 5.2}. For probe pulses, a potential of 25 kVp has been set at 32 mA-s. The typical duration of a probe pulse is 50−250 ms and there is a time interval of 2 minutes between two successive probe pulses. Following the probe pulses, the ghost pulse is applied. For the ghost pulse, a potential of 28 kVp has been set at 400 mA-s. During ghosting, the added Al filter has been removed. The dose of the ghost pulse (>60 R) is much higher than that of the probe pulse (<14 mR). Hence a desirable amount of ghost is achieved. In step (iii), the natural recovery process begins in which the probe pulses are again applied to measure the sensitivity. After a few probe pulses to measure the sensitivity during the natural recovery process, the bias polarity is reversed and the magnitude is changed. After applying the reverse bias for 1 minute, the bias is restored to the initial operating bias and the sensitivity is measured.

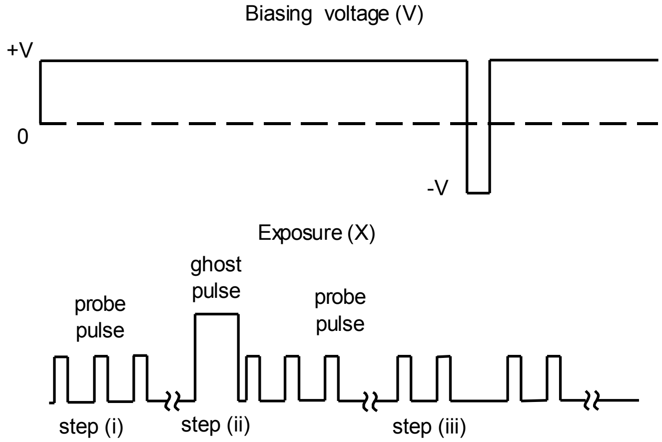

Figure 5.2 Steps for time and exposure dependent ghosting measurement and simulation; (i) initial probe pulses, (ii) ghost pulse, and (iii) probe pulses during the recovery process and the switching of the biasing voltage.

5.3 Analytical Model

A theoretical model to investigate the ghosting and its recovery mechanisms in multilayer a-Se detectors has been developed considering the following effects; (i) carrier trapping in both charged and neutral defect states, (ii) recombination of drifting carrier with trapped carriers, (iii) X-ray induced meta-stable deep trap centers, (iv) instantaneous electric field profile and field dependent carrier generation, (v) effect of dark current on trapped carrier distribution, (vi) collection of detrapped holes and dark signal, (vii) exponential release of trapped charges, and (vii) relaxation of meta-stable trap centers over time. The amounts of carrier injections due to dark current and detrapped carriers are much smaller than that of X-ray generated carriers. Therefore, the effects of dark current and carrier detrapping on the carrier dynamics during exposure are neglected. However, these effects are considered during the interval between two successive X-ray exposures.

Consider a multilayer X-ray image detector with a thickness *L*, which is biased with a voltage *V* to establish an electric field in the photoconductor as shown in Fig. 5.3. It is assumed that, the diffusion of the carriers is negligible compared with their drift component because of the very high applied voltage [20]. It is also assumed that, the effective carrier mobility μ is constant throughout the photoconductor thickness [127]. Therefore, the continuity equations for holes and electrons can be written as [128],

$$\frac{\partial n'}{\partial t'} - \mu_e \frac{\partial (n'F')}{\partial x'} = \gamma' e^{-\alpha x'} - C_{Le} n' p'_{tc} - n'\left(\frac{1}{\tau'_{ce}} + \frac{1}{\tau'_{ne}}\right), \tag{5.1}$$

$$\frac{\partial p'}{\partial t'}+\mu_h\frac{\partial(p'F')}{\partial x'}=\gamma' e^{-\alpha x'}-C_{Lh}p'n'_{tc}-p'\left(\frac{1}{\tau'_{ch}}+\frac{1}{\tau'_{nh}}\right), \tag{5.2}$$

where x' is the distance from the top electrode, t' is the time, $p'(x', t')$ is the free hole concentration, $n'(x', t')$ is the free electron concentration, $p'_t(x', t')$ is the trapped hole concentration, $n'_t(x', t')$ is the trapped electron concentration, $F'(x', t')$ is the electric field, $\gamma'(x', t')$ is the EHP generation rate, τ' is the deep trapping time, α is the linear attenuation coefficient of the photoconductor, C_{Le} is the recombination coefficient between free electrons and trapped holes, and C_{Lh} is the recombination coefficient between free holes and trapped electrons. The subscripts c and n are associated with charged and neutral defect states, respectively and the subscripts e and h represent electrons and holes, respectively. Note that in the continuity equations, bulk recombination between free electrons and holes are neglected due to the small signal radiation.

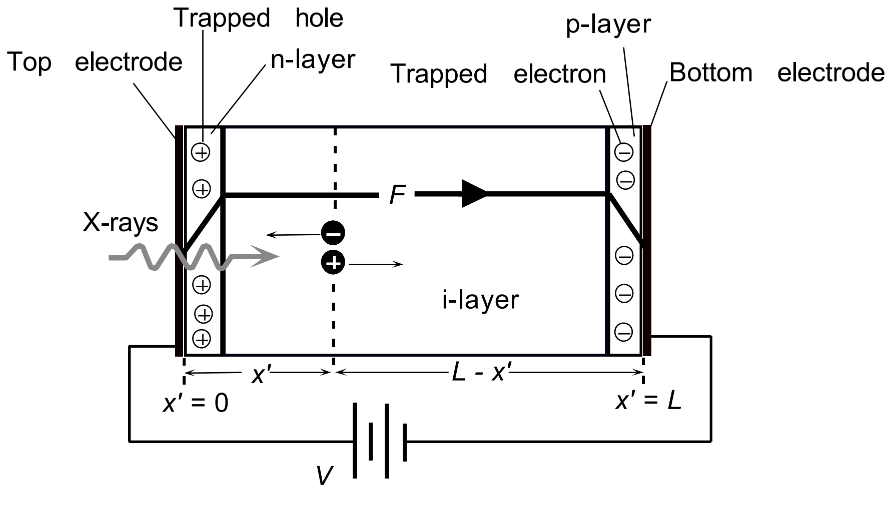

Figure 5.3 Schematic diagram of a multilayer a-Se based X-ray image detector. The electron-hole pairs are generated at *x* and then follow the electric field *F*.

It has been reported that the recombination process in a-Se follows the Langevin mechanism [124]. Hence, the recombination coefficient is expressed by,

$$C_{Lh(e)} = \frac{q\mu_{h(e)}}{\varepsilon_{se}} \tag{5.3}$$

where q is the elementary charge and ε_{se} (= $\varepsilon_0\varepsilon_r$) is the permittivity of a-Se photoconductor.

The initial deep trapping time, $\tau_0 = 1/(C_tN_0)$, where C_t is the capture coefficient and N_0 is the initial concentration of deep trap centers. If the trapped carrier concentration due to previous exposure is large, the available deep trap centers to trap the carriers generated by subsequent exposure are reduced. This mechanism is known as the trap filling effect. On the contrary to trap filling effect, the X-ray induced deep trap centers generation process increases the total concentration of deep trap centers. In this analysis, the X-ray induced trap centers are assumed to be charged defects. Therefore, the carrier trapping times can be expressed as [128],

$$\tau'_{ne} = \frac{\tau'_{0ne}}{1 - n_{tc}/N_{0ne}}, \tag{5.4}$$

$$\tau'_{ce} = \frac{\tau'_{0ce}}{1 + \left(N_{Xe} - n_{tn}\right)/N_{0ce}}, \tag{5.5}$$

$$\tau'_{nh} = \frac{\tau'_{0nh}}{1 - p_{tc}/N_{0nh}}, \tag{5.6}$$

$$\tau'_{ch} = \frac{\tau'_{0ch}}{1 + \left(N_{Xh} - p_{tn}\right)/N_{0ch}}, \tag{5.7}$$

where N_X is the concentration of the X-ray induced deep trap centers.

The concentration of X-ray induced meta-stable deep trap centers depends on the amount of exposure, the irradiation energy, and the photoconductor material. It is assumed that, the X-ray induced deep trap center generation kinetics follows a first order rate law [128]. Thus the concentration of X-ray induced meta-stable deep trap centers can be written as,

$$N_{Xe}(X) = N_{sat(e)}\left(1 - e^{-X/\xi}\right), \tag{5.8}$$

$$N_{Xh}(X) = N_{sat(h)}\left(1 - e^{-X/\xi}\right), \tag{5.9}$$

where N_{sat} is the saturation value of the X-ray induced deep trap centers, ξ is an irradiation energy dependent constant, and X is the amount of accumulated exposures. The unit of ξ and X is R. The trapping rate equations in the charged and neutral defect states are [128],

$$\frac{\partial n'_{tc}}{\partial t'} = -C_{Lh} p' n'_{tc} + \frac{n'}{\tau'_{ne}}, \tag{5.10}$$

$$\frac{\partial n'_{tn}}{\partial t'} = \frac{n'}{\tau'_{ce}}, \tag{5.11}$$

$$\frac{\partial p'_{tc}}{\partial t'} = -C_{Le} n' p'_{tc} + \frac{p'}{\tau'_{nh}}, \tag{5.12}$$

$$\frac{\partial p'_{tn}}{\partial t'} = \frac{p'}{\tau'_{ch}}. \tag{5.13}$$

The Poisson's equation relates the gradient of the electric field to the local space charge, and is given by,

$$\frac{\partial F'}{\partial x'} = \frac{q}{\varepsilon_{se}}\left[p' + p'_{tc} + p'_{tn} - n' - n'_{tc} - n'_{tn}\right]. \tag{5.14}$$

The physical equations have been simplified using the normalized distance, $x = x'/L$, the normalized attenuation depth, $\Delta = 1/\alpha L$, and the normalized electric field, $F = F'/F_0$. The time coordinate is normalized with respect to the longest transit time between the two types of carriers (for a-Se we consider the electron transit time, $t_e = L/\mu_e F_0$). Therefore, the normalized time coordinate, $t = t'/t_e$. The hole and electron life-times are normalized by their respective transit times, and thus, $\tau_h = \mu_h \tau'_h F_0/L$ and $\tau_e = \mu_e \tau'_e F_0/L$.

The physical equations described in this chapter are normalized to simplify the calculation. The charge carrier concentrations are normalized with respect to the total X-ray generated charge carriers per unit area, Q_0 (electrons/m^2) in the photoconductor, assuming that the total charge carriers are uniformly distributed over the sample volume. Consider γ_0 as the EHP generation rate for a uniform electric field of F_0 throughout the photoconductor layer. Then, the total collectable EHPs, which are generated in the photoconductor layer, can be expressed as [129],

$$Q_0 = p_0 L = \int_0^{T_e}\int_0^{L} \gamma_0 e^{-\alpha x'} dx' dt' = \frac{\gamma_0 T_e \eta}{\alpha} = \frac{5.45\times 10^{17}\left(X\eta\right)}{\left(\alpha_{en}/\rho\right)_{air} W_0}\left(\frac{E_{ab}}{E_{ph}}\right) \tag{5.15}$$

where $\eta = 1 - e^{(-1/\Delta)}$ is the quantum efficiency of the detector, T_e is the exposure time, X is the exposure in Roentgens, W_0 is the EHP creation energy of the photoconductor for electric field of F_0 and incident photon energy of E_{ph}, E_{ab} is the average absorbed energy, $(\alpha_{en})_{air}$ and ρ_{air} are the energy absorption coefficient and the density of air, respectively. The unit of $(\alpha_{en}/\rho)_{air}$ is in cm^2/g.

Using the normalized parameters described above, the physical equations can be expressed as,

$$\frac{\partial n}{\partial t} - \frac{\partial (nF)}{\partial x} = Ge^{-x/\Delta} - k_0 n p_{tc} - n\left(\frac{1}{\tau_{ce}} + \frac{1}{\tau_{ne}}\right) \tag{5.16}$$

$$\frac{\partial p}{\partial t} + f_\mu \frac{\partial (pF)}{\partial x} = Ge^{-x/\Delta} - k_0 f_\mu p n_{tc} - f_\mu p\left(\frac{1}{\tau_{ch}} + \frac{1}{\tau_{nh}}\right) \tag{5.17}$$

$$\frac{\partial n_{tc}}{\partial t} = -k_0 f_\mu p n_{tc} + \frac{n}{\tau_{ne}} \tag{5.18}$$

$$\frac{\partial n_{tn}}{\partial t} = \frac{n}{\tau_{ce}} \tag{5.19}$$

$$\frac{\partial p_{tc}}{\partial t} = -k_0 n p_{tc} + f_\mu \frac{p}{\tau_{nh}} \tag{5.20}$$

$$\frac{\partial p_{tn}}{\partial t} = f_\mu \frac{p}{\tau_{ch}} \tag{5.21}$$

$$\frac{\partial F}{\partial x} = k_0\left[p + p_{tc} + p_{tn} - n - n_{tc} - n_{tn}\right] \tag{5.22}$$

where $n = n'/p_0$, $p = p'/p_0$, $n_t = n'_t/p_0$, $p_t = p'_t/p_0$, $f_\mu = \mu_h/\mu_e$, $k_0 = eQ_0/\varepsilon_{se}F_0$. In (5.15) and (5.16), $G(x,t) = (t_e W_0)/[\eta \Delta T_e W(x,t)]$, where $W(x,t)$ is the EHP creation energy at the instantaneous electric field $F(x,t)$.

During dark period, the physical equations are still valid except the carrier generation term in the continuity equations has to be replaced by the carrier injection rate [127]. The injection current densities are given by (4.2) and (4.3). The normalized expressions of electron and hole injection rates are given by,

$$g_{dh}(0,t)=\frac{N_V t_e}{p_0 T_e}\left(\frac{v_R}{\mu_e F(0,t)+v_R}\right)\exp\left\{-\frac{\varphi_h-\beta_s\sqrt{F(0,t)}}{kT}\right\} \tag{5.23}$$

$$g_{de}(1,t)=\frac{N_C t_e}{p_0 T_e}\left(\frac{v_R}{\mu_e F(1,t)+v_R}\right)\exp\left\{-\frac{\varphi_e-\beta_s\sqrt{F(1,t)}}{kT}\right\} \tag{5.24}$$

where $F(0,t)$ is the instantaneous electric field at the metal/n-layer interface and $F(1,t)$ is the instantaneous electric field at the metal/p-layer interface.

The nonlinearly coupled physical equations are simultaneously solved by the finite difference method. It has been assumed that, after applying high voltage, there is a sufficient time interval so that the dark current reaches the steady-state before any exposure. We also assume that, there are trapped charges in the blocking layers; however no initial trapped charge in the intrinsic layer. Therefore, the initial conditions are; $n(x,0) = 0$ and $p(x,0) = 0$ in all three layers, $p_{tc}(x,0) = p_{tc0}$, $p_{tn}(x,0) = p_{tn0}$, $n_{tc}(x,0) = 0$ and $n_{tn}(x,0) = 0$ in the n-layer, $n_{tc}(x,0) = n_{tc0}$, $n_{tn}(x,0) = n_{tn0}$, $p_{tc}(x,0) = 0$ and $p_{tn}(x,0) = 0$ in the p-layer. The boundary condition is given by,

$$\int_0^1 F(x,t)dx = 1 \tag{5.25}$$

The normalized expression of total current density due to X-ray generated carriers is [26],

$$j(t) = \int_0^1 F(x,t)\left[n(x,t) + r_\mu p(x,t)\right]dx \, . \tag{5.26}$$

The normalized collected charge or charge collection efficiency is calculated by integrating the total current over the time period of interest. The normalized X-ray sensitivity is given by the product of the normalized collected charge and the quantum efficiency.

During the ghosting experiment a considerable amount of hole detrapping is expected. When the detrapped carrier moves through the photoconductor, it can be trapped again in an arbitrary position, and can later be detrapped. For simplicity, we take an average detrapping time and neglect further trapping to calculate the resultant amount of detrapped carriers. The hole detrapping probability is [1-exp(-t_{off} / τ_{rh})], where τ_{rh} is the average detrapping (release) time and t_{off} is the time gap between two successive X-ray exposures (Fig. 5.2). The current density due to detrapping of holes at positive bias is given by [103],

$$j_{rh}(t) = \int_0^1 \frac{p_t(x,t)e^{-(t/\tau_{rh})}}{\tau_{rh}}(1-x)dx \, . \tag{5.27}$$

The amount of collected charges due to detrapped holes is calculated by integrating (5.27) over the time gap (i.e., dark-time). The collected charge due to the detrapped holes is added to the collected charges due to the X-ray exposure and the dark current.

The reduced sensitivity of a ghosted sample is eventually recovered with time when the sample is rested. During the resting period, exponential release of the trapped carriers and exponential decay of the total meta-stable trap centers have been considered [127]. Therefore, the time dependent trapped carrier concentrations and X-ray induced meta-stable trap centers are given by [28],

$$p_t(x,t+\Delta t) = p_t(x,t)e^{-\Delta t/\tau_{re}} \tag{5.28}$$

$$n_t(x,t+\Delta t) = n_t(x,t)e^{-\Delta t/\tau_{re}} \tag{5.29}$$

$$N_{Xh}(X,t+\Delta t) = N_{sat(h)}\left(1-e^{-X/\xi}\right)e^{-\Delta t/\tau_{Nh}} \tag{5.30}$$

$$N_{Xe}(X,t+\Delta t) = N_{sat(e)}\left(1-e^{-X/\xi}\right)e^{-\Delta t/\tau_{Ne}} \tag{5.31}$$

where Δt is the infinitesimally small time step, $\tau_{rh(e)}$ is the release time of holes (electrons), and τ_N is the characteristic decay time for the X-ray induced meta-stable trap centers.

5.4 Results and Discussions

The ghosting and recovery experiments have been carried out under a low positive applied electric field (~1−2 V/μm) for mammography. A very little ghost has been found under normal operating applied electric fields (~5−10 V/μm) due to small thickness of the sample and low energy. In other studies (e.g., chest radiology), a significant amount of ghosting has been found under normal operating applied fields [28]. The purpose of this research is to investigate the ghosting and its recovery mechanisms using the available measurement facilities. The measurement is carried out following the sequences of Fig. 5.2. The X-ray sensitivity is calculated as a function of accumulated X-ray exposures and time. The relative X-ray sensitivity is obtained by normalizing the sensitivity by the expected sensitivity before any X-ray exposure [130]. The numerical model is validated with the experimental data. Figure 5.4 shows the relative sensitivity of an n-i-p detector structure as a function of accumulated X-ray exposures and time. The symbols represent the experimental data and the solid line represents the theoretical validation to the experimental data [128]. The dashed line represents the relative sensitivity considering hole detrapping only, and the dashed-dotted line represents the relative sensitivity considering electron detrapping only. The mammography sample, 1152 has a total photoconductor thickness of 204 μm. The thicknesses of the n- and p-layers are 6 μm and 5 μm, respectively. The average photon energy is ~18.9 keV for a 25 kVp applied X-ray spectrum with 2 mm Al filtration. The applied electric field is ~1 V/μm. After obtaining the change in sensitivity for 8 probe pulses within the first 16 minutes, the ghost pulse is applied. The exposure for each probe pulse is 11.4 mR and the exposure for the ghost pulse is 62 R. The ghost exposure ends at time $t = 0$. After the ghost pulse, the probe pulses are again applied to measure the sensitivity. During this time, the ghosted sample recovers by a natural process and therefore, it is termed as natural recovery.

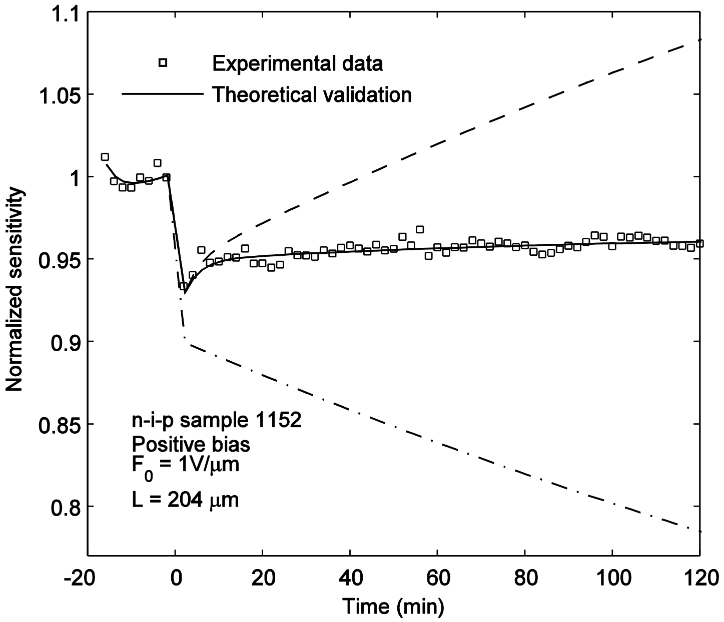

Figure 5.4 Relative X-ray sensitivity as a function of exposure and time showing natural recovery for the sample 1152 at 1 V/μm applied electric field. The symbols represent the experimental data and the solid line represents the theoretical fit to the experimental data [128]. The dashed line represents the relative sensitivity considering hole detrapping only and the dashed-dotted line represents the relative sensitivity considering electron detrapping only.

The $\mu\tau$ (mobility-lifetime product) values of carriers in the intrinsic layer are ~168.2 × 10^{-6} cm^2/V and ~2 × 10^{-6} cm^2/V for holes and electrons, respectively. The drift mobility, μ is measured by time-of-flight (TOF) experiments and the lifetime, τ is measured by interrupted field time-of-flight (IFTOF) experiments [84]. For both holes and electrons, the validated neutral trap centers for all the three layers (n-i-p) is $N_{0n} = 10^{17}$ /m^3. In the n-layer, the validated charged trap centers are $N_{0ce} = 4.91 \times 10^{18}$ /m^3 and N_{0ch} = 1.5×10^{21} /m^3, whereas in the *p*-layer these are 1.5×10^{21} /m^3 and 7.8×10^{16} /m^3, for electrons and holes, respectively. In the *i*-layer, the validated charged trap centers are 4.91×10^{18} /m^3 and 7.8×10^{16} /m^3, for electrons and holes, respectively. Unless otherwise specified, all the parameters mentioned above are fixed for all the simulations shown in this paper. For both holes and electrons, the validated N_{sat} and ξ are 1.05×10^{19} /m^3 and 100 R, respectively. The validated detrapping (release) times for holes and electrons are 3.5 minutes and 1.3 hours, respectively. The validated recovery time constant for meta-stable trap centers is 48 hours [122]. The sensitivity drops to ~93% by the high dose ghost pulse mainly due to the creation of X-ray induced meta-stable trap centers and the recombination of the drifting carriers with the oppositely charged trapped carriers [128].

It is evident from Fig. 5.4 that, there are two distinct regions of recovery; (i) an initial faster recovery, and (ii) a subsequent slow recovery. The faster recovery is due to the release of trapped holes, which are added to the collected charge. The slow recovery is due to the relaxation of the X-ray induced trap centers and the trap filling by the generated electrons owing to probe pulses. It has been found that, the relatively faster electron release rate as compared to the relaxation rate of the X-ray induced trap centers results empty trap center available for further trapping of electrons, which eventually slows down the rate of recovery. The sensitivity is expected to reach the initial sensitivity level, naturally, by resting the sample longer than the recovery time constant of the meta-stable trap centers [128].

It is instructive to show the electric field distribution during the ghosting recovery. Figure 5.5 shows the electric field distribution across the photoconductor for the conditions of Fig. 5.4. Before any exposure, there exist trapped carriers in the blocking layers, but no trapped carriers in the i-layer (as evident from the solid line in Fig. 5.5).

During ghosting, the electric field in the n-layer increases with accumulated X-ray exposure as trapped electrons in the i-layer are much higher compared to trapped holes. During recovery, trapped holes are released and trapped electrons fill the existing trap centers in the sample. Thus the electric field increases in the n-layer.

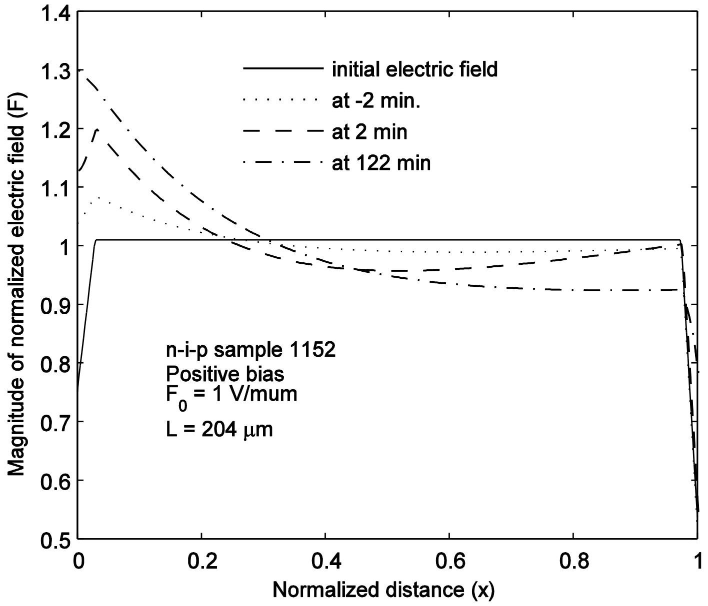

Figure 5.5 The change in electric field during ghosting and natural recovery for the conditions of Fig. 5.4.

During the experiment of ghosting and recovery the dark current is mixed up with the X-ray photocurrent. Thus, it is difficult to measure dark current at the presence of X-ray exposures. The X-ray photocurrent is usually few orders of magnitude higher than the steady-state dark current. Figure 5.6 shows the simulated relative magnitude of dark current with respect to the initial dark current as a function of time for the conditions of Fig. 5.4. The dark current is calculated by the model described in chapter 4. The validated effective barrier height for hole injection from the top electrode is 0.89 eV, and the initial dark current density is 3.1 pA/cm^2. The dark current density is calculated at the end of the dark time (2 minutes), and right before the next probe pulse. During ghosting and recovery process, the dark current increases due to increased electric field in the n-layer as explained before. However, the dark current is expected to decrease towards the initial value by resting the sample longer than the recovery time constant of the X-ray induced meta-stable trap centers.

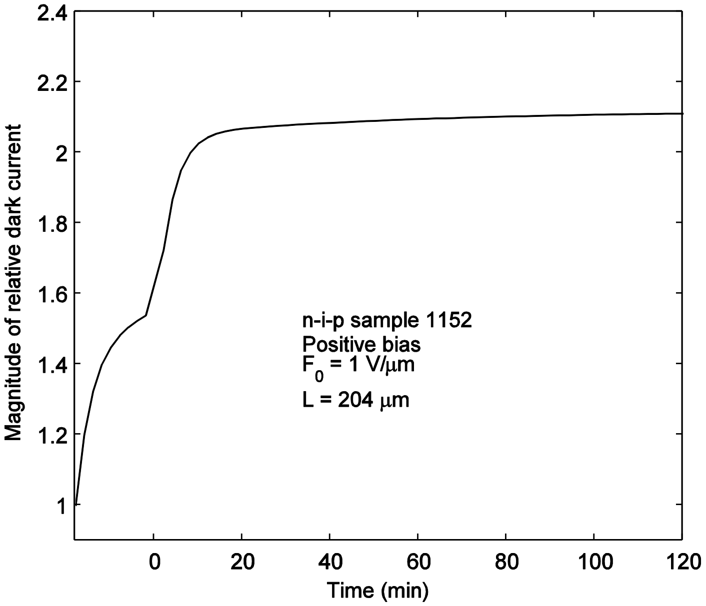

Figure 5.6 Relative dark current versus time for the conditions of Fig. 5.4.

In this thesis, a ghost removal technique is investigated by reversing the bias during natural recovery process. Figure 5.7 shows the relative sensitivity as a function of accumulated X-ray exposures and time for an n-i-p detector structure. In this case, the bias voltage has been reversed for 1 minute during natural recovery (the experimental sequences are shown in Fig. 5.2). The symbols represent the experimental data and the solid line represents the theoretical validation to the experimental data [131]. The simulated curve shows a good agreement with the experimental data. The applied electric field is ~1 V/μm. The sample 1149 has the same carrier range and thickness as the sample 1151. After obtaining the change in sensitivity for 5 probe pulses within the first 10 minutes, the ghost pulse is applied. The exposure for each probe pulse is 15.5 mR and the exposure for the ghost pulse is 69 R. After 20 minutes of natural recovery, the field is reversed to ~1.0 V/μm and held for 1 minute. Then the field is restored to the initial positive polarity, and the probe pulses are applied to measure the sensitivity. The validated parameters are $N_{sat} = 2.15 \times 10^{19}$ /m^3 and $\xi = 200$ R, for both holes and electrons. The validated detrapping times of holes and electrons are 2 minutes and 1.5 hours, respectively. The validated effective barrier height is ~0.72 eV for both electrons and holes, during the reverse bias. The other parameters are the same as in Fig. 5.4. From Fig. 5.7 it is evident that, the relative sensitivity increases abruptly due to the effects of reverse bias. During the reverse bias, it is expected that a huge number of holes drift through the photoconductor layer. It is believed that, the faster recovery is due to the recombination of the trapped electron with the injected holes. A detail physical explanation for the abrupt increase in sensitivity will be presented later part of this chapter.

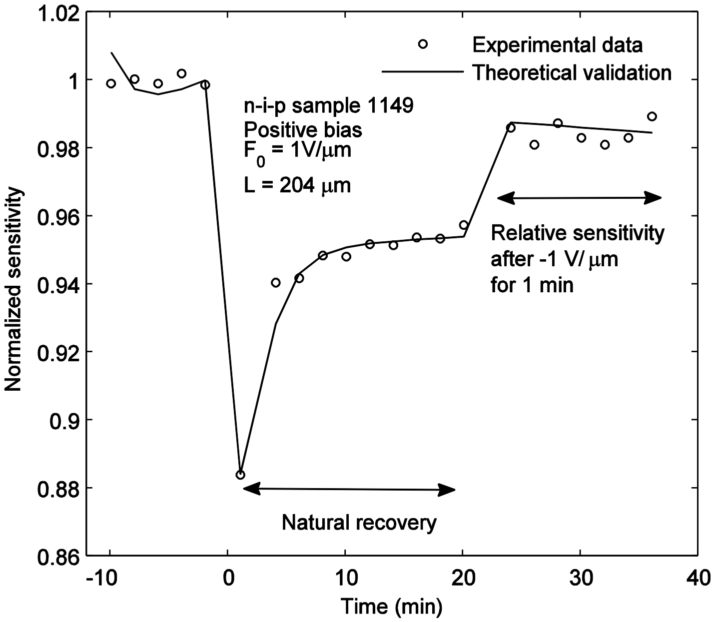

Figure 5.7 Relative X-ray sensitivity as a function of exposure and time showing the natural recovery as well as the recovery after reverse bias for the sample 1149 at 1 V/μm applied electric field. The magnitude of reverse field is 1 V/ μm. The symbols represent the experimental data and the solid line represents the theoretical validation to the experimental data [131].

It is instructive to observe the effects of the magnitude of reverse bias on the recovery process. Figure 5.8 shows the relative sensitivity as a function of accumulated X-ray exposures and time for the sample 1149. In this case, the magnitude of the field due to reverse bias has been increased to ~1.5 V/μm. The symbols represent the experimental data and the solid line represents the theoretical validation to the experimental data. The simulated curve shows a good agreement with the experimental data. The applied electric field is ~1 V/μm. After obtaining the change in sensitivity for 8 probe pulses within the first 16 minutes, the ghost pulse is applied. The exposures for probe and ghost pulses are the same as in Fig 5.7. After 22 minutes of natural recovery, the field is reversed to ~1.5 V/μm and held for 1 minute. Then the field is restored to the initial positive polarity, and the probe pulses are applied to measure the sensitivity. The validated N_{sat} is 1.3×10^{19} /m^3 for both holes and electrons. The detrapping times of holes and electrons are 2.5 minutes and 1.1 hours, respectively. The validated effective barrier height is ~0.73 eV for both electrons and holes, during the reverse bias. The other parameters are the same as in Fig. 5.7.

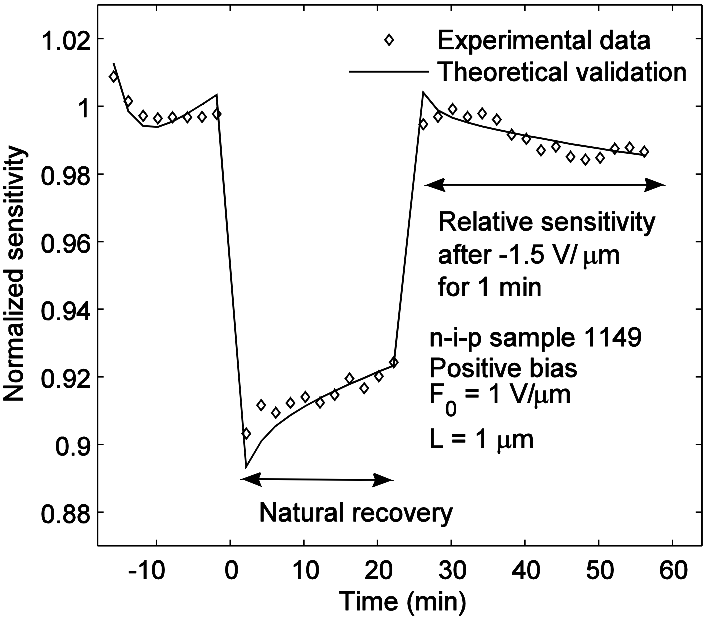

Figure 5.8 Relative X-ray sensitivity as a function of exposure and time for the sample 1149 at ~1 V/μm applied electric field. The magnitude of reverse field is ~1.5 V/ μm. The symbols represent the experimental data and the solid line represents the theoretical validation to the experimental data.

It is evident from Figs. 5.7 and 5.8 that, the relative sensitivity increases to 100% by increasing the magnitude of reverse bias. At higher reverse bias, it is expected that more carriers will be injected and then will recombine with the existing trapped carriers. From

Fig. 5.8 it is evident that, after the relative sensitivity decreases slowly the abrupt recovery. The physical reasons for this slow decrease in sensitivity will be explained with experimental results in the later part of this chapter.

It is instructive to study the ghosting and recovery at different applied electric field for the same sample. Figure 5.9 shows the relative sensitivity as a function of accumulated X-ray exposures and time for the sample 1149. The symbols represent the experimental data and the solid line represents the theoretical validation to the experimental data. The simulated curve shows a good agreement with the experimental data. The applied electric field is ~2 V/µm. After obtaining the change in sensitivity for 5 probe pulses within the first 10 minutes, the ghost pulse is applied. The exposures for probe and ghost pulses are the same as in Fig 5.7. The magnitude of the applied electric field due to reverse bias is ~1 V/µm. The validated N_{sat} is 1.3×10^{19} /m^3, for both holes and electrons. The validated detrapping times of holes and electrons are 3.5 minutes and 1 hour, respectively. The validated effective barrier height is ~0.75 eV, for both electrons and holes during the reverse bias. The other parameters are the same as in Fig. 5.7. From Fig. 5.9 it is evident that, the amount of ghosting is less compared to Figs. 5.7 and 5.8. At higher operating biases, ghosting is less due to reduced trapping and recombination, which is also found by previous analysis [127]. It is evident from Fig. 5.9 that, the recovery rate is very small after the reverse bias. Therefore, it is necessary to increase the magnitude of reverse bias.

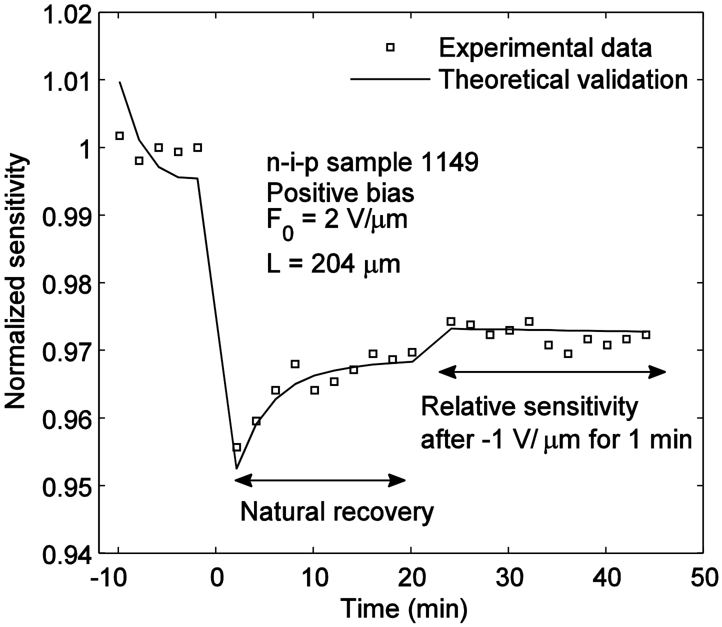

Figure 5.9 Relative X-ray sensitivity as a function of exposure and time for the sample 1149 at 2 V/μm. The magnitude of reverse electric field is 1 V/ μm. The symbols represent the experimental data and the solid line represents the theoretical validation to the experimental data.

Figure 5.10 shows the relative sensitivity as a function of accumulated X-ray exposures and time for the sample 1149. The symbols represent the experimental data and the solid line represents the theoretical validation to the experimental data [131]. The simulated curve shows a good agreement with the experimental data. The applied electric field is ~2 V/μm. After obtaining the change in sensitivity for 7 probe pulses within the first 14 minutes, the ghost pulse is applied. The exposures for probe and ghost pulses are the same as in Fig 5.7. After 20 minutes of natural recovery, the field is reversed to ~1.5 V/μm and held for 1 minute. Then the field is restored to the initial positive polarity, and the probe pulses are applied to measure the sensitivity. The validated N_{sat} is 2.3 × 10^{19}

/m^3, for both holes and electrons. The detrapping times of holes and electrons are 2.5 minutes and 1.3 hours, respectively. The validated effective barrier height is ~0.72 eV for both the electrons and holes, during the reverse bias. The other parameters are the same as in Fig. 5.7. From Figs. 5.7 and 5.10 it is evident that, a higher magnitude of reverse bias is required to get faster recovery at higher operating bias.

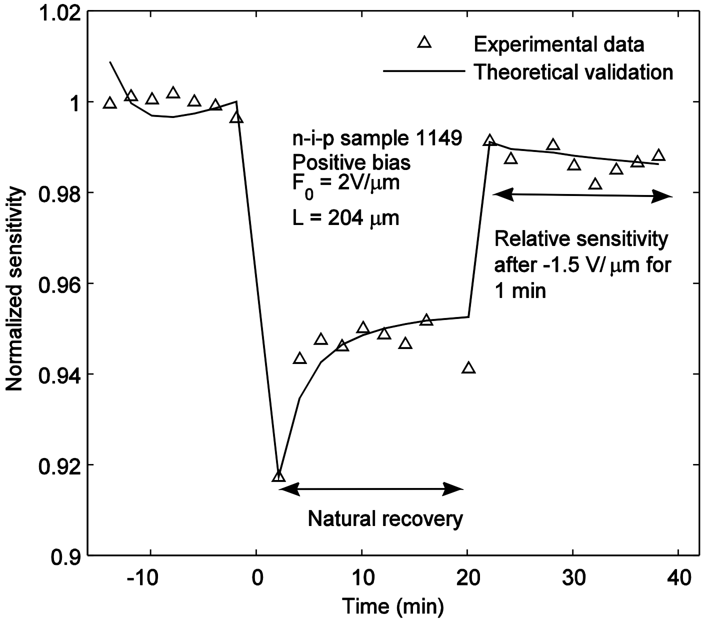

Figure 5.10 Relative X-ray sensitivity as a function of exposure and time for the sample 1149 at 2 V/μm. The magnitude of reverse electric field is 1.5 V/ μm. The symbols represent the experimental data and the solid line represents the theoretical validation to the experimental data [131].

It is instructive to monitor the sensitivity recovery for hours after reverse bias to find a conclusive physical reason of the abrupt recovery. Figure 5.11 shows the relative sensitivity as a function of accumulated X-ray exposures and time for the sample 1152.

The symbols represent the experimental data and the solid line represents the theoretical fit to the experimental data. The applied electric field is ~1 V/μm. After obtaining the change in sensitivity for 5 probe pulses within the first 10 minutes, the ghost pulse is applied. The exposure for each test pulse is 11.6 mR and the exposure for the ghost pulse is 60 R. After 20 minutes of natural recovery, the field is reversed to ~1.0 V/μm, and held for 1 minute. Then the field is restored to the initial positive polarity, and the probe pulses are applied to measure the sensitivity. The simulated curve shows a good agreement with the experimental data. The fitted value of N_{sat} is 1.1×10^{19} /m^3, for both holes and electrons. The detrapping time of electrons is 1 hour. The other parameters are the same as in Fig. 5.4. Figure 5.11 shows a fast increase in relative sensitivity due to the effects of reverse bias.

During reverse bias, huge number of carriers is injected from the metal electrodes. Some of the injected carriers recombine with the existing trapped charges, but most of them are trapped as evident from Figs. 5.12 and 5.13 later. Therefore, the relative sensitivity recovers abruptly due to less trapping of carriers by the effect of trap filling. It has been found that, the faster electron release rate as compared to the relaxation rate of the X-ray induced trap centers results in empty trap centers available for further trapping of electrons. Therefore, the slow decrease in sensitivity after the interim reverse bias is due to the lower characteristic release time of the trapped electrons as compared to the higher characteristic recovery time of the X-ray induced meta-stable trap centers. It has been found by simulation that, a higher electron release time and (or) a lower induced trap center recovery time ceases the decrease in relative sensitivity after the interim reverse bias, and the relative sensitivity eventually reaches the initial sensitivity.

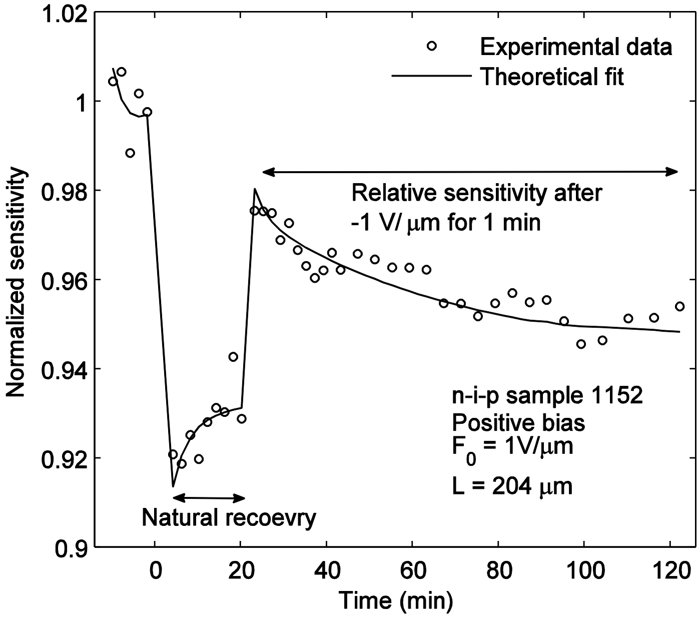

Figure 5.11 Relative X-ray sensitivity as a function of exposure and time showing the natural recovery as well as the recovery after reverse bias for the sample 1152 at 1 V/μm applied electric field. The symbols represent the experimental data and the solid line represents the theoretical fit to the experimental data [128].

Figure 5.12 shows the simulated trapped electron concentration across the detector structure at different times for the conditions of Fig. 5.11. It is evident from Fig. 5.12 that, just after the reverse bias, the trapped electron concentration in the sample increases. The release of these trapped electrons over time results in more electron trapping during subsequent exposures. Therefore, the relative sensitivity gradually decreases.

Figure 5.13 shows the simulated trapped hole concentration across the sample at different times for the conditions of Fig. 5.11. It is apparent from Fig. 5.13 that, the trapped holes release quickly and, therefore the collected charge due to the detrapped holes makes a significant contribution to increase the relative sensitivity immediately after the interim reverse bias. From Figs. 5.12 1nd 5.13 it is evident that, both trapped electron and hole concentrations are increased by the injected carriers from the metal contacts at reverse bias. That means, during the reverse bias, the rate of trapping of carriers exceeds the rate of recombination between the drifting carriers and the oppositely charged trapped carriers, which is counter intuitive.

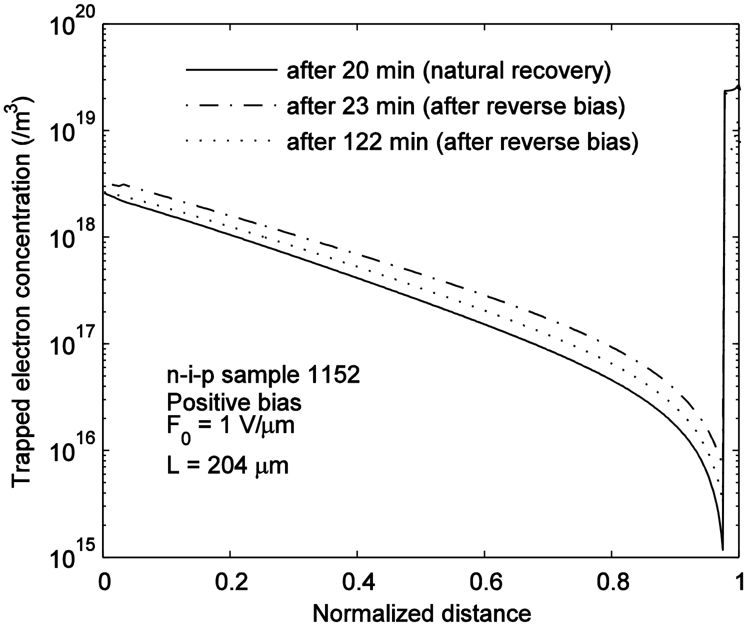

Figure 5.12 Trapped electron concentration across the detector structure before and after the interim reverse bias for the conditions of Fig. 5.11 [128].

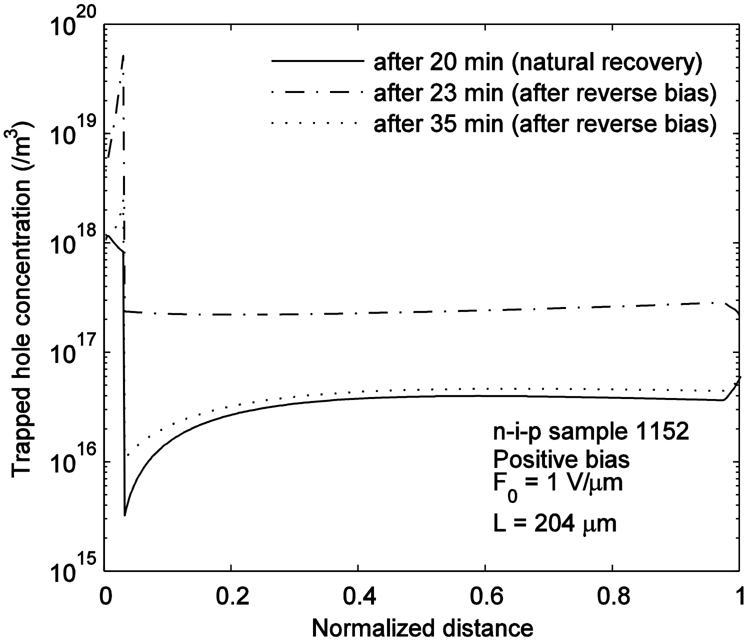

Figure 5.13 Trapped hole concentration across the detector structure before and after the interim reverse bias for the conditions of Fig. 5.11 [128].

Figure 5.14 shows the simulated relative magnitude of dark current with respect to the initial dark current as a function of time for the conditions of Fig. 5.11. The validated effective barrier height for hole injection from the top electrode is 0.89 eV, and the initial dark current density is 3.1 pA/cm^2. The dark current density is calculated at the end of the dark time (2 minutes), and right before the next probe pulse. The validated effective barrier heights for both the injected holes and electrons are ~0.73 eV in the calculation of dark current during the reverse bias. There is an increase in dark current during initial probe pulses, and it quickly reaches a plateau. However, during natural recovery, the dark current increases at slower rate and the rate of increase in dark current gradually reaches a plateau. The electric fields at the metal contacts increase with time at the beginning of the natural recovery process, which leads to the increase of the dark current. Later, the electric fields at the metal contacts decrease, and hence the dark current decays slowly over time during the natural recovery process. Figure 5.15 shows the electric field distributions across the photoconductor during the transition of the biases. The initial field is shown for a reference as well. During the interim reverse bias, the injected holes become trapped in the n-layer, which increases the electric field at the metal/n-layer interface. Due to the reverse bias, the dark current increases to almost three orders (~3.1 nA/cm^2) of the initial value as shown in Fig. 5.14. After the bias has been restored, the electric field at the metal/n-layer interface decreases, which reduces the dark current.

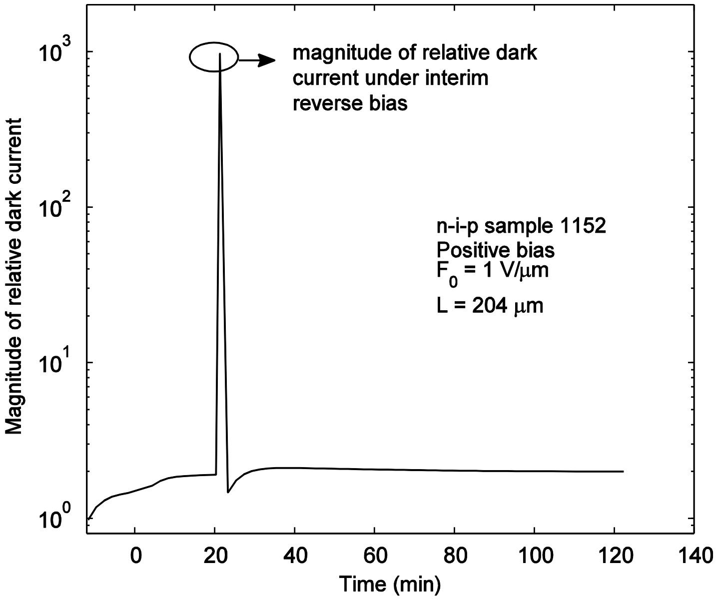

Figure 5.14 Relative dark current versus time for the conditions of Fig. 5.11. The current is negative at reverse bias [128].

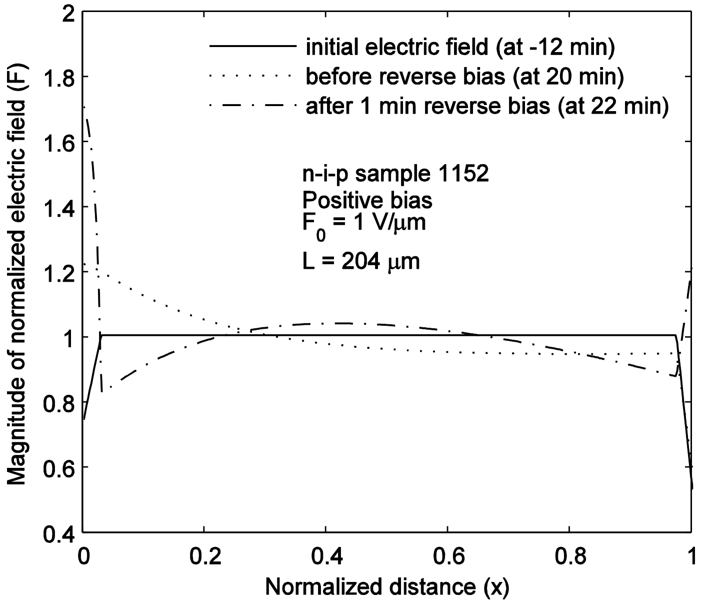

Figure 5.15 The change in electric field before and after reverse bias for the conditions of Fig. 5.11. The electric field is negative under reverse bias [128].

It is instructive to observe the effects of the magnitude of reverse bias on the recovery process for a longer period (~hours). Figure 5.16 shows the relative sensitivity as a function of accumulated X-ray exposures and time for the sample 1152. The symbols represent the experimental data and the solid line represents the theoretical validation to the experimental data. The exposure for each probe pulse is 13.6 mR and the exposure for the ghost pulse is 63 R. In this case the magnitude of the applied field during reverse bias has been increased to ~1.5 V/μm. The simulated curve shows a good agreement with the experimental data. The value of N_{sat} is 1.25×10^{19} /m^3, for both holes and electrons. The validated detrapping time of holes and electrons are 3 minutes and 1.25 hours, respectively. The validated effective barrier heights for both the injected holes and electrons are ~0.74 eV during the reverse bias. The other parameters are the same as in

Fig. 5.11. It is evident from Fig. 5.16 that, the ghost has been eliminated after the interim reverse bias. Comparing Figs. 5.11 and 5.16 it is conclusive that, an increased magnitude of reverse bias results in faster sensitivity recovery. It has been found that, the duration of the reverse bias can also be increased to have a faster sensitivity recovery.

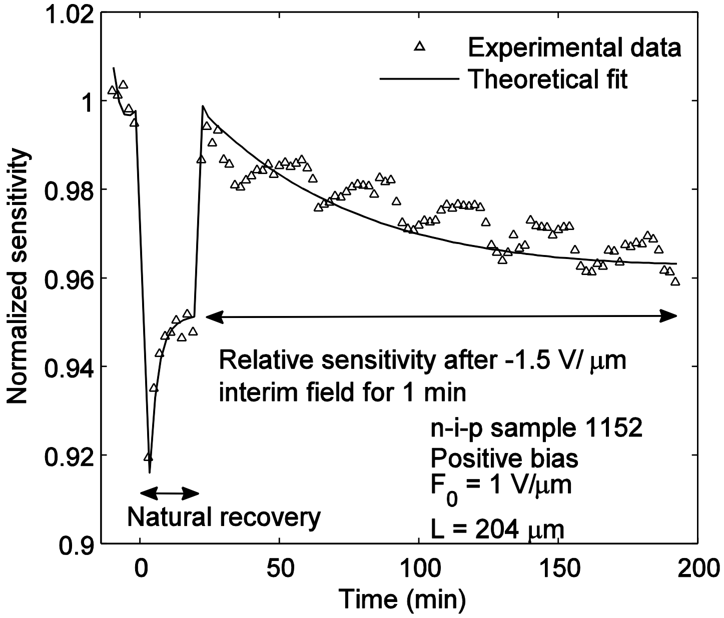

Figure 5.16 Relative X-ray sensitivity as a function of exposure and time for the sample 1152. The magnitude of the electric field due to reverse bias is ~1.5 V/μm. The symbols represent the experimental data and the solid line represents the theoretical validation to the experimental data [128].

The effect of increased magnitude of reverse bias has been investigated further. Figure 5.17 shows the relative sensitivity as a function of accumulated X-ray exposures and time for the sample 1149. The symbols represent the experimental data and the solid line represents the theoretical validation to the experimental data. The exposure for each probe pulse is 15.5 mR and the exposure for the ghost pulse is 69 R. In this case, the magnitude of the field due to reverse bias has been increased to ~2.5 V/μm. The simulated curve shows a good agreement with the experimental data. The value of N_{sat} is 1.65×10^{19} /m^3 for both holes and electrons. The detrapping time of holes and electrons are 3 minutes and 2.2 hours, respectively. The validated effective barrier heights for both the injected holes and electrons are ~0.71 eV during the reverse bias. The other parameters are the same as in Fig. 5.10. It is evident from Fig. 5.17 that, the relative sensitivity reaches to 110% after the interim reverse bias due to trap filling effect. However, the actual sensitivity is less than the trap-limited sensitivity (i.e., the sensitivity reduction due to trapping only). In this case, the sensitivity is mostly limited by recombination after the reverse bias.

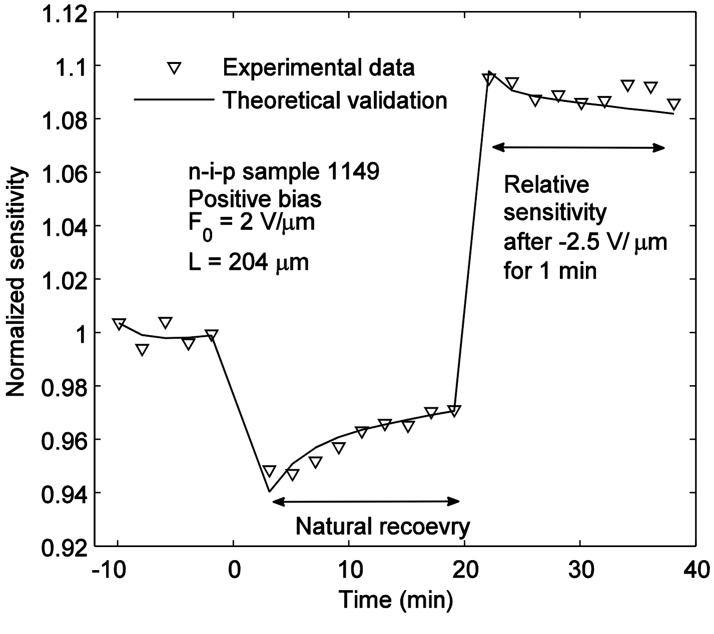

Figure 5.17 Relative X-ray sensitivity as a function of exposure and time for the sample 1149 at ~2 V/μm applied electric field. The magnitude of the electric field due to reverse bias is ~2.5 V/μm. The symbols represent the experimental data and the solid line represents the theoretical validation to the experimental data.

It is observed from Figs. 5.4, 5.11, and 5.16 that, there exist some oscillations in the sensitivity recovery curves. However, the magnitude and frequency of this oscillation depend on samples and experimental conditions. This oscillation occurs most probably because of some instantaneous fluctuations of trapping and release events. Considering the characteristic trapping and release times in the theoretical model, the simulation results show an average tendency which match with the average trends of the measured values.

The sensitivity recovery by shining blue light from the back (charge collection electrode) without reversing the bias has been investigated, but this method is not very successful in n-i-p detector structures. The principle of shining blue light is to create a huge number of holes near the interface, and let them drift through the photoconductor layer. These holes supposed to recombine with the trapped electrons, which can recover the initial sensitivity. In practice, most of the light generated carriers are lost in the blocking layers right after their generation, and thus no effect has been found.

The sensitivity recovery by shining light under reverse bias has also been investigated. Figure 5.18 shows the relative sensitivity as a function of accumulated X-ray exposures and time for the sample 1149. After obtaining the change in sensitivity for 6 probe pulses within the first 12 minutes, the ghost pulse is applied. The exposure for each test pulse is 15.5 mR and the exposure for the ghost pulse is 69 R. After 20 minutes of natural recovery, the field is reversed to ~1.0 V/μm and held for 1 minute. During this time the sample is shined by the blue light from the back (charge collection electrode) for

20 s. Then the field is restored to the initial positive polarity, and the probe pulses are applied to measure the sensitivity. After 46 minutes, the field is reversed to ~1.5 V/µm and held for 1 minute. During this time, the sample is shined by the blue light (charge collection electrode) for 20 s. Then the field is restored to the initial positive polarity, and the sensitivity is measured.

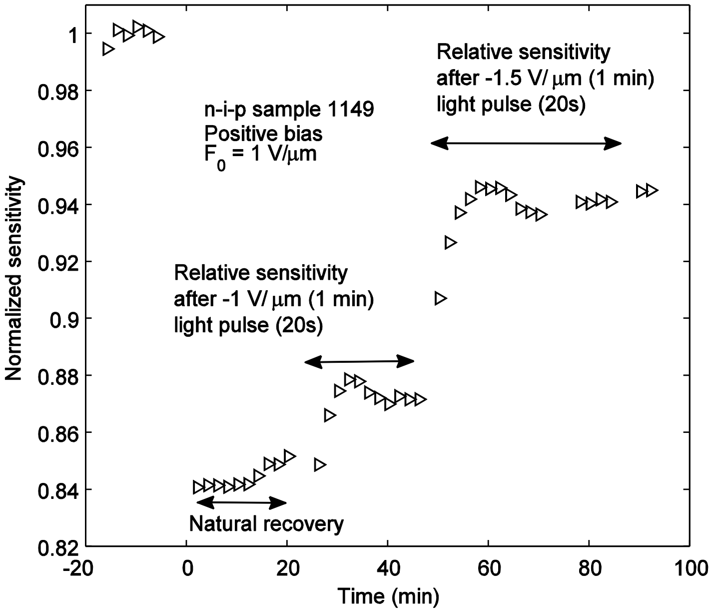

Figure 5.18 Relative X-ray sensitivity as a function of exposure and time for the sample 1149 at ~1 V/µm applied electric field.

Another experiment has been carried out using light pulse and reverse bias during natural recovery. Figure 5.19 shows the relative sensitivity as a function of accumulated X-ray exposures and time for the sample 1149. After obtaining the change in sensitivity for 6 probe pulses within the first 12 minutes, the ghost pulse is applied. The exposure for each test pulse is 15.5 mR and the exposure for the ghost pulse is 69 R. After 22 minutes of natural recovery, the field is reversed to ~0.5 V/μm and held for 1 minute. During this time, the sample is shined by the blue light from the back (charge collection electrode) for 20 s. Then the field is restored to the initial positive polarity and the probe pulses are applied to measure the sensitivity. After 32 minutes, the field is reversed to ~1 V/μm and held for 1 minute. During this time, the sample is shined by the blue light from the back (charge collection electrode) for 20 s. Then the field is restored to the initial positive polarity, and the sensitivity is measured. After 40 minutes the field is reversed to ~2.5 V/μm and held for 1 minute. During this time, no light pulse is applied. Then the field is restored to the initial positive polarity and the sensitivity is measured.

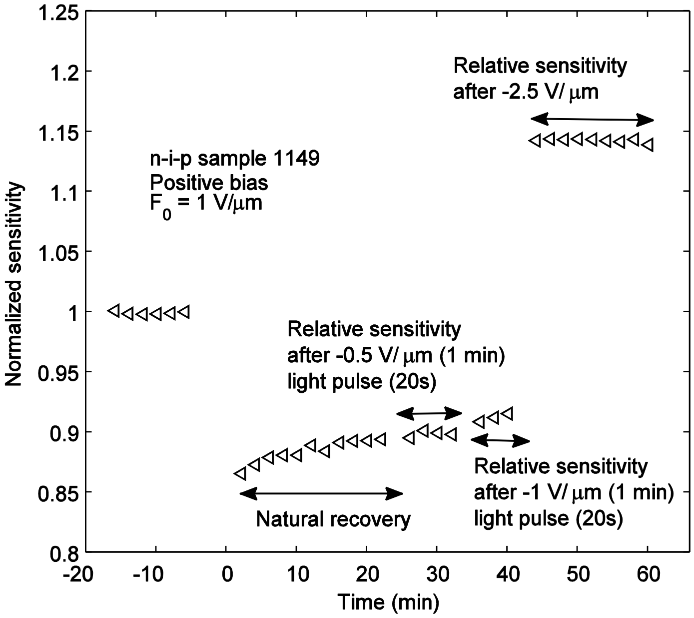

Figure 5.19 Relative X-ray sensitivity as a function of exposure and time for the sample 1149 at ~1 V/μm applied electric field.

It is evident from Figs. 5.18 and 5.19 that, the shining light from the back reduces rate of recovery due to reverse bias. It is explained before that, the faster recovery after the reverse bias is due to trap filling effect. Light generation can create more trap centers in the p-layer and thus, hole trapping reduces the interface electric field in the p-layer. Therefore, the hole injection due to reverse bias is minimized, which eventually reduce the trap filling effect. After the field is restored to initial positive polarity, the trapped holes in the p-layer enhance the electron injection form the bottom electrode and the trap filling effect increases gradually.

5.5 Conclusions

In this chapter, the ghosting recovery mechanisms in multilayer a-Se structures for mammography under low bias are examined. A ghost removal technique is investigated by reversing the bias polarity during the natural recovery process. After ghosting, the sensitivity in a rested sample is recovered mainly by trap filling, relaxation of the deep trap centers, and recombination of the injected carriers with the existing trapped carriers. A faster sensitivity recovery is found by reversing the bias during the natural recovery process. During the reverse bias, a large number of carriers is injected from the metal contacts and recombines with the existing trapped charges, but mostly fills the trap centers. This results in an abrupt recovery of the relative sensitivity. The release of trapped electrons enhances the trapping rates in subsequent probe pulses and, therefore, the relative sensitivity decreases over time. An increased magnitude of the interim reverse bias results in faster sensitivity recovery.

CHAPTER 6

CONCLUSIONS, CONTRIBUTIONS, AND FUTURE WORKS

In this thesis, a set of theoretical and experimental works have been presented to investigate the physical mechanisms responsible for time and bias dependent dark current, and X-ray induced change in sensitivity (ghosting) in multilayer a-Se detectors. An analytical model has been developed to describe the transient and steady-state dark current in a-Se based X-ray image detectors. A theoretical model has also been developed to describe the transient and steady-state dark current in a-Si:H p-i-n photodiode. The developed dark current model has also been applied to poly-HgI_2 based detectors. The developed models have been validated with the measured and published experimental results. The models show a very good agreement with the experimental results. The comparison of the models with the experimental data estimates some important properties (e.g., trap center concentrations, barrier heights) of the detector material. The dark current has a significant effect on the variation in X-ray sensitivity when the amount of injected carriers is comparable to the amount of X-ray generated carriers.

We have suggested a ghost removal technique by reversing the bias polarity during the natural recovery process under no irradiation. We examine the relative sensitivity as a function of accumulated X-ray exposures and time in a-Se detectors for mammography by solving the carrier transport equations (e.g., continuity, trapping rate, and Poisson's equations) numerically. The theoretical model considers the carrier injection from the metal contacts during the reverse bias. The validation of the simulation results with the experimental data quantitatively explains the carrier dynamics and the sensitivity recovery mechanisms under reverse bias. The contributions of this research are summarized in the following sections.

6.1 Dark Current

A theoretical model for describing the transient and steady-state behavior of dark current in a-Se based X-ray image detectors has been developed. The analytical model considers carrier injections from the metal contacts and thermally generated carriers from the bulk. The main source of dark current is the injection of holes from the metal/n-layer interface, which is described by the diffusion theory. The hole injection from the metal depends on the blocking layer (n-layer) thickness, concentration of trap centers in the blocking layer, characteristics carrier release time, and the effective barrier height. The thermal generation current is much smaller compared to the injection current due to the large band-gap in a-Se. The validation of the first principle model with the experimental results estimates the concentration of deep hole trap center in the n-layer, trap depth from the valence band edge, and the effective barrier heights for the injecting carriers. The dark current in the p-i-n structure is higher than the n-i-p structure, since holes are injected from the bottom electrode (ITO) in p-i-n structures. The saturated values of trapped carriers in the blocking layers increase with increasing the applied electric field. Increasing trap centers in the blocking layers may apparently beneficial for lowering the dark current. However, we need to increase the doping for increasing trap centers, which may change the effective barrier height and the depth of the trap centers. Increasing the blocking layer (n-layer) thickness also reduces the dark current. However, the X-ray generated carrier in the thick blocking layer (n-layer) will move slowly under lower electric field, which will reduce the overall charge collection efficiency of the detector. Therefore, a tradeoff between the lower dark current (wider n-layer) and the higher sensitivity (thinner n-layer) is necessary to find an optimum n-layer thickness. The electron injection from the negative electrode increases due to the reduced effective barrier height resulting from the smaller metal work function.

A theoretical model for describing the bias-dependent transient and steady-state behavior of dark current in hydrogenated amorphous silicon (*a*-Si:H) p-i-n photodiode has been developed. The dark current in a-Si:H photodiode has two components, thermal generation in the i-layer and the electron injection through the p-i interface. The validation of the physics-based model with the experimental results estimates the active dopant in the p-layer in the range of $\sim 10^{18}$ /cm^3 and the mid-gap defect density changes from $\sim 10^{16}$ /cm^3/eV to $\sim 2 \times 10^{16}$ /cm^3/eV due to X-ray radiation. Photodiodes that have very good junction properties, the high initial dark current decreases with time monotonously and reaches a plateau and, in case of poor junctions, the dark current decays initially and then rises to a steady-state value.

The developed dark current model has been applied to describe the steady-state behavior of dark current in poly-HgI_2 detectors. The dark current in poly-HgI_2 detectors is mainly controlled by the electron injection from the metal electrode. The bulk thermal generation current is considerably low compared to the electron injection current due to large energy band-gap of poly-HgI_2. The validation of the physics-based model with the experimental results estimates the effective barrier height for electron injection, which varies from ~1 eV to ~1.1 eV.

6.2 Ghosting and its Recovery

The ghosting and its recovery mechanisms in multilayer a-Se structures for mammography under low bias are examined. A ghost removal technique is investigated by reversing the bias polarity during the natural recovery process. The theoretical model considers the accumulated trapped charges in both charged and neutral defect states and their effects (trap filling, recombination, electric field profile, and electric field dependent electron-hole pair creation), the carrier transport in the blocking layers, and the effects of charge injection from the metal contacts. The X-ray induced deep trap centers are considered as charged defects. The continuity equations, the trapping rate equations, and the Poisson's equation in all three a-Se layers for a step X-ray exposure are simultaneously solved. There are two distinct regions of natural recovery; (i) an initial faster recovery and (ii) a subsequent slow recovery. The faster recovery is due to the release of trapped holes, which are added to the collected charge. The slow recovery is due to the relaxation of the X-ray induced trap centers and the trap filling by the generated electrons owing to probe pulses. It has been found that, the relatively faster electron release rate as compared to the relaxation rate of the X-ray induced trap centers results empty trap center available for further trapping of electrons, which eventually slows down the rate of recovery. The sensitivity is expected to reach the initial sensitivity level, naturally, by resting the sample longer than the recovery time constant of the meta-stable trap centers. A faster sensitivity recovery is found by reversing the bias during the natural recovery process. During reverse bias, a large number of carriers is injected from the metal contacts and recombines with the existing trapped charges, but mostly fills the trap centers. This results in an abrupt recovery of the relative sensitivity. It has been found that, the faster electron release rate as compared to the relaxation rate of the X-ray induced trap centers results in empty trap centers available for further trapping of electrons. Therefore, the slow decrease in sensitivity after the interim reverse bias is due to the lower characteristic release time of the trapped electrons as compared to the higher characteristic recovery time of the X-ray induced meta-stable trap centers. It has been found by simulation that, a higher electron release time and (or) a lower induced trap center recovery time ceases the decrease in relative sensitivity after the interim reverse bias, and the relative sensitivity eventually reaches the initial sensitivity. Due to the reverse bias, the dark current increases to almost three orders of the initial value. An increased magnitude of the interim reverse bias results in faster sensitivity recovery.

The sensitivity recovery by shining blue light from the back (charge collection electrode) has been investigated, but this method is not very successful in n-i-p detector structures. The sensitivity recovery by shining light and reverse bias has also been investigated. It has been found that, shining light with reverse bias slightly improves the rate of recovery. However, the recovery rate is not as fast as compared to reverse bias technique.

6.3 Suggestions for Future Works

The developed dark current model shows a very good agreement with the experimental results under normal operating field in a-Se layer. However, the model can be verified with dark current behavior in avalanche selenium detectors (if data is available) to test its robustness. The appropriateness of the developed dark current model can be examined under different electric field applications. The developed dark current model considers uniform trapping in the blocking layers. Considering non uniform trapping in the blocking layers, the dark current model can be modified.

The transient behavior of dark current during ghosting and recovery can be characterized. The ghosting and recovery can be investigated in a-Se based n-i detectors. The effect of reverse bias on the resolution of the detector can be examined. The ghosting and recovery model described in this thesis can be applied to other photoconductive detectors (e.g., HgI_2, PbI_2, CdZnTe). The ghost removal technique by reverse bias can also be examined in these detectors. Charge collection (sensitivity) and ghosting models can be extended to study indirect conversion detectors and solar cells. The ghosting model can be modified to describe the image lag in both the direct and indirect conversion detectors.

Appendix A

If the injected hole concentration decays exponentially due to trapping, the carrier concentration can be written as

$$c(x) = B\exp(-x / \mu F_0 \tau), \tag{A.1}$$

where τ is the carrier lifetime, μ is the carrier mobility, F_0 is the electric field, and B is the carrier concentration at $x = 0$. The drift and diffusion current components are,

$$J_{drift} = e\mu F_0 c, \tag{A.2}$$

and $J_{diff} = -eD\dfrac{dc}{dx}$. (A.3)

Taking, $F_0 \approx V/L$ and using Einstein relation, the ratio of the diffusion current to the drift current is,

$$J_{diff} / J_{drift} = (L / \mu F_0 \tau)(V_t / V) \tag{A.4}$$

where V is the bias voltage, L is the total photoconductor thickness and $V_t = kT/e$ is the thermal voltage. The ratio $L/\mu F_0 \tau$ is the inverse of normalized schubweg, which has to be smaller (preferably smaller than one) for detector applications. The applied voltage is in the range of few hundreds to few thousands volts. At extreme case, taking $L/\mu F_0 \tau = 100$ in the *i*-layer, and $V = 200$ V, the ratio of diffusion current to the drift current at room temperature is ~ 0.01. Therefore, the diffusion current component is negligible compared to its drift component in detector applications.

References

[1] J. M. Boone, “X-ray production, interaction, and detection in diagnostic imaging” in *Handbook of Medical Imaging* vol. 1, J. Beutel, H. L. Kundel, and R. L. Van Metter, Ed. Washington: SPIE, 2000, ch. 1.

[2] H. E. Johns and J. R. Cunningham, *The physics of radiology*. 4th ed. Springfield, IL: Charges C Thomas, 1983, chs. 5 and 7.

[3] http://www.radiologyinfo.org (May 24, 2011)

[4] S. O. Kasap and J. A. Rowlands, “Direct-conversion flat-panel X-ray image detectors,” *IEE Proceedings*: *Circuits, Devices, and Systems*, vol. 149, no. 2, pp. 85−96, Apr. 2002.

[5] J. A. Rowlands and J. Yorkston, “Flat panel detectors for digital radiography” in *Handbook of Medical Imaging*, vol. 1, J. Beutel, H. L. Kundel, and R. L. Van Metter, Ed. Washington: SPIE, 2000, ch. 4.

[6] K. Kotter and M. Langer, “Digital radiography with large-area flat-panel detectors,” *European Radiology*, vol. 12, no. 10, pp. 2562−2570, Oct. 2002.

[7] M. Spahn, “Flat detectors and their clinical applications,” *European Radiology*, vol. 15, no. 9, pp. 1934−1947, Sep. 2005.

[8] L. E. Antonuk, Y. El-Mohri, W. Huang, K. -W. Jee, J. H. Siewerdsen, M. Maolinbay, V. E. Scarpine, H. Sandler, and J. Yorkston, “Initial performance evaluation of an indirect-detection, active matrix flat-panel imager (AMFPI) prototype for megavoltage imaging,” *International Journal of Radiation Oncology Biology Physics*, vol. 42, no. 2, pp 437−54, Sep. 1998.

[9] M. Hoheisel, M. Arques, J. Chabbal, C. Chaussat, T. Ducourant, G. Hahm, H. Horbaschek, R. Schulz, and M. Spahn, “Amorphous silicon X-ray detectors,” *Journal of Non-Crystalline Solids*, vol. 227–230, part 2, pp. 1300–1305, May 1998.

[10] T. Jing, C. A. Goodman, J. Drewery, G. Cho, W. S. Hong, H. Lee, S. N. Kaplan, V. Perez-Mendez, and D. Wildermuth, “Detection of charged particles and X-rays by scintillator layers coupled to amorphous silicon photodiode arrays,” *Nuclear Instruments*

and Methods in Physics Research A: *Accelerators, Spectrometers, Detectors and Associated Equipment*, vol. 368, no. 3, pp. 757−764, Jan. 1996.

[11] S. Kasap, J. B. Frey, G. Belev, O. Tousignant, H. Mani, L. Laperriere, A. Reznik, and J. A. Rowlands, "Amorphous selenium and its alloys from early xeroradiography to high resolution X-ray image detectors and ultrasensitive imaging tubes," *Physica Status Solidi B*, vol. 246, no. 8, pp. 1794−1805, Aug. 2009.

[12] G. Zentai, L. Partain, R. Pavlyuchkova, C. Proano, M. Schieber, K. Shah, P. Bennett, L. Melekhov, and H. Gilboa, "Comparison of mercuric iodide and lead iodide X-ray detectors for X-ray imaging applications," *IEEE Transactions on Nuclear Science*, vol. 53, no. 5, pp. 2506−2512, Oct. 2006.

[13] S. O. Kasap and G. Belev, "Progress in the science and technology of direct conversion x-ray image detectors: The development of a double layer a-Se based detector," *Journal of Optoelectronics and advanced materials*, vol. 9, no. 1, pp. 1−10, Jan. 2007.

[14] H. Du, L. E Antonuk, Y. El-Mohri, Q. Zhao, Z. Su, J. Yamamoto, and Y. Wang, "Investigation of the signal behavior at diagnostic energies of prototype, direct detection, active matrix, flat-panel imagers incorporating polycrystalline HgI_2," *Physics in Medicine and Biology*, vol. 53, no. 5, pp 1325−1351, Mar. 2008.

[15] I. Khodami, M. M. Adachi, M. Malhotra, F. Taghibakhsh, J. A. Rowlands, K. S. Karim, K. L. Kavanagh, "Light induced degradation in amorphous silicon photodiodes and implication for diagnostic medical imaging application," *Proceedings of the SPIE - The International Society for Optical Engineering*, *Medical Imaging*, vol. 6142, pp. 61422U−1−9, 2006.

[16] S. O. Kasap, and J. A. Rowlands, "Direct-conversion flat-panel X-ray image sensors for digital radiography," *Proceedings of the IEEE*, vol. 90, no. 4, pp 591−604, Apr. 2002.

[17] S. O. Kasap, "Photoreceptors: the chalcogenides," in *Handbook of Imaging Materials*, 2nd ed. A. S. Diamond and D. S. Weiss, Ed. New York: Marcel Dekker, 2002, pp. 329−368.

[18] S. O. Kasap and J. A. Rowlands, "X-ray photoconductors and stabilized a-Se for direct conversion digital flat panel X-ray image detectors," *Journal of Materials Science*: *Materials in Electronics,* vol. 11, no. 3, pp. 179−198, Apr. 2000.

[19] G. Belev, S. Kasap, J. A. Rowlands, D. Hunter, and M. Yaffe, “Dependence of the electrical properties of stabilized a-Se on the preparation conditions and the development of a double layer X-ray detector structure,” *Current Applied Physics*, vol. 8, no. 3−8, pp. 383−387, May 2008.

[20] **S. A. Mahmood**, M. Z. kabir, O. Tousignant, H. Mani, J. Greenspan, and P. Botka, “Dark current in multilayer amorphous selenium X-ray imaging detectors,” *Applied Physics Letters*, vol. 92, no. 22, pp. 223506−1−3, Jun. 2008.

[21] J. B. Frey, G. Belev, O. Tousignant, H. Mani, and S. O. Kasap, “Dark current in multilayer stabilized amorphous selenium X-ray photoconductors,” *Physica Status Solidi C*, vol. 6, no. S1, pp. S251− S254, May 2009.

[22] D. C. Hunt, O. Tousignant, and J. A. Rowlands, “Evaluation of the imaging properties of an amorphous selenium-based flat panel detector for digital fluoroscopy,” *Medical Physics*, vol. 31, no. 5, pp. 1166−1175, May 2004.

[23] M. F. Stone, W. Zhao, B. V. Jack, P. O’Connor, B. Yu and P. Rehak, “The X-ray sensitivity of amorphous selenium for mammography,” *Medical Physics*, vol. 29, no. 3, pp. 319−324, Mar. 2002.

[24] R. E. Johanson, S. O. Kasap, J. Rowlands and B. Polischuk, “Metallic electrical contacts to stabilized amorphous selenium for use in X-ray image detectors,” *Journal of Non-Crystalline Solid*, vol. 227−230, pt. 2, pp. 1359−1362, May 1998.

[25] G. Belev and S. O. Kasap, ”Reduction of dark current in stabilized a-Se based X-ray detectors,” *Journal of Non-Crystalline Solid*, vol. 352, no. 9−20, pp. 1616−1620, Jun. 2006.

[26] M. Z. Kabir, M. Yunus, S. O. Kasap, O. Tousignant, H. Mani, and P. Gauthier, “Sensitivity of stabilized a-Se based X-ray photoconductors,” *Current Applied Physics*, vol. 6, no. 3, pp. 393−398, Jun. 2006.

[27] L. Bakueva, A. W. Rau, J. A. Rowlands, and A. Shik, “X-ray induced ghosting in amorphous selenium,” *Journal of Physics D*: *Applied Physics*, vol. 39, no. 3, pp. 441−448, Feb. 2006.

[28] F. Manouchehri, M. Z. Kabir, O. Tousignant, H. Mani, and V. K. Devabhaktuni, “Time and exposure dependent x-ray sensitivity in multilayer amorphous selenium

detectors," *Journal of Physics D*: *Applied Physics*, vol. 41, no. 23, pp. 235106−1−10, Dec. 2008.

[29] C. A. Klein, "Bandgap dependence and related features of radiation ionization energies in semiconductors," *Journal of Applied Physics*, vol. 39, no. 4, pp. 2029−2038, Mar. 1968.

[30] W. Que and J. A. Rowlands, "X-ray photogeneration in amorphous selenium: geminate versus columnar recombination," *Physical Review B*, vol. 51, no. 16, pp. 10500−10507, Apr. 1995.

[31] I. M. Blevis, D. C. Hunt, and J. A. Rowlands, "Measurement of x-ray photogeneration in amorphous selenium," *Journal of Applied Physics*, vol. 85, no. 11, pp. 7958−7962, Jun. 1999.

[32] G. Belev and S. O. Kasap, "Amorphous selenium as an X-ray photoconductor," *Journal of Non-crystalline Solids*, vol. 345−346, pp. 484−488, Oct. 2004.

[33] W. Shockley, "Currents to conductors induced by a moving point charge," *Journal of Applied Physics*, vol. 9, no. 10, pp. 635−636, Oct. 1938.

[34] S. Ramo, "Current induced by electron motion," *Proceedings of the IRE*, vol. 27, no. 9, pp. 584−585, Sep. 1939.

[35] Z. He, "Review of the Shockley-Ramo theorem and its application in semiconductor gamma-ray detectors," *Nuclear Instruments and Methods in Physics Research A*: *Accelerators, Spectrometers, Detectors and Associated Equipment*, vol. 463, no. 1−2, pp. 250−267, May 2001.

[36] S. O. Kasap, *Optoelectronics and photonics*: *Principles and practices*. Upper Saddle River, NJ: Prentice-Hall, 2001, ch. 5.

[37] R. A. Street, "Recombination in amorphous semiconductors," *Physical Review B*, vol.17, no. 10, pp. 3984−3995, May 1978.

[38] S. O. Kasap, *Principles of electronic materials and devices*. 3rd ed. New York: McGraw-Hill, 2006, ch. 1.

[39] S. O. Kasap, C. Haugen, M. Nesdoly, J. A. Rowlands, “Properties of a-Se for use in flat panel X-ray image detectors,” *Journal of Non-crystalline Solids*, vol. 266−269, pp. 1163−1167, May 2000.

[40] D. Adler and E. J. Yoffa, “Localized electronic states in amorphous semiconductors,” *Canadian journal of Chemistry*, vol. 55, no. 11, pp. 1920−1929, 1977.

[41] M. Z. Kabir, “Modeling of X-ray photoconductors for X-ray image detectors,” Doctoral Thesis, Electrical Engineering, University of Saskatchewan, Saskatoon, Canada, 2005.

[42] M. Kastner, D. Adler, and H. Fritzsche “Valence-alternation model for localized gap states in lone-pair semiconductors,” *Physical Review Letters*, vol. 37, no. 22, pp. 1504−1507, Nov. 1976.

[43] M. Abkowitz and R. C. Enck, “Photoenhanced metastable deep trapping in amorphous chalcogenides near room temperature,” *Physical Review B*: *Condensed Matter*, vol. 27, no. 12, pp. 7402−7411, Jun. 1983.

[44] A. V. Kolobov, H. Oyanagi, A. Roy, and K. Tanaka, “A nanometer scale mechanism for the reversible photostructural change in amorphous chalcogenides,” *Journal of Non-crystalline Solids*, vol. 232−234, pp. 80−85, Jul. 1998.

[45] K. Morigaki, *Physics of amorphous semicondcutors*. World Scientific Pub Co Inc, 1999, ch. 5.

[46] M. Abkowitz, “Density of states in a-Se from combined analysis of xerographic potentials and transient transport data,” *Philosophical Magazine Letters,* vol. 58, no. 1, pp. 53−57, Jul. 1988.

[47] S. O. Kasap and C. Juhasz, “Modelling of photoinduced discharge of double-layer photoreceptors: general formulation and small signal xerographic time-of-flight analysis,” *Journal of Physics D*: *Applied Physics*, vol. 27, no. 3, pp. 574−581, Mar. 1994.

[48] S. O. Kasap and C. Juhasz, “Time-of-flight drift mobility measurements on chlorine doped amorphous selenium films,” *Journal of Physics D*: *Applied Physics*, vol. 18, no. 4, pp. 703−720, Apr. 1985.

[49] H. -Z. Song, G. J. Adriaenssens, E. V. Emelianova, and V. I. Arkhipov, “Distribution of gap states in amorphous selenium thin films,” *Physical Review B*: *Condensed Matter*, vol. 59, no. 16, pp. 10607−10613, Apr. 1999.

[50] S. O. Kasap, K. V. Koughia, B. Fogal, G. Belev, R. E. Johanson, “The influence of deposition conditions and alloying on the electronic properties of amorphous selenium,” *Semiconductors*, vol. 37, no. 7, pp. 789−794, Jul. 2003.

[51] K. Koughia, Z. Shakoor, S. O. Kasap, and J. M. Marshall, “Density of localized electronic states in a-Se from electron time-of-flight photocurrent measurements,” *Journal of Applied Physics*, vol. 97, no. 3, pp. 033706−1−11, Feb. 2005.

[52] S. Kasap, J. B. Frey, G. Belev, O. Tousignant, H. Mani, J. Greenspan, L. Laperriere, O. Bubon, A. Reznik, G. DeCrescenzo, K. S. Karim and J. A. Rowlands, “Amorphous and polycrystalline photoconductors for direct conversion flat panel X-ray image sensors,” Sensors, vol. 11, no. 5, pp. 5112−5157, May 2011.

[53] S. O. Kasap, M. Z. Kabir, and J. A. Rowlands, “Recent advances in X-ray photoconductors for direct conversion X-ray image sensors,” *Current Applied Physics*, vol. 6, no. 3, pp. 288−292, Jun. 2006.

[54] C. Haugen, S. O. Kasap, and J. A. Rowlands, “Charge transport and electron-hole pair creation energy in stabilized a-Se x-ray photoconductors,” *Journal of Physics D*: *Applied Physics*, vol. 32, no. 3, pp. 200−207, Feb. 1999.

[55] E. Fourkal, M. Lachaine, and B. G. Fallone, “Signal formation in amorphous-Se-based X-ray detectors,” *Physical Review B*: *Condensed Matter and Materials Physics*, vol. 63, no. 19, pp. 195204−1−8, May 2001.

[56] R. A. Street, “Introduction,” in *Technology and applications of Amorphous Silicon*, R. A. Street, Ed. New York: Springer-Verlag, 2000, ch. 1.

[57] K. Tanaka, E. Maruyama, T. Shimada, and H. Okamoto, *Amorphous Silicon*. New York: John Wiley & Sons, 1998, ch. 3.

[58] R. A. Street, *Hydrogenated Amorphous Silicon*. New York: Cambridge University Press, 1991, ch. 7.

[59] H. Wieczorek, “Effects of trapping in a-Si:H diodes,” *Diffusion and Defect Data Part B* (*Solid State Phenomena*), vol. 44−46, pt. 1, pp. 957−972, 1995.

[60] R. A. Street, “Thermal generation currents in hydrogenated amorphous silicon p-i-n structures,” *Applied Physics Letters*, vol. 57, no. 13, pp. 1334−1336, Sep. 1990.

[61] R. A. Street, *Hydrogenated Amorphous Silicon*. New York: Cambridge University Press, 1991, ch. 10.

[62] Z. Su, L. E Antonuk, Y. El-Mohri, L. Hu, H. Du, A. Sawant, Y. Li, Y. Wang, J. Yamamoto, and Q. Zhao, “Systematic investigation of the signal properties of polycrystalline HgI_2 detectors under mammographic, radiographic, fluoroscopic and radiotherapy irradiation conditions,” *Physics in Medicine and Biology*, vol. 50, no. 12, pp. 2907−2928, Jun. 2005.

[63] P. J. Sellin, “Thick film compound semiconductors for X-ray imaging applications,” *Nuclear Instruments and Methods in Physics Research A*: *Accelerators, Spectrometers, Detectors and Associated Equipment*, vol. 563, no. 1, pp. 1−8, Jul. 2006.

[64] G. Zentai, L. Partain, R. Pavlyuchkova, C. Proano, G. Virshup, L. Melekhov, A. Zuck, B. N. Breen, O. Dagan, A. Vilensky, M. Schieber, H. Gilboa, P. Bennet, K. Shah, Y. Dmitriev, J. Thomas, M. Yaffe, and D. Hunter “Mercuric iodide and lead iodide X-ray detectors for radiographic and fluoroscopic medical imaging,” *Proceedings of the SPIE - The International Society for Optical Engineering*, *Medical Imaging*, vol. 5030, pp. 77−91, 2003.

[65] G. Zentai, L. Partain, R. Pavlyuchkova, C. Proano, B. N. Breen, A. Taieb, O. Dagan, M. Schieber, H. Gilboa, and J. Thomas, “Mercuric iodide medical imagers for low exposure radiography and fluoroscopy,” *Proceedings of the SPIE - The International Society for Optical Engineering*, *Medical Imaging*, vol. 5368, pp. 200−210, 2004.

[66] A. Zuck, M. Schieber, O. Khakhan, and Z. Burshtein, “Near single-crystal electrical properties of polycrystalline HgI_2 produced by physical vapor deposition,” *IEEE Transaction on Nuclear Science*, vol. 50, no. 4, pp. 991−997, Aug. 2003.

[67] S. Chen-Tsung, H. Tang-Jung, L. Ying-Zi, L. San-Min, C. Kuan-Cheng, “Oriented polycrystalline α-HgI_2 thick films grown by physical vapor deposition,” *Journal Crystal Growth*, vol. 280, no. 3−4, pp. 442−447, Jul. 2005.

[68] R. A. Street, S. E. Ready, K. Van Schuylenbergh, J. Ho, J. B. Boyce, P. Nylen, K. Shah, L. Melekhov, and H. Hermon, “Comparison of PbI_2 and HgI_2 for direct detection active matrix X-ray image sensors,” *Journal of Applied Physics*, vol. 91, no. 5, pp. 3345−3355, Mar. 2002.

[69] S. M. Sze and K. K. Ng, *Physics of Semiconductor Devices*. 3rd ed. New Jersey: John Wiley & Sons, 2007, ch. 3.

[70] R. A. Street, “Long-time transient conduction in a-Si:H p-i-n devices,” *Philosophical Magazine B*, vol. 63, no. 6, pp. 1343−1363, Jun. 1991.

[71] M. Mulato, C. M. Hong, and S. Wagner, “Size and etching effects on the reverse current of a-Si:H p-i-n diodes”, *Journal of the Electrochemical Society*, vol. 150, no. 12, pp. G735−G738, Dec. 2003.

[72] H. P. D. Lanyon, “Electrical and optical properties of vitreous selenium”, *Physical Review*, vol. 130, no. 1, pp. 134−143, Apr. 1963.

[73] J. L. Hartke, “Drift mobilities of electrons and holes and space-charge-limited currents in amorphous selenium films”, *Physical Review*, vol. 125, no. 4, pp. 1177−1192, Feb. 1962.

[74] G. Pfister and A. Lakatos, “One-carrier and two-carrier steady state space-charge-limited currents in amorphous selenium”, *Physical Review B*: *Solid State*, vol. 6, no. 8, pp. 3012−3018, Oct. 1972.

[75] L. Müller and M. Müller, “Current-voltage characteristics at high fields in amorphous selenium thin layers,” *Journal of Non-Crystalline Solids*, vol. 4, pp. 504−509, Apr. 1970.

[76] G. S. Belev, “Electrical properties of amorphous selenium based photoconductive devices for application in X-ray image detectors,” Doctoral Thesis, University of Saskatchewan, Saskatoon, Canada, 2007.

[77] S. O. Kasap, and C. Juhasz, “Charge transport in selenium based amorphous xerographic photoreceptors,” *Photographic Science and Engineering*, vol. 26, no. 5, pp. 239−244. Sep.−Oct. 1982.

[78] S. O. Kasap, “X-ray sensitivity of photoconductors: application to stabilized a-Se,” *Journal of Physics D*: *Applied Physics*, vol. 33, no. 12, pp. 2853–2865, Dec. 2000.

[79] S. M. Vaezi-Nejad and C. Juhasz, “Electrical properties of amorphous semiconductor selenium and its alloys: I. Monolayers,” *Semiconductor Science and Technology,* vol. 2, no. 12, pp. 809−821, Dec. 1987.

[80] S. O. Kasap, V. Aiyah, B. Polischuk, A. Bhattacharyya, and Z. Liang, "Deep-trapping kinematics of charge carriers in amorphous semiconductors: A theoretical and experimental study," *Physical Review B*: *Condensed Matter*, vol. 43, no. 8, pp. 6691−6705, Mar. 1991.

[81] G. J. Rees, H. G. Grimmeiss, E. Janzen, and B. Skarstam, "Capture, emission and recombination at a deep level via an excited state," *Journal of Physics C*: *Solid State Physics*, vol. 13, no. 33, pp. 6157−6165, Nov. 1980.

[82] G. Micocci, P. Siciliano, and A. Tepore, "Photoinduced current transient spectroscopy in InSe single crystals," *Solar Energy Materials*, vol. 20, no. 3, pp. 181−187, Mar. 1990.

[83] **S. A. Mahmood** and M. Z. Kabir, "Dark current mechanisms in stabilized amorphous selenium based n-i detectors for x-ray imaging applications," *Journal of Vacuum Science and Technology A*: *Vacuum, Surfaces and Films,* vol. 29, no. 3, pp. 031603–1–6, May 2011.

[84] S. O. Kasap, B. Polischuk, and D. Dodds, "An interrupted field time-of-flight (IFTOF) technique in transient photoconductivity measurements," *Review of Scientific Instruments*, vol. 61, no. 8, pp. 2080−2087, Aug. 1990.

[85] **S. A. Mahmood** and M. Z. Kabir, "Modeling of transient and steady-state dark current in amorphous silicon p-i-n photodiodes," *Current Applied Physics,* vol. 9, no. 6, pp. 1393−1396, Nov. 2009.

[86] M. Z. Kabir, S. O. Kasap, and J. A. Rowlands, in *Springer Handbook of Electronic and photonic Materials*, Ed. S.O. Kasap and Peter Capper (Springer, Heidelberg, 2006), ch 48.

[87] G. E. Frank-Kamennetskaya, M. D. Vorontsov, and I. P. Kalinkin, "Electrical properties of film heterojunctions of cadmium selenide and amorphous selenium," *Soviet Physics Journal*, vol. 33, no. 11, pp. 952−957, Nov. 1990.

[88] S. Touihri, G. Safoula, and J. C. Bernéde, "Diode devices based on amorphous selenium films," *Physica Status Solidi A*, vol. 159, no. 2, pp. 569−578, Feb. 1997.

[89] J. C. Bernéde, S. Touihri, and G. Safoula, "Electrical characteristics of an aluminum/amorphous selenium rectifying contact," *Solid-State Electronics*, vol. 42, no. 10, pp. 1775−1778, Oct. 1998.

[90] J. K. Wu, S. A. Lyon, and W. C. Johnson, "Temperature and field dependence of the generation of interface states in the si-SiO2 system after high-field stress," *Applied Physics Letters*, vol. 42, no. 7, pp. 585−587, Apr. 1983.

[91] M. Z. Kabir, F. Manouchehri, **S. A. Mahmood**, V. K. Devabhaktuni, O. Tousignant, H. Mani, J. Greenspan, and P. Botka, "Modeling of dark current and ghosting in multilayer amorphous selenium X-ray detectors," in *Proceedings of the SPIE - The International Society for Optical Engineering*, *Medical Imaging*, vol. 6913, pp. 69133U–1–12, 2008.

[92] H. Kim, A. Pique, J. S. Horwitz, H. Mattoussi, H. Murata, Z. H. Kafafi and D. B. Chrisey, "Indium tin oxide thin films for organic light-emitting devices," *Applied Physics Letters,* vol. 74, no. 23, pp. 3444−3446, Jun. 1999.

[93] M. Hoheisel, N. Brutscher and H. Wieczorek, "Relaxation phenomena of image sensors made from a-Si:H," *Journal of Applied Physics*, vol. 66, no. 9, pp. 4466−4473, Nov. 1989.

[94] S. Kar and W. E. Dahlke, "Interface states in MOS structures with 20−40 Å thick SiO_2 films on nondegenerate Si," *Solid-State Electronics*, vol. 15, no. 2, pp. 221−237, Feb. 1972.

[95] J. Liang, E. A. Schiff, S. Guha, B. Yan and J. Yang, "Hole-mobility limit of amorphous silicon solar cells," *Applied Physics Letters*, vol. 88, no. 6, pp. 063512–1–3, Feb. 2006.

[96] H. J. Kim, G. Cho, T. H. Lee, and Y. S. Kim, "Comparative study on the radiation damage of a-Si:H p-i-n diodes made by PECVD and ion shower doping," *IEEE Transaction on Nuclear Science*, vol. 49, no. 5, pp. 2244–2249, Oct. 2002.

[97] M. Mulato, C. M. Hong, and S. Wagner, "Size and etching effects on the reverse current of a-Si:H p-i-n diodes," *Journal of the Electrochemical Society*, vol. 150, no. 12, pp. G735– G738, Dec. 2003.

[98] J. K. Arch and S. J. Fonash, “Origins of reverse bias leakage currents in hydrogenated amorphous silicon p-i-n detector structures,” *Applied Physics Letters*, vol. 60, no. 6, pp. 757–759, Feb. 1992.

[99] H. J. Kim and G. Cho, “Analysis of the transient leakage current of an a-Si:H p-i-n diode,” *Journal of the Korean Physical Society*, vol. 40, no. 5, pp. 908–912, May 2002.

[100] S. Tchakarov, P. Roca i Cabarrocas, U. Dutta, P. Chatterjee, and B. Equer, “Experimental study and modeling of reverse-bias dark currents in PIN structures using amorphous and polymorphous silicon,” *Journal of Applied Physics*, vol. 94, no. 11, pp. 7317–7327, Dec. 2003.

[101] J. B. Chévrier and B. Equer, “High electric-field amorphous silicon p-i-n diodes: effect of the p-layer thickness,” *Journal of Physics D*: *Applied Physics*, vol. 76, no. 11, pp. 7415−7422, Dec. 1994.

[102] Z. E. Smith, S. Aljishi, D. Slobodin, V. Chu, S. Wagner, P. M. Lenahan, R. R. Arya, and M. S. Bennett, “Thermal-equilibrium defect processes in hydrogenated amorphous silicon,” *Physical Review Letters*, vol. 57, no. 19, pp. 2450–2453, Nov. 1986.

[103] K. C. Kao and W. Hwang, “*Electrical transport in solids*,” New York: Pergamon Press, 1981, ch. 5.

[104] A. Cerdeira and M. Estrada, “Modeling of reverse current behavior in amorphous thin and thick p-i-n diodes,” *IEEE Transaction on Electron Devices*, vol. 47, no. 11, pp. 2238–2240, Nov. 2000.

[105] R. A. Street, *Hydrogenated Amorphous Silicon*. New York: Cambridge University Press, 1991, ch. 4.

[106] **S. A. Mahmood**, R. V. R. Murthy, M. Z. Kabir, and V. Dutta, “The role of bulk and interface states on performance of a-Si:H p-i-n solar cells using reverse current-voltage technique,” *Journal of Physics D*: *Applied Physics*, vol. 42, no. 14, pp. 145115−1−6, Jul. 2009.

[107] R. A. Street, “Large area image sensor arrays,” in *Technology and applications of Amorphous Silicon*, R. A. Street, Ed. New York: Springer-Verlag, 2000, ch. 4.

[108] W. B. Jackson, S. M. Kelso, C. C. Tsai, J. W. Allen, and S. -J. Oh, “Energy dependence of the optical matrix element in hydrogenated amorphous and crystalline

silicon," *Physical Review B*: *Condensed Matter*, vol. 31, no. 8, pp. 5187−5198, Apr. 1985.

[109] H. J. Kim, G. Cho, J. Choi, and K. Jung, "Leakage current of amorphous silicon p-i-n diodes made by ion shower doping," *Applied Physics Letters*, vol. 80, no. 25, pp. 4843−4845, Jun. 2002.

[110] A. Levi, M. M. Schieber, and Z Burshtein, "Dark current transients in HgI_2 single crystals used as γ- and x-ray spectrometers," *Journal of Applied Physics*, vol. 57, no. 6, pp. 1944−1950, Mar. 1985.

[111] Y. -C. Chang and R. B. James, "Theoretical studies of carrier transport in HgI_2," *Physical Review B*: *Condensed Matter*, vol. 53, no. 21), pp. 14200−14211. Jun. 1996.

[112] G. Xu, W. Jie, G. Li, and G. zha, "Study of trapping levels in α-HgI_2 crystals by UV and isothermal current measurements," *Nuclear Instruments and Methods in Physics Research A*: *Accelerators, Spectrometers, Detectors and Associated Equipment*, vol. 613, no. 2, pp. 277−279, Feb. 2010.

[113] **S. A. Mahmood** and M. Z. Kabir, "Dark current mechanisms in imaging detectors (review)," *Semiconductor Science and Technology*, to be submitted.

[114] B. Fogal, M. Z. Kabir, R. E. Johanson, S. K. O'Leary and S. O. Kasap, "X-ray induced recombination effects in a-Se based x-ray photoconductors used in direct conversion x-ray sensors," *Journal of Vacuum Science and Technology A*: *Vacuum, Surfaces and Films*, vol. 22, no. 3, pp. 1005−1009, May 2004.

[115] S. Steciw, T. Stanescu, S. Rathee, and B.G. Fallone, "Sensitivity reduction in biased amorphous selenium photoconductors," *Journal of Physics D*: *Applied Physics*, vol. 35, no. 21, pp. 2716−2722, Nov. 2002.

[116] W. Zhao, G. DeCrescenzo, and J. A. Rowlands, "Investigation of lag and ghosting in amorphous selenium flat-panel x-ray detectors," in *Proceedings of the SPIE - The International Society for Optical Engineering*, *Medical Imaging*, vol. 4682, pp. 9−20, 2002.

[117] J. Kalade, E. Montrimas and J. Rakauskas, "The mechanism of sensitivity reduction in selenium layers irradiated by X-rays," *Physica Status Solidi A*, vol. 25, no. 2, pp. 629–636, Oct. 1974

[118] S. O. Kasap and V. Aiyah, A. Baillie, A. G. Leiga, “X-ray induced hole trapping in electroradiographic plates,” *Journal of Applied Physics*, vol. 69, no. 10, pp. 7087–7096, May 1991

[119] U. Schiebel, T. Buckremer, G. Frings, and P. Quadfling, “Deep trapping and recombination in a-Se:As X-ray sensitive photoreceptors,” *Journal of Non-Crystalline Solids*, vol. 115, no. 1−3, pp. 216-218, Dec. 1989.

[120] A. W. Rau, L. Bakueva, and J. A. Rowlands, “The x-ray time of flight method for investigation of ghosting in amorphous selenium-based flat panel medical x-ray imagers,” *Medical Physics*, vol. 32, no. 10, pp. 3160−3177, Oct. 2005.

[121] M. Nesdoly, “X-ray sensitivity and x-ray induced charge transport changes in stabilized a-Se films,” Doctoral Thesis, Department of Electrical Engineering, University of Saskatchewan, Saskatoon, Canada, 2000.

[122] C. Allen, G. Belev, R. Johanson, and S. O. Kasap, “Relaxation of electrical properties of stabilized amorphous selenium based photoconductors,” *Journal of Non-Crystalline Solids*, vol. 354, no. 19–25, pp. 2711–2714, May 2008.

[123] D. K. Biegelsen and R. A. street, “Photoinduced Defects in Chalcogenide Glasses,” *Physical Review Letters*, vol. 44, no. 12, pp. 803−806, Mar. 1980 .

[124] C. Haugen and S. O. Kasap, “Langevin recombination of drifting electrons and holes in stabilized a-Se (Cl-doped a-Se:0.3% As),” *Philosophical Magazine B* (*Physics of Condensed Matter, Electronic, Optical and Magnetic Properties*), vol. 71, no. 1, pp. 91−96, Jan. 1995.

[125] S. O. Kasap, B. Fogal, M. Z. Kabir, R. E. Johanson, and S. K. O’Leary, “Recombination of drifting holes with trapped electrons in stabilized a-Se photoconductors: Langevin recombination,” *Applied Physics Letters*, vol. 84, no. 11, pp. 1991−1993, Mar. 2004.

[126] M. Yunus, M. Z. Kabir, and S. O. Kasap, “Sensitivity reduction mechanisms in amorphous selenium photoconductive x-ray image detectors,” *Applied Physics Letters*, vol. 85, no. 26, pp. 6430−6432, Dec. 2004.

[127] **S. A. Mahmood**, M. Z. Kabir, O. Tousignant, and H. Mani, “Ghosting and its recovery mechanisms in multilayer selenium detectors for mammography,” in

Proceedings of the SPIE - The International Society for Optical Engineering, *Medical Imaging*, vol. 7258, pp. 725860–1–11, 2009.

[128] **S. A. Mahmood**, M. Z. Kabir, O. Tousignant, and J. Greenspan "Investigation of ghosting recovery mechanisms in selenium X-ray detector structures for mammography," *IEEE Transaction on Nuclear Science*, accepted for June 2012 issue.

[129] M. Z. Kabir, M. Yunus, and S. O. Kasap, "Dependence of x-ray sensitivity of direct conversion x-ray detectors on x-ray exposure and exposure history," in *Proceedings of the SPIE - The International Society for Optical Engineering*, *Medical Imaging,* vol. 5368, pp. 170-176, 2004.

[130] M. Z. Kabir and S. O. Kasap, "Charge collection and absorption-limited sensitivity of X-ray photoconductors: Applications to a-Se and HgI_2," *Applied Physics Letters*, vol. 80, no. 9, pp. 1664–1666, Mar. 2002.

[131] **S. A. Mahmood**, M. Z. Kabir, O. Tousignant, J. Greenspan, and M. F. Mokam, "Investigation of ghosting recovery techniques and mechanisms in multilayer selenium X-ray detectors under low bias," in *Proceedings of the SPIE - The International Society for Optical Engineering*, *Medical Imaging*, vol. 7622, pp. 762216–1–8, 2010.